Politecnico di Milano
Department of Civil and Environmental Engineering
Doctoral School in structural, seismic and
geotechnical engineering

Three-dimensional numerical simulation of large scale landslides

Supervisors
Prof. Umberto Perego
Dr. Massimiliano Cremonesi

Tutor
Prof. Claudio di Prisco

The Chair of the Doctoral Program
Prof. Roberto Paolucci

Phd Candidate
Francesco Ferri

2016 – XXVIII cycle

Francesco Ferri
Three-dimensional numerical simulation of large scale landslides

e-mail:
francesco.ferri@polimi.it

Three-dimensional numerical simulation of large scale landslides

A Thesis
Presented to
The Academic Faculty

by

Francesco Ferri

In Partial Fulfillment
of the Requirements for the Degree

in
structural, seismic and geotechnical engineering

Milan, March 2016

Doctoral School in structural, seismic and geotechnical engineering
Department of Civil and Environmental Engineering
Politecnico di Milano

XXVIII cycle

Faculty Members

Prof. Roberto Paolucci (Chairman)
Prof. Raffaele Ardito
Prof. Fabio Biondini
Prof. Gabriella Bolzon
Prof. Claudia Comi
Prof. Alberto Corigliano
Prof. Dario Coronelli
Prof. Claudio Di Prisco
Prof. Mardo Di Prisco
Prof. Roberto Felicetti
Prof. Liberato Ferrara
Prof. Attilio Frangi
Prof. Elsa Garavaglia
Prof. Cristina Jommi
Prof. Pier Giorgio Malerba
Prof. Stefano Mariani
Prof. Umberto Perego
Prof. Federico Perotti
Prof. Lorenza Petrini
Prof. Luigi Zanzi

Abstract

The assessment of landslide hazard has become a topic of major interest not only for geoscientists and engineers but also for the community and the local administrations, in Italy and in many parts of the world. The reason for international interest in landslides is the increasing awareness of the socio-economic impact of landslides and the increased presence of development and urbanization on the environment, often in mountainous terrains. Flow-like landslides, for example debris flows or rock avalanches, due to high velocity and in some cases due to not preventable triggering mechanism (e.g. earthquake) are among the most dangerous events. Modelling such kind of landslides is important for the creation of accurate maps of hazardous areas, to estimate the entity of the hazard and finally to design appropriate protective measures. Starting from a two dimensional numerical tool for fluid-structure interaction problems, a three dimensional Lagrangian numerical approach, for the simulation of rapid landslides, has been developed. The simulation approach is based on the so called Particle Finite Element Method (PFEM), first proposed by Oñate, Idelsohn and coworkes at the International Center for Numerical Methods in Engineering (CIMNE).

The moving soil mass is assumed to obey a rigid-viscoplastic, non-dilatant Drucker-Prager constitutive law, which is cast in the form of a regularized, pressure sensitive Bingham model. Unlike in classical formulations of computational fluid mechanics, where no-slip boundary conditions are assumed, basal slip boundary conditions are introduced to account for the specific nature of the landslide-basal surface interface. The basal slip conditions are formulated in the

form of modified Navier boundary conditions, with a pressure sensitive threshold. A special mixed Eulerian-Lagrangian formulation is used for the elements on the basal interface to accommodate the new slip conditions into the PFEM framework. To avoid inconsistencies in the presence of complex shapes of the basal surface, the no-flux condition through the basal surface is relaxed using a penalty approach. The proposed model is validated by simulating both laboratory tests and real large scale problems. In particular, the well studied cases of the Frank avalanche and the Vajont slide are presented. In the latter, the mobilized material impinges into the water reservoir, generating a huge wave. In this case, both the terrain and the water have been modelled and simulated.

A related subject considered in this work is the implementation of a nodal integration instead of the standard elemental integration. An advantage of the Lagrangian approach for the fluid flow is that the convective terms in the momentum conservation disappear, and the difficulty is transmitted to the necessity to frequently retriangulate the mesh. When retriangulation is performed, data have to be transmitted from the old mesh to the new one. In this approach, to avoid interpolation from mesh to mesh, only degrees of freedom of particles located at the vertices of triangles, in 2D, and tetrahedra, in 3D, are used, so that only linear shape functions can be used for both velocity and pressure. Nevertheless some quantities like strains, stresses, density and apparent viscosity still have to be evaluated in the elements to perform the integration. This can lead to problems if more than one material is considered (e.g. terrain and water) or if nonlinear material behavior with internal variables is considered. A 2D approach based on nodal integration has been developed to avoid this obstacle.

Contents

List of Figures

List of Tables

1 Introduction

The term landslide denotes "the movement of a mass of rock, debris or earth down a slope" as described by Cruden, 1991. This is a complex process not merely related to the land or to sliding, the term has a much more extensive meaning which includes different movements (flows, slides, falls, etc.) and velocity ranges (from 1 mm a day to hundreds of meters per hour). Landslides can occur all over the Earth's surface, from the center of a city to desolate environments, in hillside or in steep mountain slopes but also in a sand dome or underwater (submarine landslides). Driven by the gravity force and therefore not limited to the Earth surface, more generally landslides can occur in every telluric planetary body. Movements on the surface of the Moon have been observed and reported in Xiao et al., 2013 and in Mars, (e.g. Brunetti et al. 2014), Venus (Malin, 1992), Mercury (Xiao and Komatsu, 2014), and in some icy satellites in the outer Solar System, (Schenk, 1998).

Among the various categories in which landslides can be divided, this work

deals exclusively with landslides for which the overall behavior is comparable to those of a fluid (flow-like landslides), where high speed and large runout normally take place. Furthermore landslides can be associated with other events. In particular, in the civil engineering field, the interaction with fluid reservoirs and with hydraulic structures like dams is of great interest.

The importance of landslides and their consequences have been often underestimated in the past, while in recent years the attention of the scientific community has grown. The development of a large number of models, very different one from the other, derives from the complexity of the phenomenon and from the physical different behaviors due to involved materials, topography, triggering mechanisms and many other important factors.

Procedures of intervention and mitigation, in situ analyses, laboratory experiments and numerical and physical models are all important tools in the assessment of landslides hazard and risk. In this work a numerical approach for the simulation of rapid landslides is presented and discussed.

Generally, in a landslide, three different phases are discernible: the initiation or triggering phase, the propagation phase and the deposition phase. Landslides are triggered by natural causes and/or human activities. Erosion at the base of a slope, saturation of soil due to prolonged or intense rainfall or snowmelt and earthquakes are some examples of natural causes. Excavation, construction or mining are human factors that can also trigger a landslide.

In the past, landslides were underestimated because their damages were considered simply as a result of the triggering phenomena. Conversely, they represent one of the most destructive hazards in nature, constituting a potentially high risk for human life and the built environment. During the last years, a huge number of landslides occurred in Italy due to the peculiarity of the geological configuration. The Veneto region is one of the most critical territory with about ten thousand active landslides (Tormen, 2015), which vary from slowly vast dimension landslides (Tessina landslide (van Westen and Lulie Getahun, 2003)) to rapid debris

flows.

The assessment of landslide hazard has become a topic of major interest not only for geoscientists and engineers but also for the community and the local administrations, in Italy and in many parts of the world. The reason for international interest in landslides is the increasing awareness of the socio-economic impact of landslides and the increased presence of development and urbanization on the environment, often in mountainous terrains. Aleotti and Chowdhury, 1999 suggest that, as urban development increases on sloping urban areas, a higher incidence of slope instability is to be expected.

Depending of the type of landslide, corrective measures can be achieved to stabilize slopes and prevent fatalities and damages, for example improving drainage and protecting the base of the slope from excavation or erosion, preventing constructions in valleys on volcanoes or steep mountain slopes or the installation of warning systems. When slope stabilization is almost impracticable the only manner to prevent fatalities and damage is the definition of areas that could be affected by the landslide. Flow-like landslides, for example debris flows or rock avalanches, due to high velocity and in some cases due to not preventable triggering mechanism (e.g. earthquake) are among the most dangerous events.

At the Department of Civil and Environmental Engineering (DICA) of Politecnico di Milano there is an active research program concerning the analysis of fluid-structure interaction problems. This dissertation is part of this research program. Starting from a numerical tool for fluid-structure problems (Cremonesi et al., 2010) a three dimensional lagrangian numerical approach for the simulation of rapid landslides has been developed. Modeling such kind of landslides is important for the creation of accurate maps of hazardous areas, to estimate the entity of the hazard and finally to design appropriate protective measures.

The simulation approach is based on the so called Particle Finite element Method (PFEM), a powerful method that has been applied in a wide range of problems (e.g. ship hydrodynamics, wave impact on breakwater harbours,

soil/rock excavation problems, melting and burning of objects in fire, mixing of substances, industrial forming processes, etc.) (Oñate et al., 2011).

Often, simple fluid dynamics problems can be studied in two dimensions. In other cases, the geometry of the problem does not allow the reduction to a two-dimensional approach and obliges a truly three-dimensional framework. An example is the simulation of landslides within a basin, with the identification of the propagating wave front and the effect of such a wave on a structure. The use of a three-dimensional approach, could in this case allow the study of a wave that propagates across the slope where the landslide took place, as happened for example, in the Mount Toc landslide that led to the tragedy of Vajont in 1963.

The outline of the thesis can be described as follows:

Chapter 2 constitute an introduction to granular matter and experimental tests of granular flows which have been used to validate the model. Subsequently a landslide classification, with a focus on flow-like landslides, is given and a briefly presentation of some historical cases is reported.

Chapter 3 is dedicated to the definition of the governing equations of the fluid problem. The Navier-Stokes equations are presented in both the Eulerian and the Lagrangian frameworks. Constitutive laws are described for Newtonian and Bingham fluids. A model for the extension to 3D flow-like landslides is presented.

Chapter 4 deals with the Finite Element discretization of the equations presented in chapter 3. Moreover the so called fractional step method, the adopted stabilization techniques and the linearisation of the solving system are presented. Then, a description of the adopted numerical method is introduced.

Chapter 5 describes the slip boundary conditions for granular materials. A special mixed Eulerian-Lagrangian formulation is introduced for the elements on the basal interface to accommodate the new slip conditions into the numerical method.

Chapter 6 presents the validation of the model by simulating laboratory tests and the critical role of the basal slip is elucidated. In particular the simulations

of the chute of a granular mass along inclined planes and on an erodible substrate are presented.

Chapter 7 is dedicated to the numerical simulations of three real events. The first large scale simulation is one of the Cougar Hill dump fails with is used to validate the model on irregular topography. Then, the simulations of two historical cases, the Frank avalanche and the Vajont slide, are presented.

Chapter 8 offers an overall summary of the work, conclusions and indications of future work.

2

Landslides simulations: a survey

In this chapter, an introduction to granular matter and experimental tests of granular flows are presented. Then, a landslide classification, with a focus on flow-like landslides, is given and a briefly presentation of some historical cases is reported. Some of the described experimental tests and real events will be discussed in detail and numerically simulated in chapter 6 and 7, respectively.

2.1 Granular matter, granular flows and experimental tests

The term "granular matter" describes a large assemblage of small grains but with a sufficient mass to neglect Brownian motion and dissipating energy whenever they interact. Grains are discrete solid components that are dispersed in one or more fluids and can exhibit solidlike behavior or fluidlike behaviors. "If we measure it by tons, the material most manipulated by man is water; the second most manipulated is granular material" (de Gennes, 1999).

Granular flows are large collections of solid moving particles. The study of granular flows is interesting due to the large number of industrial processes and applications but also for their connections to landslides. The transport of seeds, rice, corn, sugar, coffee, rocks or chemical and pharmaceutical products like pills and powders are just some examples of industrial applications. Phenomena like the motion of red blood cells in small vessels, traffic flow or planetary rings are studied in bio-engineering, transportation engineering and astrophysics, respectively.

In the civil engineering, all type of landslides involve a granular solid phase, in fact rock avalanches, debris flows, snow avalanches and pyroclastic flows are mostly composed by granular matter. In the last decades the attention on this field has grown quickly and some theories have been developed. One of the most widely used theories for the description of granular flow is the Kinetic theory. In (Lun et al., 1984) an idealized granular material consisting of identical spherical particles is studied using statistical methods close to those used in the kinetic theory of gases. In addition to the shape of particles, other hypothesis are at the basis of the kinetic theory: the material is dry, the grains are cohesionless, frictionless and elastic and the collision between them is considered random, binary, instantaneous and uncorrelated. Over the time, some of these hypothesis have been removed and the kinetic theory has grown rapidly, just as the interest in this field and its applications (Yoon et al., 2005; Forterre and Pouliquen, 2008).

To provide direct field observations of landslides is extremely difficult. The reconstructions of real events have often been made with information from visual observers and with in situ analysis of the terrain. For this reason the number of field observations is limited and exhaustive data cannot be recovered from real cases. On the other hand, laboratory experiments with granular material can be done to extrapolate information on both material properties and propagation mechanisms. In fact, laboratory experiments with granular material are increasingly being used to validate theories of landslides propagation. Even if

a satisfactory agreement of the computational model with laboratory data still does not confirm that the theory is adequate to describe a large scale process in nature, experimental tests can help to develop better models.

In (Manzella and Labiouse, 2013) laboratory experiments which consist on releasing dry rigid non-cohesive grains or small bricks on an inclined plane have been designed to investigate rock avalanche propagation mechanisms and to identify parameters influencing their deposit characteristics. In Hutter et al., 1995 laboratory experiments of an initially stationary mass of cohesionsless granular material down on a rough curved bed are presented. Empirical and analytical analyses of laboratory granular flows to investigate rock avalanche propagation are described in Manzella and Labiouse, 2009. In Azanza et al., 1999 a two dimension channel is used to measure the kinematics and the structure of the granular flow. Experiments to investigate the rapid downslope motion of deforming masses of solid grains and intergranular fluids have been developed to understand the behavior of rapid mass movements on irregular surfaces (Iverson et al., 2004). In Barbolini et al., 2005 a low cost system is used to estimate the concentration and velocity profiles in rapid granular flows, in the front, body and tail of the moving mass and in Bartelt et al., 2007 the basal shear force and the basal velocity measurements have been applied to study the basal frictional behaviour of granular material.

2.2 Landslides classification

The word landslide indicates a vast variety of processes that have in common downward and outward movements of slope-forming materials such as rock, soil, artificial fill or a combination of these. Geologists, engineers, and other professionals often adopt slightly differing definitions of landslides because of the complex nature of the phenomenon and because of the large number of related disciplines.

In the literature, the most comprehensive classification is due to Varnes, 1978,

see Figure 2.3. Landslides are one of the most important geomorphological processes shaping the surface of the Earth (Anderson and Anderson, 2010).

Figure 2.1 describes the main parts in which a landslide can be subdivided. Depending of the magnitude and size of the landslides, the moving material can be sorted material like gravel, sand, silt and clay or unsorted material like debris, earth, rock and mud. A review on different classifications can be found in Hungr et al., 2001.

In the description of a landslide some surfaces are significant, in particular for the type of movements that are here considered. The original ground surface and the final ground surface, which determine the geomorphic change, are respectively the ground surface before and after the event, while often a surface of rupture or separation is recognizable, often called basal surface. The volume between the original ground surface and the surface of rupture contains the moving material, which can grow due to erosion or other phenomena.

Figure 2.2 shows a series of different landslides. They can be classified into different groups on the basis of the type of movement and the type of material involved.

Movements, internally describing how the mass is displaced, are fall, topple, slide, spread or flow. Thus, landslides are described using two terms that refer respectively to material and movement; rockfall, debris flow, and so forth and depending on the velocity magnitude, flow or for extremely high velocity the term avalanche is used.

Landslides may also exhibit a complex failure encompassing more then one type of movement(that is, rock slide-debris flow) (Highland and Bobrowsky, 2008). This work focuses on landslides with high velocity, that are normally associated with long runout. In particular, with reference to Figure 2.2, the type of movements that will be treated are the slides and flows (or avalanche) and a combination of them.

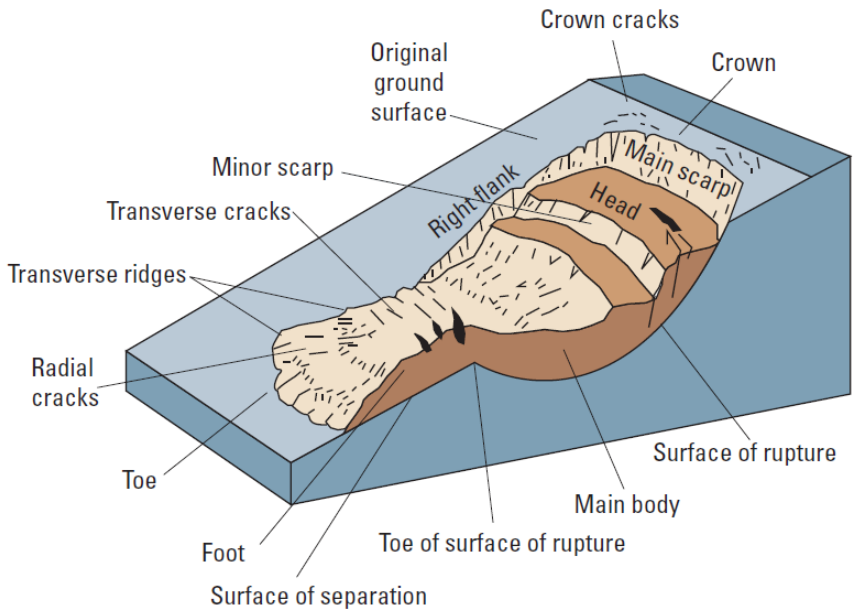

Figure 2.1: A simple illustration of a rotational landslide that has evolved into an earthflow. Imagine illustrates commonly used labels for the parts of a landslide (Varnes, 1978)

Slides

"A slide is a downslope movement of a soil or rock mass occurring on surfaces of rupture or on relatively thin zones of intense shear strain" (Varnes, 1978). It can be rotational, with a curved surface of rupture, or translational with a relatively planar surface of rupture and the velocity range of the travel is variable from very slowl (1 meter every year) to rapid. In general, rapid ones are of rotational type.

Flows

"A flow is a spatially continuous movement in which surfaces of shear are short-lived, closely spaced, and usually not preserved. The distribution of velocities in the displacing mass resembles the one in a viscous liquid. The lower boundary of displaced mass may be a surface along which appreciable differential movement has taken place or a thick zone of distributed shear" (Cruden and Varnes, 1996).
Often, there is a gradation of change from slides to flows, depending on the water content, mobility, and evolution of the movement.

Debris Flow

"Debris flow is a very rapid to extremely rapid flow of saturated non-plastic debris in a steep channel" (Hungr et al., 2001). The materials involved are loose soil, rock and organic matter which combined with water can behave like a slurry that flows downslope. Sometimes a debris flow can be the evolution of a rotational or translational slide in which the mass loses cohesion during the motion, due to the increasing velocity or the change in water content. Occasionally it could be a dry flow, that can occur in cohesionelss sand (sand flows). The velocity of travel can be rapid to extremely rapid (> 5 m/s) depending on density and slope angle.

Lahars, volcanic debris flows, are a particular class of debris flows character-

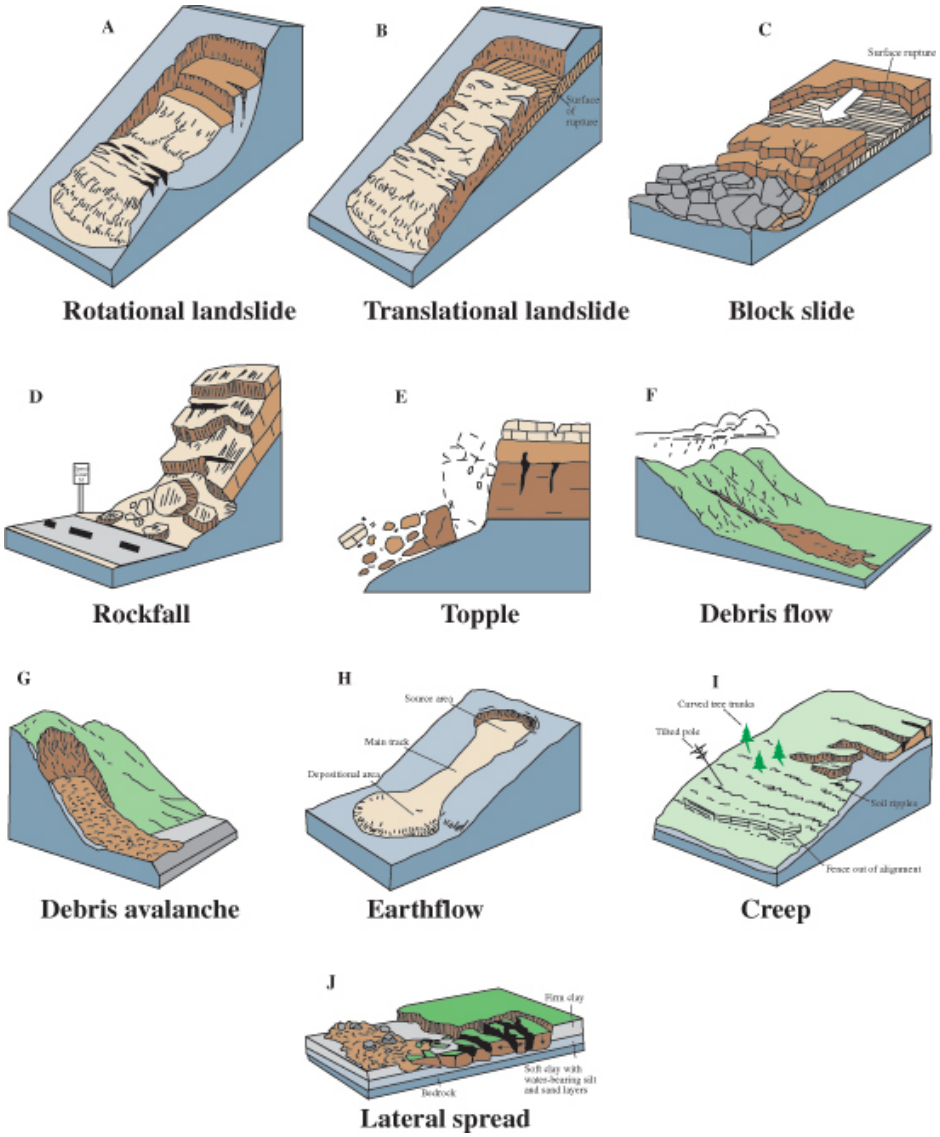

Figure 2.2: These schematics illustrate the major types of landslide movement (Highland and Bobrowsky, 2008)

TYPE OF MOVEMENT		TYPE OF MATERIAL		
		BEDROCK	ENGINEERING SOILS	
			Predominantly coarse	Predominantly fine
FALLS		Rock fall	Debris fall	Earth fall
TOPPLES		Rock topple	Debris topple	Earth topple
SLIDES	ROTATIONAL	Rock slide	Debris slide	Earth slide
	TRANSLATIONAL			
LATERAL SPREADS		Rock spread	Debris spread	Earth spread
FLOWS		Rock flow (deep creep)	Debris flow (soil creep)	Earth flow
COMPLEX		Combination of two or more principal types of movement		

Figure 2.3: Types of landslides. Abbreviated version of Varnes' classification of slope movements (Varnes, 1978)

ized by a mix of water and ash coming from a volcano. The word "lahar" is an Indonesian term, sometimes the term volcanic mudflow is used. Lahar behavior is similar to the concrete, like a fluid when in motion and like a solid when at rest. Some of the largest and most deadly lahars have originated from eruptions, with a travel distance of hundreds kilometers and can become larger as they gain speed and accumulate debris (Thouret et al., 1998).

Debris Avalanche

Debris avalanche is an extremely rapid flow of resulting fragmented debris in steep slope. The debris are formed due to the collapse of an unstable slope and are transported downslope. Generally, debris avalanches are large and if sufficient water is present, the avalanche can become a debris flow or a lahar. The travel distance is large, and the transport material can be up to one or more kilometers in size. They are rapid to extremely rapid, they can travel close to 100 m/s depending especially on the inclination of the slope. Debris avalanches can be also the result of volcanic activity including volcanic earthquakes or the injection of magma, which causes slope instability, (Highland and Bobrowsky, 2008).

Rock Avalanche

Rock avalanches are large masses of rock debris that move rapidly down a mountain slope, smashing everything in their path. Rock avalanche are among the most dangerous landslides phenomena, in fact they can mobilize more than one million cubic meters, with a huge area of propagation and deposition.
The term appeared for the first time in the report of the Frank slide in Alberta (McConnell and Brock, 1904). This event will be discussed in detail later on.

Earthflow

Earthflows can occur in soils made of clay or silt, but also in the presence of a clay-bearing bedrock. Normally, on gentle to moderate slopes. The movement of the mass, which is composed by fine to very fine grains, determines that the earthflow behaves as plastic or/and viscous flow with strong internal deformation. Slides may also evolve downslope into earthflows. The travel velocity can range from very slow (creep) to rapid.

Mudflow

A mudflow is a "very rapid to extremely rapid flow of saturated plastic debris in a channel, involving significantly greater water content relative to the source material" (Hungr et al., 2001).

2.2.1 Case History

Here are described some historical cases. Some of these cases will be used as tests for numerical simulations and will be discussed in more detail in chapter 7. They will be identify on the basis of the classification presented above.

Sarno and Quindici, 1998

On 5th-6th May 1998, more than a hundred individual mass movements occurred along the slope of Pizzo d'Alvano massif, in Campania region, where landslides hit the towns of Bracigliano, Sarno, Siano and Quindici. This towns, located approximately 30 km east of Naples, were badly affected with signifi-

Figure 2.4: Sarno and Quindici landslides

cant destruction. In fact, from the source area located in the upper part of the basins, the post-failure stages originated rapid and extremely rapid landslides that traveled down-slope and then propagated in highly urbanized areas. The total involved soil volume was about $2,000,000\ m^3$ of which 40% derived from the eroded materials along the channels.

The triggering phenomenon was an intense rainfall as measured by the rain gauges located at the toe of the Pizzo d'Alvano massif. In this tragedy 161 people lost their lives. Due to the relevant property damage and loss of human life, many contributions have been made to analyze the phenomenon. The landslides are classified as mudflows (Figure 2.4) (Del Prete et al., 1998; Cascini et al., 2008).

Lituya Bay, 1958

Lituya Bay is located on the northeast shore of the Gulf of Alaska. The event, occurred in 1958, is probably one of the most famous and well-studied event. The landslide was triggered by an 8.3 magnitude earthquake which mobilized a huge

part of the rock mountain along the shore of the bay.

The landslide was triggered impulsively by fault movement and intense earthquake vibrations. It is highly probable that the entire mass plunged into Gilbert Inlet as a rigid body at the time of the earthquake. The estimated volume of $30.6 \cdot 10^6\ m^3$ slid down in the Gilbert Inlet at the head of Lituya Bay, causing a huge wave.

According to the trimline of forest destruction, including tree uprooting and overturning, and erosion down to bedrock over a spur located at the opposite side in the Gilbert Inlet, the wave ran up to an elevation of 524 m, the highest recorded history (see Figures 2.5 and 2.6).

Two or three fishing boats in the bay were sunk and two people were killed by a 30 m high water wave travelling seaward at about 150-200 km/h. The number of causalities remained very low, compared with the scale of the event, only because of the absence of human villages in the surroundings, whereas the entire shore suffered extensive destruction (Fritz et al., 2009; Miller, 1960).

This is an example of multi-hazard event where the landslide interacts with a fluid mass generating a huge wave.

Vajont, 1963

Unfortunately landslides effects elsewhere have been more catastrophic in terms of lost lives. For instance in the 1963 Vajont reservoir disaster, over 2000 people were killed and it is considered the most disastrous landslide that occurred in the XX century. It has sadly become a famous engineering disaster caused by the failure to control the effects of reservoir filling upon the stability of Monte Toc, on the left bank of the dam reservoir. Subsequently, a huge landslip drained approximately $270 \cdot 10^6\ m^3$ of soil into the newly created reservoir (see Figure 2.7).

This did not make the dam collapse, but triggered two destruction mechanisms: a first water wave reached the village of Casso, located 260 m above the lake level in the opposite shore; afterwards, the dam was over-topped by 245 m.

Figure 2.5: View of Lituya Bay. The detached mass is indicated.

Then, a water wave of an estimated 30 millions m^3 descended down the valley, initially more than 70 m in height, destroying the villages of Longarone, Pirago, Villanova, Rivalta and Fae (Ward and Day, 2011; Kilburn and Petley, 2003). The landslide is classified as rockslide, due to the predominant translation movement. Also in this case, the catastrophic effects are related to the wave generated.

Frank, 1903

The Frank Slide of 1903 was the deadliest landslide disaster of Canadian history. It was a very large and rapid slope movement occured near the town of Frank, Alberta, Canada in 1903 (McConnell and Brock, 1904). It is classified as rock avalanche. With its 36 10^6 m^3 of moving material the landslides destroyed a part of the town of Frank, with 73 causalities. The rock detached from the ridge of Turtle Mountain, crossed talus aprons and glacial drift benches and covered the floodplain of Crownest River and the opposite hillside.

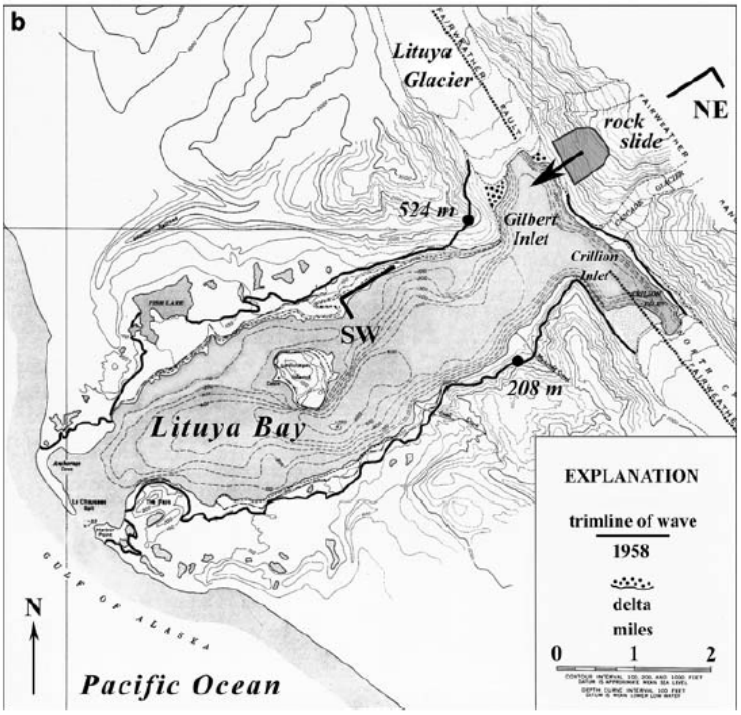

Figure 2.6: Lituya Bay. The dark line indicates the run up of the landslide generated wave.

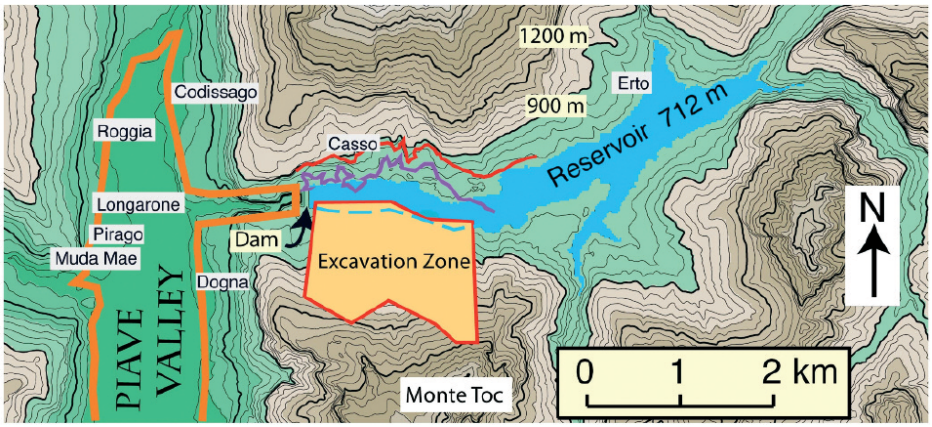

Figure 2.7: Vajont reservoir disaster. Map showing topographic and bathymetric contours and trimline of generated wave runup.

Figure 2.8: View of the Frank avalanche from the Turtle Mountain

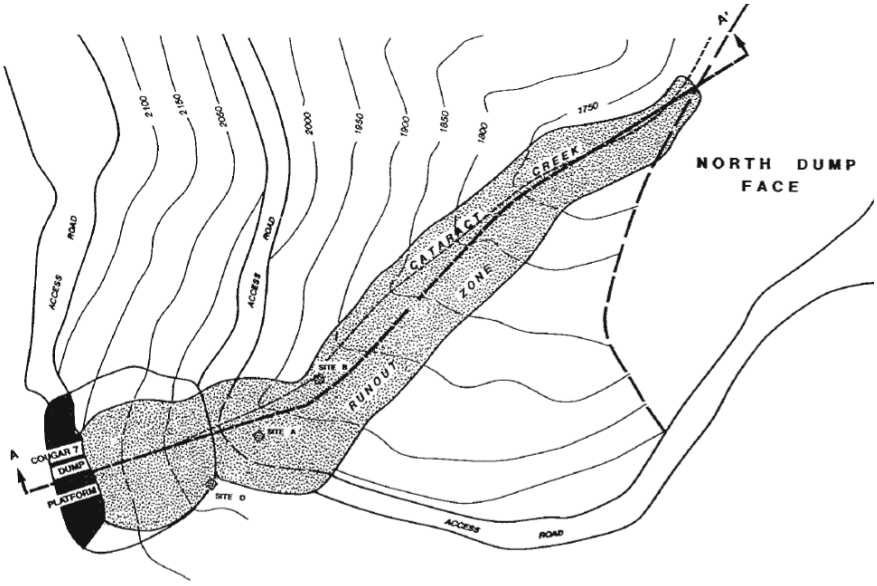

Figure 2.9: Debris flow, The Cougar Hill landslide

Cougar Hill, 1992

On May 11, 1992, the Cougar 7 dump at the Greenhills Mine located near Elkford, British Columbia, failed. Approximately 200,000 m^3 of failure debris slid off the 100 m high waste dump, traveled across an access roadway, and flowed downslope for a total runout distance of 700 m. A service truck and driver traveling along the access road near the dump toe were swept off the road by the failure material. Figure 2.9 shows a plan of the area affected by the debris flow. The dump was constructed in the winter of 1991 between February and May. Heavy rains occurred during the spring of 1991. The failure occurred very rapidly and the debris attained considerable velocity. The runout debris of the Cougar 7 dump consisted predominantly of sandy gravel materials (Dawson et al., 1998; Pastor et al., 2014).

Figure 2.10: Picture of the Fei Tsui landslide

Fei Tsui, 1995

The Fei Tsui landslide occurred on August 1995 in the Chai Wan area, Honk Kong, on a 60 degrees slope in weathered volcanic rock, grading from moderately to completely decomposed tuff. It involved $14 \cdot 10^3$ m^3 of material with two groundwater systems, the regional groundwater table and a perched water table. The causes are described as a combination of a weak material together with the groundwater recharge following a prolonged heavy rainfall. The maximum width of the mobilized mass was 90 m, and the distance travelled 70 m, after which the landslide piled some 6 m up against a corner of the Baptist Church building. Figure 2.10 shows a general view of the landslide. The failure suggested that this was a translational rock slide - debris flow (Knill, 2006; Pastor et al., 2014).

2.3 Numerical methods for the simulation of 3D landslides

Traditional research on landslides has focused on the determination of reliability of slopes and on the study of the failure risk. An overview of traditional approach can be found in Schuster and Highland, 2007.

The prediction of run-out distances and velocity requires a complete mathematical model of the phenomenon. This work is focused on the simulation of the dynamic evolution of a landslide in an unstable slope whit emphasis on the determination of macroscopic quantities, such as the runout distance and the shape of the final deposit.

In the literature, approaches for the simulation of a propagating landslide usually belong to one of two main groups: approaches based on discrete models and approaches based on continuum models.

The Discrete Element Method (DEM) is a typical example of a discrete model. The landslide is described by a set of particles of different shapes which interact between each other through contact forces. The material constitutive behavior plays a role only in the contact between particles making the definition of the forces the crucial part of the method. Examples of the use of DEM for the simulation of landslide can be found e.g. in Calvetti et al., 2000; Taboada and Estrada, 2009; Lu et al., 2014. In Martelloni et al., 2013, a Molecular Dynamics approach, an alternative discrete scheme, has been proposed for modeling the triggering and propagation of landslides caused by rainfall.

Continuum models treat the landslide material as a continuum medium. Starting from the balance equations (mass, momentum and energy conservation), models with different levels of complexity can be considered. These equations can be formulated for all the involved phases (solid particles, fluid and gas) (Pudasaini, 2012; Pitman and Le, 2005), or for one single homogeneous phase representing the material overall behavior.

A common simplification in continuum models consists of integrating the

equations of motion along the vertical axis (Savage and Hutter, 1989). The 2D depth-integrated model is simple and can provide accurate results in terms of velocity of propagation, time to reach a particular place and depth of the flow. These models have been widely used to describe flow-like landslides (Hutter and Koch, 1991; Gray et al., 1999; Quecedo et al., 2004; McDougall and Hungr, 2004). However, in the case of high velocities and accelerations in the depth direction or rough or irregular basal surfaces, depth integrated models can hardly be applicable. Details about depth-average models and a complete bibliography can be found in the recent overview by Pastor et al., 2015.

From the numerical point of view, starting from the equations of motion of the continuum problem, different methods have been proposed. In continuum models, equations of motion can be formulated in different frameworks, leading to different numerical approaches. Smoothed Particle Hydrodynamics (SPH), originally conceived for astrophysical problems, has been successfully applied to model catastrophic landslides (McDougall and Hungr, 2004). In particular, the group of Pastor has studied different aspects of the use of SPH for landslide simulations (see for example Pastor et al., 2015, 2009b and the reference therein).

Methods based on structured and unstructured grids have also been proposed. In Berger et al., 2011; Pitman et al., 2003, depth averaged equations have been solved using the Finite Volume method on rectangular grids with an adaptive remeshing. In Pitman et al., 2003 Finite Volume method has been applied to the simulation of granular avalanches and landslides. In Beguería et al., 2009 the Finite Differences approach is used to describe a debris flow over a complex topography; the proposed approach is again based on a numerical integration of the depth-averaged equations using a shallow water approximation. Another example of the use of Finite Differences in this context can be found in Wang and Sassa, 2010b.

Also the Finite Element Method has been extensively used. In Chen and Lee, 2003 a Lagrangian finite element method has been formulated to reproduce the dynamic runout caused by a landslide. In Crosta et al., 2009 an Arbitrary

Lagrangian-Eulerian approach is used to model entrainment/deposition phenomena in rock and debris avalanches. Quecedo et al., 2004 propose a finite element discretization of the depth-averaged equations using a two step Taylor-Galerkin algorithm. Andersen and Andersen, 2010 present a numerical model, based on Material Point Method (MPM), for studying the dynamic evolution of landslides. In this case the combination of the Langrangian and the Eulerian descriptions allows for the modelling of complex material behavior in the presence of large displacements.

A constitutive model is required by all continuum approaches. Constitutive behaviors can be based on elasto-plastic models or on rheological models. The Bingham model is the simplest model which describes the transition between solid and fluid phases (see e.g. Lagrée et al., 2011 for a comparison with other rheological models). When the shear stress is below a certain threshold, the material behaves like a rigid body, whereas the material flows like a viscous fluid when the limit is exceeded. In frictional models the threshold stress varies with the pressure field and the friction angle (Quecedo et al., 2004). A cohesion can be added to this model (Pastor et al., 2009a). More complex models can also include effects like erosion (Crosta et al., 2009; Oñate et al., 2006)

This work is devoted to the presentation of a numerical approach for the three-dimensional simulation of landslide runouts starting from an unstable slope. A landslide is here intended as a gravity-driven free surface flow (granular flow, mud flow, debris flow, etc.). The numerical analysis of this type of problems requires the ability to track free surfaces and interfaces, in the case that more than one material (e.g. a landslide impinging in a water reservoir (Cremonesi et al., 2011)) is involved, to account for complex constitutive behaviors and possibly for multiphysics phenomena. Different approaches have been developed in order to tracking the free surface, in the Eulerian context. The Height Function method was described in Hirt et al., 1975, in which the free surface is defined by its distance from a reference line. Anther technique is the Volume of Fluid

Method (Hirt and Nichols, 1981) where a function is defined equal to one at any point occupied by the fluid and equal to zero anywhere else. A similar idea is used in the Level Set Method (Osher and Sethian, 1988), which allows to track the free surface starting from the definition of a level set function ϕ, defined as positive inside the domain, negative outside and zero on the interfaces. More recently an edge-based level set finite element method has been proposed, where besides the standard method to track the free surface by convecting the ϕ values with the velocity field $\mathbf{u}$, an extrapolation of the pressure field is used to impose both the pressure boundary condition and the volume conservation (Rossi et al., 2013). Nevertheless, the need of simulating evolving free surfaces and interfaces makes Eulerian approaches still limited in the range of application, in particular, in the context of flow-like landslides the Eulerian approach are less convenient to use. A Lagrangian approach with continuous remeshing, to account for the extremely large deformations and consequent mesh distortion, based on the so-called Particle Finite Element Method (PFEM) (Onate et al., 2004) is here adopted. The PFEM is a finite element method originally developed for the simulation of fluid dynamics, including free surface flows and breaking waves (Larese et al., 2008; Idelsohn et al., 2004), and fluid-structure interaction problems (Idelsohn et al., 2006, 2008; Cremonesi et al., 2010). The method has been applied and validated on a large number of different problems, including simulations of landslides (Zhang et al., 2015) and of landslide generated water waves (Cremonesi et al., 2011; Salazar et al., 2015, 2012). Coupled poromechanics problems have been studied with PFEM (Larese et al., 2012), where the a Lagrangian model is used for the structure behavior while the Eulerian approach, with a level set technique for the tracking of the free surface, is used for the fluid. This method has been applied in the study of overtopping and failure of rockfill dams (Larese et al., 2013).

3

Mathematical description of the fluid dynamics problem and its extension to flow-like landslides

This chapter is dedicated to the definition of the governing equations of the fluid problem. The Navier-Stokes equations are presented in both the Eulerian and the Lagrangian frameworks. A regularization is adopted to describe the Bingham behaviour and the apparent viscosity is introduced. Then a model for the extension to 3D flow-like landslides, described as elastic-viscoplatic materials, is presented and, following the idea used for the Bingham fluids, the apparent viscosity is defined.

3.1 The fluid dynamics problem

Fluid dynamics is the branch of mechanics that studies the behavior of fluids (liquids and gases) in motion. A fluid is a material substance and can be described

in terms of its elemental components, atoms and molecules. In the intent to apply classical mechanics laws to this type of description, the model must consider the molecules as rigid bodies that move in the space and interact each other through both actions depending on the distance (attraction/repulsion) and collisions.

Willing to compute the molecular number N_m in 1 cm^3 of gas (for example air), the state equation $PV = nRT$ in the standard condition ($P = 101325$ Pa, $T = 288$ K and with $R = 8.314 \frac{\mathrm{J}}{\mathrm{mol\,K}}$), gives $N_m = 2.5 \times 10^{18}$. A so huge number can explain why this approach does not have the possibility to be adopted in these conditions. Even if the motion of all the particles would be determined, the enormous quantity of information could not be used with benefit. Furthermore, spatial scales corresponding to the investigating phenomenon are enormously greater than the spatial scales at the molecular level.

This argument can easily be extended to the case of granular flows and fast landslides. In the first case the number of the small size grains, of the order of 1-10 mm, is very high compared to the released volume (in the laboratory experiments that will be presented in Chapter 6 cases from 3 to 20 l are considered). As regards fast landslides, the size of the moving material components (granular matter, rock blocks etc..) are very variable but the size of the domain can be enormous (order of millions m^3) making again a discrete approach not feasible.

Hence, in the adopted macroscopic approach, the material is described as a continuous medium where each spatial point in a specific instant owns physical and mechanical proprieties, like velocity, pressure, density and so on. To the continuum hypothesis it is immediately associated the concept of field, intended as the spatial distribution of a certain macroscopic physical quantity, which can be a scalar quantity (e.g. pressure), or a vector one (e.g. velocity). The physical-mathematical model which describes the behavior of a fluid, then, refers to a macroscopic representation. Nevertheless, later on, the concept of fluid particle, understood as a macroscopic fluid with homogeneous properties will be used.

A fluid can be defined as a substance that deforms continuously under the action of shear stress (Vigevano, 2003). The fluid, which is then regarded as a

continuous medium, can be modeled using equations of conservation. The resolution of the fluid problem treated in this work involves the solution of differential equations to calculate velocities and pressures, and other quantities, in each point of the domain. Such equations, formulated by Claude-Louis Navier and George Gabriel Stokes, can be expressed in different ways.

In particular, in the Eulerian or spatial formulation fluid proprieties are a function of the current configuration $\mathbf{x}$ and time t within a defined domain, called control volume, and in the Lagrangian or material formulation, where proprieties are observed following the evolution of a single particle, they are function of the reference configuration $\mathbf{X}$ and time t. Many fluid dynamics problems are solved in the Eulerian framework, such as for example, the motion of a fluid inside a pipe. Other problems are instead characterized by highly variable domains and not defined a priori, for example the advancement front of a landslide or any problem characterized by a more or less quickly evolving free surface. Writing the equations in a framework or in another one involves some important differences.

3.2 The Navier-Stokes equations

In a moving domain $\Omega \subset \mathbb{R}^n$ with $n = 2, 3$ with the boundary $\partial\Omega_t$, the Navier-Stokes equations for a compressible fluid are given by the following partial differential system of equation:

$$\begin{aligned} \rho \frac{\partial \mathbf{u}}{\partial t}\Big|_X &= \nabla_x \cdot \boldsymbol{\sigma} + \rho \mathbf{b} \quad \text{in } \Omega_t \times (0,T) \\ \frac{\partial \rho}{\partial t}\Big|_X &+ \nabla_x \cdot \mathbf{u} = 0 \quad \text{in } \Omega_t \times (0,T) \end{aligned} \tag{3.1}$$

where $\mathbf{u} = \mathbf{u}(\mathbf{x}, t)$ is the velocity field, $\boldsymbol{\sigma} = \boldsymbol{\sigma}(\mathbf{x}, t)$ is the Cauchy stress tensor, $\rho(\mathbf{x})$ the material density and $\mathbf{b}(\mathbf{x}, t)$ is the external forces per unit mass. The symbol ∇_x represents the gradient operator with respect to the current configuration $\mathbf{x}$ and the derivative $\frac{\partial}{\partial t}\big|_X$ is the total (or material) derivative. The system of equations (3.1) describes the motion of a homogeneous fluid in the domain Ω_t.

The problem has to be supplemented with an appropriate initial condition:

$$\mathbf{u} = \mathbf{u}_0 \qquad \text{in}\,\Omega_{t=0} \tag{3.2}$$

while standard Dirichlet and Neumann boundary conditions are imposed on the boundary $\partial\Omega_t$. On Γ_t^D Dirichlet boundary conditions are imposed on velocities and on Γ_t^N Neumann boundary conditions are imposed on surface tractions:

$$\begin{aligned} \mathbf{u}(\mathbf{x},t) &= \bar{\mathbf{u}}(\mathbf{x},t) \qquad \text{on}\,\Gamma_t^D \times (0,T) \\ \boldsymbol{\sigma}(\mathbf{x},t)\cdot\mathbf{n} &= \mathbf{h}(\mathbf{x},t) \qquad \text{on}\,\Gamma_t^N \times (0,T) \end{aligned} \tag{3.3}$$

where $\bar{\mathbf{u}}(\mathbf{x},t)$ and $\mathbf{h}(\mathbf{x},t)$ are assigned functions and $\mathbf{n}$ is the outward normal to the boundary and $\Gamma_t^D + \Gamma_t^N = \partial\Omega_t$.

The scalar equation in $\Omega_t \times (0,T)$

$$\left.\frac{\partial\rho}{\partial t}\right|_X + \rho\nabla_x\cdot\mathbf{u} = 0 \tag{3.4}$$

represents the mass conservation. For incompressible fluids density is constant and the equation reduces to:

$$\nabla_x\cdot\mathbf{u} = 0 \qquad \text{in}\,\Omega_t \times (0,T) \tag{3.5}$$

According to the definition of the derivative $\left.\frac{\partial}{\partial t}\right|_X$ and the reference configuration the Eulerian or Lagrangian formulation is obtained. The Eulerian approach is based on the mathematical concept of field, and the fluid properties (speed, pressure, density etc.) are defined in terms of space and time. The observer is attached to the fixed or inertial reference system and takes photos of the velocity and pressure field in each moment without any information on the movement of each individual particle. In this work the Lagrangian approach has been privileged. The following paragraph contains a detailed description of this approach.

3.3 The Lagrangian framework

In the material formulation, the Navier-Stokes equations describe the motion of a single particle and the physical properties are directly attributed to

the particle according to its movement and time. The difference between the two approaches is mathematically evident in the terms containing the temporal derivative: given a quantity M of the same particle, the total derivative in the Eulerian framework is expressed as:

$$\frac{\partial M}{\partial t}\Big|_X = \frac{\partial M}{\partial t}\Big|_x + \frac{\partial M}{\partial x}u_x + \frac{\partial M}{\partial y}u_y + \frac{\partial M}{\partial z}u_z \tag{3.6}$$

The total time derivative considers the variation of M of the same particle over time, where the values of M are related to different spatial positions while the partial derivative considers the variation of M of a same geometric point in the interval dt and is therefore referred to different particles. The total and partial derivative differ for the convective term that contains the spatial derivatives of the quantity M multiplied by the corresponding components of velocity. The fact that in the Lagrangian description, the domain (the mesh) varies with particles motion determines an important advantage compared to the Eulerian formulation: the nonlinear convective term disappears.

Consider a mass with initial configuration $\mathcal{B}_0$ occupying the volume Ω_0 with boundary $\partial\Omega_0$. The body undergoes a motion described by a deformation mapping $\chi(\mathbf{X}, t)$, where $\mathbf{X}$ denotes the position of a material particle in the reference configuration, while the corresponding position in the current configuration $\mathcal{B}_t$ at time t occupying the volume Ω_t with boundary $\partial\Omega_t$, is defined by

$$\mathbf{x} = \chi(\mathbf{X}, t) \tag{3.7}$$

The motion of a material point relates the material coordinates $\mathbf{X}$ with the spatial ones $\mathbf{x}$. This is described by the transformation χ as follow:

$$\chi : \Omega_0 \times (0, T) \longrightarrow \Omega_t \times (0, T) \tag{3.8}$$

$$(\mathbf{X}, t) \longmapsto \chi(\mathbf{X}, t) = (\mathbf{x}, t) \tag{3.9}$$

where Ω_t represents the spatial domain and Ω_0 the material reference domain and the physical time t is measured for the same variable in both descriptions (Donea and Huerta, 2003).

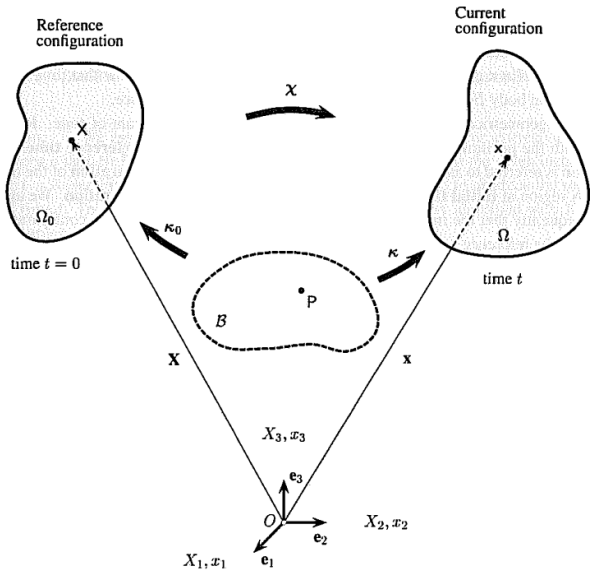

Figure 3.1: Configuration and motion of a continuum body (Holzapfel, 2000)

The differential of the previous relation takes the form

$$dx_i = \frac{\partial x_i}{\partial X_\alpha} dX_\alpha \qquad \mathbf{dx} = \mathbf{F}\mathbf{dX} \tag{3.10}$$

where the second order tensor $\mathbf{F}$ is the deformation gradient.

$$\mathbf{F}(\mathbf{X}, t) = \frac{\partial \chi(\mathbf{X}, t)}{\partial \mathbf{X}} = \nabla_X \mathbf{x} \tag{3.11}$$

Supposing that the inverse transformation exists, $(\mathbf{X}, t) = \chi^{-1}(\mathbf{x}, t)$ then

$$\mathbf{F}^{-1}(\mathbf{x}, t) = \frac{\partial \chi^{-1}(\mathbf{x}, t)}{\partial \mathbf{x}} \tag{3.12}$$

The volume variation at time t can be calculated as :

$$dx = J(\mathbf{X}, t) dX \tag{3.13}$$

where J is the determinant of $\mathbf{F}$. Consider the three non-complanar line elements $\mathbf{dX}_1$, $\mathbf{dX}_2$, $\mathbf{dX}_3$ at the point $\mathbf{X}$ in $\mathcal{B}_0$ so that

$$\mathbf{dx}_i = \mathbf{F}\mathbf{dX}_i \qquad i = 1, 2, 3 \tag{3.14}$$

in accordance with (3.10), therefore

$$dV = \mathbf{dX}_1 \cdot (\mathbf{dX}_2 \wedge \mathbf{dX}_3) = \det(\mathbf{dX}_1, \mathbf{dX}_2, \mathbf{dX}_3) \tag{3.15}$$

The corresponding volume dv in the deformed configuration is

$$dv = \det(\mathbf{x}_1, \mathbf{x}_2, \mathbf{x}_3) = \det(\mathbf{F}\,\mathbf{dX}_1, \mathbf{F}\,\mathbf{dX}_2, \mathbf{F}\,\mathbf{dX}_3) = (\det \mathbf{F})dV \equiv JdV \tag{3.16}$$

The determinant of $\mathbf{F}$ is called J, the volume ratio or Jacobian determinant, the ratio of the current volume of a small element with respect to its reference volume. The condition of impenetrability of matter requires that

$$J = \det \mathbf{F} > 0 \tag{3.17}$$

For incompressible fluids $dV = dv$ and therefore $J = 1$.

Considering a small surface $\mathbf{dS} = \mathbf{N}dS$ in $\mathcal{B}_0$, a cylinder of volume $dV = \mathbf{dX} \cdot \mathbf{dS} > 0$, with a suitable choice of $\mathbf{dX}$.

$$dv = JdV \Rightarrow \mathbf{dx} \cdot d\mathbf{s} = J\mathbf{dX} \cdot d\mathbf{S} \tag{3.18}$$

where $\mathbf{dx}$ and $\mathbf{ds}$ represent the deformation of $\mathbf{dX}$ and $\mathbf{dS}$ respectively. The previous relation using equation (3.10) becomes

$$\mathbf{F}\,\mathbf{dX} \cdot \mathbf{ds} = \mathbf{dX} \cdot \mathbf{F}^T\mathbf{ds} = J\mathbf{dX} \cdot \mathbf{dS} \tag{3.19}$$

The last relation can be expressed in the following form, known as Nanson's formula (Holzapfel, 2000; Ogden, 1997)

$$\mathbf{n}ds = J\mathbf{F}^{-T}\mathbf{N}dS \tag{3.20}$$

which represents the transformation of an oriented element from the surface area dS of normal $\mathbf{N}$ in the initial configuration to the surface area $\mathbf{n}ds$ in the current configuration.

Returning to the deformation expressed in the form

$$\mathbf{x} = \chi(\mathbf{X}, t) \tag{3.21}$$

for an arbitrary choice of reference configuration, the velocity of the material particle which is assigned the place $\mathbf{X}$ in the reference configuration is denoted by

$$\mathbf{U}(\mathbf{X},t) = \frac{\partial \chi}{\partial t}(\mathbf{X},t) \tag{3.22}$$

In the Eulerian specification the notation $\mathbf{u}(\mathbf{x},t)$ has been used for the velocity of the material particle which occupies the place $\mathbf{x}$ at time t. The velocity is the same even if expressed in the two different configuration, that means

$$\mathbf{U}(\mathbf{X},t) = \mathbf{u}(\mathbf{x},t) \tag{3.23}$$

Now it is possible to compute the relation between the gradient of the velocity in both configuration:

$$\mathbf{U}(\mathbf{X},t) = \mathbf{u}(\mathbf{x},t) = \mathbf{u}(\chi(\mathbf{X},t)) \;\Rightarrow\; \nabla_X \mathbf{U} = \nabla_x \mathbf{u}\,\mathbf{F} \tag{3.24}$$

Starting from Nanson's formula (3.20), a relation similar to equation (3.24) can be obtained also for the divergence of a second order tensor: is possible to obtain the relation for the divergence of the Cauchy stress in the current and reference configuration:

$$\nabla_x \cdot \boldsymbol{\sigma} = \frac{1}{J} \nabla_X \cdot (J \boldsymbol{\sigma} \mathbf{F}^{-T}) \tag{3.25}$$

Relation (3.25) is known as Piola transformation (Holzapfel, 2000; Marsden and Hughes, 1994). To introduce the equations of motion in the Lagrangian framework, an important identity may be introduced:

$$\nabla_X \cdot (J \mathbf{F}^{-T}) = 0 \tag{3.26}$$

which can be proved integrating equation (3.26) over the domain Ω_0, applying the divergence theorem twice and using the Nanson's formula (3.20):

$$\int_{\Omega_0} \nabla_X \cdot (J \mathbf{F}^{-T}) d\Omega_0 = \int_{\partial \Omega_0} J \mathbf{F}^{-T} \mathbf{N} d\Gamma_0 = \int_{\partial \Omega_t} \mathbf{n} d\Gamma = \int_{\Omega_t} \nabla_x \cdot \mathbf{I} d\Omega_t = 0 \tag{3.27}$$

3.3.1 The Navier-Stokes equations in the Lagrangian framework

applying Piola's transformation to equation 3.1, the momentum equation becomes:

$$\rho \frac{D\mathbf{U}}{Dt} = \frac{1}{J}\nabla_X \cdot \mathbf{\Pi} + \rho \mathbf{b} \quad \text{in } \Omega_0 \times (0,T) \tag{3.28}$$

where $\mathbf{\Pi} = J\boldsymbol{\sigma}\mathbf{F}^{-T}$ is the first Piola-Kichhoff tensor. For a incompressible fluid the mass conservation implies the volume conservation.

$$\frac{D(\rho d\Omega)}{Dt} = \frac{DJ}{Dt} = J\mathbf{F}^{-T} : \nabla_X \mathbf{U} = 0 \tag{3.29}$$

$$J\mathbf{F}^{-T} : \nabla_X \mathbf{U} = \nabla_X \cdot (J\mathbf{F}^{-1}\mathbf{U}) - \nabla_X \cdot (J\mathbf{F}^{-T})\mathbf{U} \tag{3.30}$$

Using the identity (3.26) the mass conservation equation in the Lagrangian formulation becomes:

$$\nabla_X \cdot (J\mathbf{F}^{-1}\mathbf{U}) = 0 \quad \text{in } \Omega_0 \times (0,T) \tag{3.31}$$

Equations (3.28) and (3.31) represent the Lagrangian form of Navier-stokes equations. In the Lagrangian approach, the nonlinearity is due to the fact that the current configuration differs by large displacements from the original one; this nonlinearity appears in the equations through the deformation gradient $\mathbf{F}$. The boundary $\Gamma_0 = \partial\Omega_0$ is partitioned in two non-overlapping subsets Γ_0^D and Γ_0^N, such that $\Gamma_0^D \cup \Gamma_N^0 = \Gamma_0$ and $\Gamma_0^D \cap \Gamma_N^0 = \emptyset$. Typical boundary conditions for the problem in the Lagrangian framework are:

$$\begin{aligned} \mathbf{U}(\mathbf{X},t) &= \bar{\mathbf{U}}(\mathbf{X},t) \qquad \text{on } \Gamma_0^D \times (0,T) \\ \mathbf{\Pi}(\mathbf{X},t)\cdot\mathbf{N} &= \mathbf{H}(\mathbf{X},t) \qquad \text{on } \Gamma_0^N \times (0,T) \end{aligned} \tag{3.32}$$

where $\bar{\mathbf{U}}(\mathbf{X},t)$ and $\mathbf{H}(\mathbf{X},t)$ are assigned functions and $\mathbf{N}$ is the outward normal to the boundary Γ_0^N

3.4 Newtonian and Bingham fluids

In the previous sections the equations of motion for a homogeneous incompressible fluid have been introduced. For a Newtonian isotropic incompressible

fluid the Cauchy stress tensor $\boldsymbol{\sigma} = \boldsymbol{\sigma}(\mathbf{x}, t)$ is related to the velocity $\mathbf{u} = \mathbf{u}(\mathbf{x}, t)$ and the pressure $p = p(x, t)$ as follow

$$\boldsymbol{\sigma} = -p\mathbf{I} + \boldsymbol{\sigma}_D \tag{3.33}$$

where $\mathbf{I}$ is the identity tensor and $\boldsymbol{\sigma}_D$ is defined as:

$$\boldsymbol{\sigma}_D = 2\mu\dot{\boldsymbol{\varepsilon}}(\mathbf{u}) = \mu(\nabla_x \mathbf{u} + \nabla_x \mathbf{u}^T) \tag{3.34}$$

where $\dot{\boldsymbol{\varepsilon}}(\mathbf{u})$ represents the symmetric part of the velocity gradient. From the incompressibility constraint ($\nabla_x \cdot \mathbf{u} = 0$) it follows that $\boldsymbol{\sigma}_D$ is the deviatoric stress tensor. The tensors $\boldsymbol{\sigma}_D$ and $\dot{\boldsymbol{\varepsilon}}$ are linearly related through the viscosity μ which is a material property. Typical examples of Newtonian fluids are water and common oils. Using (3.33) and (3.34) the momentum balance equation $(3.1)_1$ can be rewritten as

$$\rho \frac{D\mathbf{u}}{Dt}\bigg|_{\mathbf{X}} = -\nabla_x p + \mu \triangle \mathbf{u} + \rho\mathbf{b} \quad \text{in } \Omega_t \times (0, T) \tag{3.35}$$

Using the constitutive relation (3.34), the momentum conservation equation (3.28) in the Lagrangian context takes the form :

$$\rho \frac{D\mathbf{u}}{Dt} = -\frac{1}{J}\nabla_X \cdot (Jp\mathbf{F}^{-T}) + \frac{1}{J}\mu\nabla_X \cdot [J(\nabla_X \mathbf{U})\mathbf{F}^{-1}\mathbf{F}^{-T}] + \rho\mathbf{b} \quad \text{in } \Omega_0 \times (0, T) \tag{3.36}$$

The hypothesis of linearity between $\boldsymbol{\sigma}_D$ and $\dot{\boldsymbol{\varepsilon}}$ through the dynamic viscosity μ is valid for Newtonian fluids. For a non-Newtonian fluid the relation can be written in more general terms as:

$$\boldsymbol{\sigma}_D = \boldsymbol{\sigma}_D(\dot{\boldsymbol{\varepsilon}}(\mathbf{u}), t) \tag{3.37}$$

Among the non-Newtonian fluids, the Bingham fluid plays a particular role. A Bingham fluid is a material that behaves as a rigid body at low shear stresses but starts flowing as a Newtonian viscous fluid once a certain shear stress σ_{D0} (yield stress) is reached. Once the yield stress is achieved, a linear relation between

shear strain rate and shear stress is considered. The Bingham behaviour, in the one dimensional framework, can be described as

$$\begin{aligned} \dot{\gamma} &= 0 \qquad && \sigma_D < \sigma_{D0} \\ \sigma_D &= \sigma_{D0} + \mu\dot{\gamma} \qquad && \sigma_D > \sigma_{D0} \end{aligned} \tag{3.38}$$

where $\dot{\gamma}$ is the shear strain rate. This behaviour introduces a nonlinear effect in the constitutive law. The Bingham law, accounting for different behaviours before and after the yield stress, has a piecewise form, which can be difficult to be dealt with numerically. Thus, an approximation based on a regularization of equations (3.38) will be introduced.

Here, following the idea of Papanastasiou, 1987, and later implemented by Cremonesi et al., 2011; Larese, 2012, an approximation based on an exponential evolution of the viscosity is introduced

$$\sigma_D = \left[\mu + \frac{\sigma_{D0}}{|\dot{\gamma}|}(1 - e^{-N|\dot{\gamma}|})\right]\dot{\gamma} \qquad \text{for } |\dot{\gamma}| \neq 0 \tag{3.39}$$

which holds both on the yielded ($\sigma_D < \sigma_{D0}$) and unyelded ($\sigma_D > \sigma_{D0}$) regions. In the approximation (3.39) the definition of the parameter N is required. In Figure 3.2 the Newtonian and Bingham fluid is compared with the exponential approximation for two different values of the parameter N. Figure 3.2 also shows that a quick stress growth can be achieved at very low strain rate with a relatively large exponent N, which is consistent with the behaviour of the Bingham material before the yield stress. In the limit of $N \longrightarrow \infty$, the Bingham behaviour in the yielded regions is recovered. The real advantage of eq. (3.39) is that it leads to a system of equations of motion solvable by algorithms very similar to those used for a Newtonian fluid.

Approximation (3.39) can also be expressed through an apparent viscosity $\bar{\mu}$, leading to

$$\begin{aligned} \sigma_D &= \tilde{\mu}\dot{\gamma} \\ \tilde{\mu} &= \mu + \frac{\sigma_{D0}}{|\dot{\gamma}|}\left(1 - e^{-N|\dot{\gamma}|}\right) \end{aligned} \tag{3.40}$$

Figure 3.3 shows the apparent viscosity of the exponential approximation for two different values of the parameter N and for a Newtonian and Bingham fluid.

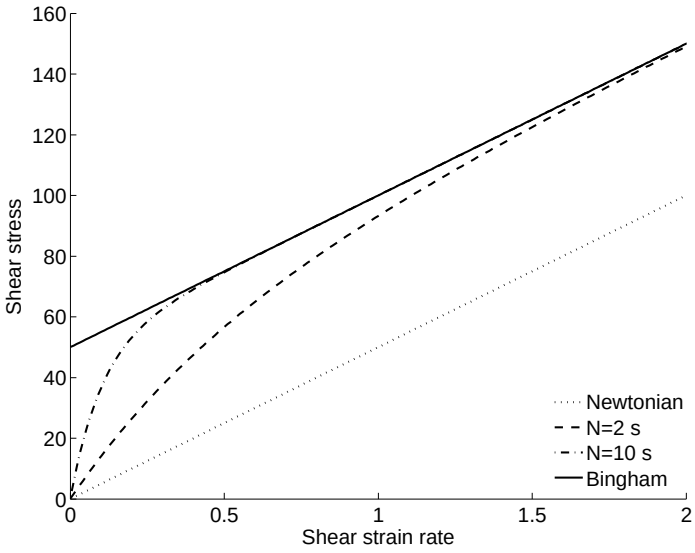

Figure 3.2: Newtonian and Bingham fluids compared with the exponential approximation for two different values of the parameter N ($\mu = 50$ Pa s; $\sigma_{D0} = 50$ Pa).

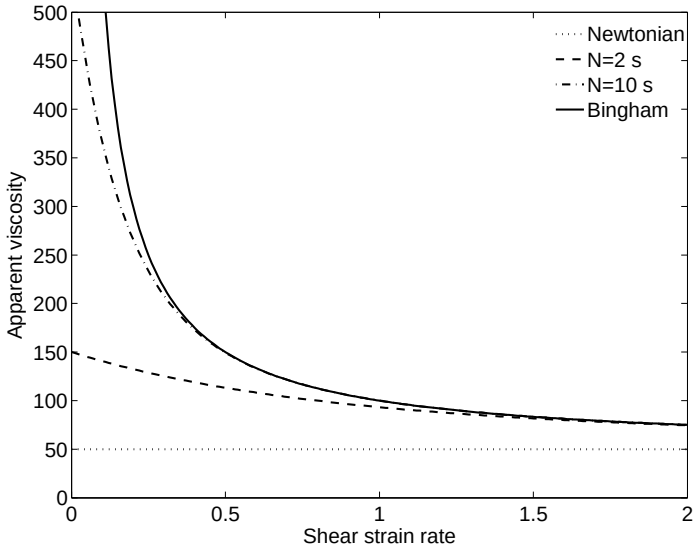

Figure 3.3: Apparent viscosity of the Newtonian and Bingham fluid compared with the exponential approximation for two different values of the parameter N ($\mu = 50$ Pa s; $\sigma_{D0} = 50$ Pa).

The apparent viscosity concept, illustrated in a one dimensional case, can be extended to tridimensional cases to express the deviatoric tensor $\boldsymbol{\sigma}_D$ in terms of the symmetric part of the velocity gradient.

$$\boldsymbol{\sigma}_D = 2\tilde{\mu}\dot{\boldsymbol{\varepsilon}}(\mathbf{u}) \tag{3.41}$$

where the definition of the apparent viscosity now is:

$$\tilde{\mu} = \mu + \frac{\sigma_{D0}}{||\dot{\boldsymbol{\varepsilon}}||}(1 - e^{-N||\dot{\boldsymbol{\varepsilon}}||}) \tag{3.42}$$

In equation (3.42) $||\dot{\boldsymbol{\varepsilon}}||$ is the Euclidean norm of the symmetric part of the gradient of the strain rate tensor $\dot{\boldsymbol{\varepsilon}}(\mathbf{u})$

3.5 Extension to 3D flow-like landslides

Landslide runouts involve extremely large deformations of the moving soil mass. For this reason, in the literature they have been modeled mainly by considering the soil as a viscous fluid. This assumption implies that the initial, statically equilibrated state cannot be included in the model and the transition from stable slope configuration to an unstable moving landslide cannot be described.

In this work, the moving mass is modeled as a rigid-viscoplastic solid undergoing large deformations. This implies that also in this case only the landslide motion can be described. The assumed rigid-viscoplastic behavior is obtained by simply neglecting the elastic part of the behavior of an elastic-viscoplastic material model. In contrast, the modeling of the soil evolution from its initially stable equilibrium configuration to the final unstable state of running landslide will require consideration of the complete elasto-viscoplastic material behavior.

3.5.1 Kinematics

Considering the deformation gradient, its polar decomposition in terms of the left stretch tensor $\bar{\mathbf{V}}$ and of the rotation tensor $\mathbf{R}$ is given by:

$$\mathbf{F} = \bar{\mathbf{V}}\,\mathbf{R} \tag{3.43}$$

The left Cauchy-Green tensor is defined by

$$\bar{\mathbf{B}} = \mathbf{F}\,\mathbf{F}^T = \bar{\mathbf{V}}\,\bar{\mathbf{V}}^T \tag{3.44}$$

where $\bar{\mathbf{B}}$ and $\bar{\mathbf{V}}$ are used to differentiates the tensors from the nodal velocities and external forces, that will be used later. In the literature the left Cauchy-Green tensor $\bar{\mathbf{B}}$ is sometimes referred as Finger deformation tensor. Any objective deformation measure can be used to define the strain energy function, but also functions of objective deformation measures can be used for this purpose. An often used function is the logarithm of the left stretch tensor $\bar{\mathbf{V}}$:

$$\boldsymbol{\varepsilon} = \ln \bar{\mathbf{V}} \tag{3.45}$$

which is coaxial with the left stretch tensor since taking the logarithm is an isotropic tensor function, and the principal values of $\boldsymbol{\varepsilon}$ are obtained as $\ln \lambda_i$ with λ_i the principal stretches. The so-called eulerian logarithmic strain tensor can be also be expressed as (De Borst et al., 2012):

$$\boldsymbol{\varepsilon} = \frac{1}{2} \ln \bar{\mathbf{B}} \tag{3.46}$$

The strain tensor $\boldsymbol{\varepsilon}$ is decomposed into volumetric and deviatoric parts according to the following standard additive split.

$$\boldsymbol{\varepsilon} = \boldsymbol{\varepsilon}_D + \varepsilon_V \mathbf{I} \tag{3.47}$$

$$\varepsilon_V = \frac{1}{3} \mathrm{tr} \boldsymbol{\varepsilon} = \frac{1}{3} \ln J \tag{3.48}$$

$$\boldsymbol{\varepsilon}_D = \boldsymbol{\varepsilon} - \varepsilon_V \mathbf{I} = \ln \bar{\mathbf{V}}_D \tag{3.49}$$

where $\mathbf{I}$ is the identity tensor and $\bar{\mathbf{V}}_D$ is the deviatoric part of the left stretch tensor $\bar{\mathbf{V}}$

$$\bar{\mathbf{V}}_D = J^{-1/3} \bar{\mathbf{V}} \Rightarrow \det \bar{\mathbf{V}}_D = 1 \tag{3.50}$$

The usual multiplicative decomposition of the deformation gradient $\mathbf{F}$ into its elastic $\mathbf{F}^e$ and plastic $\mathbf{F}^p$ parts is assumed (Lubarda, 2004; Simo and Hughes, 2006):

$$\mathbf{F} = \mathbf{F}^e \, \mathbf{F}^p \qquad \mathbf{F}^e = \bar{\mathbf{V}}^e \, \mathbf{R}^e, \; \mathbf{F}^p = \bar{\mathbf{V}}^p \, \mathbf{R}^p \tag{3.51}$$

with obvious meaning of symbols.

Making use of equation (3.11) the time derivative is

$$\dot{\mathbf{F}} = \frac{\partial}{\partial t} (\nabla_X \mathbf{x}) = \nabla_X \mathbf{U} \tag{3.52}$$

The superposed dot will be used henceforth to denote the time derivative $\partial / \partial t$.

Indeed, using equation $(3.24)_2$, the spatial velocity gradient $\nabla_x \mathbf{u}$ can be easily expressed as

$$\mathbf{l} = \nabla_x \mathbf{u} = \dot{\mathbf{F}} \, \mathbf{F}^{-1} \tag{3.53}$$

According to the decomposition of equation (3.51), the spatial velocity gradient is expressed as:

$$\mathbf{l} = \mathbf{l}^e + \mathbf{F}^e \, \mathbf{L}^p \, \mathbf{F}^{e-1} = \mathbf{l}^e + \mathbf{l}^p \tag{3.54}$$

where

$$\mathbf{l}^e = \dot{\mathbf{F}}^e \, \mathbf{F}^{e-1}, \quad \mathbf{L}^p = \dot{\mathbf{F}}^p \, \mathbf{F}^{p-1} \tag{3.55}$$

define the spatial elastic and plastic velocity gradients, respectively. Note that while $\mathbf{l}^p$ is defined in the current configuration, $\mathbf{L}^p$ is defined in the intermediate configuration. The plastic velocity gradient in the current configuration is given by $\mathbf{l}^p = \mathbf{F}^e \mathbf{L}^p \mathbf{F}^{e-1}$.

The elastic and plastic velocity gradients $\mathbf{l}^e$ and $\mathbf{l}^p$ can be split in the sum of their symmetric and antisymmetric components:

$$\mathbf{l}^e = \frac{1}{2}(\mathbf{l}^e + \mathbf{l}^{eT}) + \frac{1}{2}(\mathbf{l}^e - \mathbf{l}^{eT}) = \mathbf{d}^e + \mathbf{w}^e \tag{3.56}$$

$$\mathbf{l}^p = \frac{1}{2}(\mathbf{l}^p + \mathbf{l}^{pT}) + \frac{1}{2}(\mathbf{l}^p - \mathbf{l}^{pT}) = \mathbf{d}^p + \mathbf{w}^p \tag{3.57}$$

where $\mathbf{d}^e$, $\mathbf{d}^p$ define the elastic and plastic rate of deformation tensors, and $\mathbf{w}^e$, $\mathbf{w}^p$ the corresponding spin tensors. As it is customary in plastically isotropic solids, $\mathbf{w}^p = 0$ is assumed, and therefore:

$$\mathbf{l} = \mathbf{d}^e + \mathbf{d}^p + \mathbf{w}^e = \nabla_x \mathbf{u} \tag{3.58}$$

3.5.2 Material model

Let $\boldsymbol{\tau} = J\boldsymbol{\sigma}$ be the Kirchhoff stress tensor. The deviatoric components of the Kirchhoff stress is given by

$$\boldsymbol{\tau}_D = J\boldsymbol{\sigma}_D \tag{3.59}$$

Elastic strains in soils are usually small, so that a Hencky type linear relation is assumed between Kirchhoff stresses and logarithmic strains

$$\boldsymbol{\tau}_D = \rho_0 \frac{\partial \Psi}{\partial \boldsymbol{\varepsilon}^e} = 2G\boldsymbol{\varepsilon}^e_D + K\varepsilon^e_V \mathbf{I} \tag{3.60}$$

where $\boldsymbol{\varepsilon}^e = \ln \mathbf{V}^e$, ρ_0 is the density in the reference configuration, G is the shear modulus, K the bulk modulus and

$$\Psi(\boldsymbol{\varepsilon}^e) = \frac{1}{2}\boldsymbol{\varepsilon}^e : \mathbf{E} : \boldsymbol{\varepsilon}^e \tag{3.61}$$

is the free energy potential per unit mass, $\mathbf{E}$ being the constant isotropic fourth order elasticity tensor.

The elastic domain is assumed to be bounded by a Drucker-Prager like condition with zero cohesion

$$q - \alpha J p \tan\varphi \leq 0 \tag{3.62}$$

where $q = \sqrt{\frac{3}{2}\boldsymbol{\tau} : \boldsymbol{\tau}}$ is the Kirchhoff effective stress, α is a material constant and φ is the material internal friction angle, which is assumed here to be constant. A non-associative, non-dilatant viscoplastic flow rule is assumed, whereby the purely deviatoric plastic strain rate is expressed as the gradient of a viscoplastic potential $g(\boldsymbol{\tau}) = q(\boldsymbol{\tau})$

$$\mathbf{d}^p = \frac{f}{\mu}\frac{\partial g}{\partial \boldsymbol{\tau}} = \frac{3}{2\mu}\frac{f}{q}\boldsymbol{\tau}_D \tag{3.63}$$

where μ is the material viscosity and f is a measure of the overstress

$$f = < q - \alpha J p \tan\varphi > \tag{3.64}$$

with $< \square >= \square$ for $\square > 0$, $< \square >= 0$ for $\square \leq 0$. With these definitions, the plastic work density is obtained as

$$\boldsymbol{\tau} : \mathbf{d}^p = \boldsymbol{\tau}_D : \mathbf{d}^p = \frac{3}{2\mu}\frac{f}{q}\boldsymbol{\tau}_D : \boldsymbol{\tau}_D = q\,\dot{\gamma}, \quad \dot{\gamma} = \frac{f}{\mu} \tag{3.65}$$

where $\dot{\gamma}$ is the effective plastic strain rate, conjugate to q in the plastic work.

After the conditions for the slope unstable motion have been met, the landslide runout starts, with negligible elastic strains if compared to the extremely large viscoplastic deformations. In this case, it is customary to assume $\mathbf{d}^e = 0$ in (3.58). Since plastic strain rates are purely deviatoric, the granular flow behaves

as an incompressible non-Newtonian fluid with $J = 1$ and $\boldsymbol{\tau}_D = \boldsymbol{\sigma}_D$. Under these conditions, from (3.63) one can express the deviatoric Kirchhoff stress $\boldsymbol{\tau}_D$ in terms of the plastic strain rate $\mathbf{d}^p$

$$\boldsymbol{\tau}_D = \frac{2}{3}\frac{q}{\dot{\gamma}}\mathbf{d}^p, \quad f > 0 \tag{3.66}$$

But further noting that for $f > 0$ and $J = 1$, from the expression $(3.65)_2$ of $\dot{\gamma}$ and making use of (3.64), q can be expressed as

$$q = \mu\dot{\gamma} + \alpha p \tan\varphi, \quad f > 0 \tag{3.67}$$

one finally obtains

$$\boldsymbol{\sigma}_D = \boldsymbol{\tau}_D = \frac{2}{3}\left(\mu + \frac{\alpha p \tan\varphi}{\dot{\gamma}}\right)\mathbf{d}^p, \quad f > 0 \tag{3.68}$$

The expression in (3.68) defines a Bingham-like frictional rigid viscoplastic behavior and is substantially identical to the one considered e.g. in Quecedo et al. (2004). This can be regularized (Papanastasiou, 1987; Cremonesi et al., 2011; Larese, 2012) defining an effective viscosity $\tilde{\mu}$ accounting for the frictional contributions.

$$\tilde{\mu} = \frac{2}{3}\left[\mu + \frac{\alpha p \tan\varphi}{\dot{\gamma}}\left(1 - e^{-N\dot{\gamma}}\right)\right] \tag{3.69}$$

where N, as before, is a regularization parameter, usually taken equal to 10^3, and setting

$$\boldsymbol{\sigma}_D = \boldsymbol{\tau}_D = \tilde{\mu}\mathbf{d} \tag{3.70}$$

for every arbitrary f, where it has been set $\mathbf{d}^e = \mathbf{0}$, $\mathbf{d} = \mathbf{d}^p$ and $J = 1$. With the additional assumption of $\alpha = 1$, this expression will be used in what follows.

4
Finite Element discretization

In this chapter the Finite Element discretization of the equations discussed in chapter 3 is presented. Moreover the so called fractional step method, the adopted stabilization techniques and the linearisation of the solving system are presented. Then, a description of the adopted numerical method is introduced.

4.1 Weak form and spatial discretization

The system of partial differential equations which governs the motion, has been described in the previous chapter in the Eulerian framework (3.1) and in the Lagrangian framework (3.28) and (3.29). For an incompressible homogeneous material the balance equations can be writtes a:

$$\begin{aligned} \rho \left.\frac{\partial \mathbf{u}}{\partial t}\right|_X &= -\nabla_x p + \tilde{\mu} \triangle \mathbf{u} + \rho \mathbf{b} \quad \text{in } \Omega_t \times (0,T) \\ \nabla_x \cdot \mathbf{u} &= 0 \quad \text{in } \Omega_t \times (0,T) \end{aligned} \tag{4.1}$$

In the following, the standard Dirichlet and Neumann boundary condition, eq. (3.3), are considered:

$$\begin{aligned} \mathbf{u}(\mathbf{x},t) &= \bar{\mathbf{u}}(\mathbf{x},t) \qquad \text{on}\, \Gamma_t^D \times (0,T) \\ \boldsymbol{\sigma}(\mathbf{x},t)\cdot\mathbf{n} &= \mathbf{h}(\mathbf{x},t) \qquad \text{on}\, \Gamma_t^N \times (0,T) \end{aligned} \tag{4.2}$$

In equation $(4.1)_1$ instead of the material viscosity μ (Newtonian fluids), the apparent viscosity for a Bingham like fluid is used, as defined in equation (3.40) (see section 3.4) and in equation (3.40), for a rigid-viscoplastic solid (see section 3.5.2). The Galerkin weak form of the governing equations is written as usual, using trial and test functions, whose existence spaces, for any given $t \in [0,T]$, are defined as

$$\bar{S}(t) = \{\mathbf{u} \in \mathbf{H}^1(\Omega_t) | \mathbf{u} = \bar{\mathbf{u}}\} \qquad \text{on } \Gamma_t^D \tag{4.3}$$

$$\bar{S}_0(t) = \{\mathbf{w} \in \mathbf{H}^1(\Omega_t) | \mathbf{w} = \mathbf{0}\} \qquad \text{on } \Gamma_t^D \tag{4.4}$$

$$\bar{Q}(t) = \{p, q \in \mathbf{L}^2(\Omega_t)\} \tag{4.5}$$

The integral form of the momentum equation can be obtained with a scalar product of the terms in equation $(4.1)_1$ with the test function $\mathbf{w} \in \bar{S}_0$ while in the mass conservation equation $(4.1)_2$ with the $q \in \bar{Q}$ test function.

The variational form reads: find $\mathbf{u} \in \bar{S} \times [0,T]$ and $p \in \bar{Q} \times [0,T]$ such that

$$\begin{aligned} &\int_{\Omega_t} \mathbf{w} \cdot \left(\rho \left. \frac{\partial \mathbf{u}}{\partial t} \right|_X + \nabla_x p - \tilde{\mu} \triangle \mathbf{u} - \rho \mathbf{b} \right) d\Omega_t = \mathbf{0} \quad \forall \mathbf{w} \in \bar{S}_0 \\ &\int_{\Omega_t} q(\nabla_x \cdot \mathbf{u}) = 0 \quad \forall q \in Q \end{aligned} \tag{4.6}$$

Applying the Green formula, the following equations are obtained:

$$\begin{aligned} &\int_{\Omega_t} \mathbf{w} \cdot \rho \left. \frac{\partial \mathbf{u}}{\partial t} \right|_X d\Omega_t - \int_{\Omega_t} p(\nabla_x \cdot \mathbf{w}) d\Omega_t - \int_{\Gamma_t^N} \mathbf{w} \cdot \mathbf{h} d\Gamma_t \\ &+ \int_{\Omega_t} \tilde{\mu} \nabla_x \mathbf{w} \cdot \nabla_x \mathbf{u} d\Omega_t - \int_{\Omega_t} \mathbf{w} \cdot \rho \mathbf{b} d\Omega_t = \mathbf{0} \quad \forall \mathbf{w} \in \bar{S}_0 \\ &\int_{\Omega_t} q(\nabla_x \cdot \mathbf{u}) = 0 \quad \forall q \in Q \end{aligned} \tag{4.7}$$

Similarly, to introduce the variational form of the Lagrangian version of the Navier-Stokes equations, the following space have to be considered:

$$S = \{\mathbf{U} \in \mathbf{H}^1(\Omega_0) | \mathbf{U} = \mathbf{U}_0\} \qquad \text{su } \Gamma_0^D \tag{4.8}$$

$$S_0 = \{\mathbf{W} \in \mathbf{H}^1(\Omega_0) | \mathbf{W} = 0\} \qquad \text{su } \Gamma_0^D \tag{4.9}$$

$$Q = \{p, q \in \mathbf{L}^2(\Omega_0)\} \tag{4.10}$$

The integral form of the momentum equation can be obtained with a scalar product of the terms in equation (3.36) with the test function $\mathbf{W} \in S_0$ while in the mass conservation equation (3.31) with the test function $q \in Q$. Hence the equations are integrated in the domain Ω_0, and the Green formula is applied:

$$\int_{\Omega_0} \rho_0 \frac{\partial \mathbf{U}}{\partial t}\bigg|_X \cdot \mathbf{W} d\Omega_0 = -\int_{\Omega_0} \mu J(\nabla_X \mathbf{U})\, \mathbf{F}^{-1}\mathbf{F}^{-T} : \nabla_X \mathbf{W} d\Omega_0$$
$$+ \int_{\Omega_0} Jp\mathbf{F}^{-T} : \nabla_X \mathbf{W} d\Omega_0 + \int_{\Omega_0} \rho_0 \mathbf{b} \cdot \mathbf{W} d\Omega_0 + \int_{\Gamma_0^N} \mathbf{W} \cdot \mathbf{H} d\Gamma_0^N \qquad \forall \mathbf{W} \in S_0 \tag{4.11}$$

$$\int_{\Omega_0} \nabla_X \cdot (J\mathbf{F}^{-1}\mathbf{U}) q d\Omega_0 = 0 \qquad \forall q \in Q \tag{4.12}$$

To simplify the mathematical description, homogeneous boundary conditions are considered $\mathbf{H}(\mathbf{X}, t) = \mathbf{0}$, $\bar{\mathbf{U}}(\mathbf{X}, t) = \mathbf{0}$ on Γ_0^N and Γ_0^D respectively. The discrete problem relate to equations (4.11)-(4.12) is obtained searching for the solution in the sub spaces $S_h \subset S$, $S_{h,0} \subset S_0$ and $Q_h \subset Q$, which are discrete approximations

of the spaces in which they are included:

$$W_i(\mathbf{X},t) = \sum_{a=1}^{N_{node}} N_a(\mathbf{X})\Theta_{ai}(t) \tag{4.13}$$

$$U_i(\mathbf{X},t) = \sum_{a=1}^{N_{node}} N_a(\mathbf{X})V_{ai}(t) \tag{4.14}$$

$$[\nabla_X U(\mathbf{X},t)]_{ij} = \sum_{a=1}^{N_{node}} V_{ai}(t)\nabla_{X_j}(N_a(\mathbf{X})) \tag{4.15}$$

$$p(\mathbf{X},t) = \sum_{a=1}^{N_{node}} N_a(\mathbf{X})P_a(t) \tag{4.16}$$

$$q(\mathbf{X},t) = \sum_{a=1}^{N_{node}} N_a(\mathbf{X})Q_a(t) \tag{4.17}$$

where $i,j = 1,2,3$, a runs over all the nodes, $V_{ai}(t)$ and P_a are the nodal values of the velocity and pressure, respectively, and Θ_{ai} and Q_a have unit value. The resulting semi-discretized system is therefore

$$\mathbf{M}(x)\frac{D\mathbf{V}}{Dt} + \mathbf{K}(x)\mathbf{V} + \mathbf{D}^T(x)\mathbf{P} = \mathbf{B} \tag{4.18}$$

$$\mathbf{D}(x)\mathbf{V} = 0 \tag{4.19}$$

where $\mathbf{V}$ is the nodal velocity vector and $\mathbf{P}$ the nodal pressure vector.

The matrices $\mathbf{M}$ and $\mathbf{K}$, represent the mass and viscosity matrix of the fluid and $\mathbf{D}$ is the matrix of the discretized divergence operator. Finally $\mathbf{B}$ is the nodal equivalent external forces vector. These matrices can be viewed as the combination of 3×3 nodal matrices, defined as follows

$$\mathbf{M}_{ab} = \int_{\Omega_0} \rho_0 N_a N_b \mathbf{I} d\Omega_0 \tag{4.20}$$

$$\mathbf{D}_{ab} = \int_{\Omega_0} J N_a (\nabla_X N_b)\mathbf{F}^{-1} d\Omega_0 \tag{4.21}$$

$$\mathbf{K}_{ab} = \int_{\Omega_0} \mu J((\nabla_X N_a)\mathbf{F}^{-1}) \otimes ((\nabla_X N_b)\mathbf{F}^{-1}) d\Omega_0 \tag{4.22}$$

$$\mathbf{B}_a = \int_{\Omega_0} \rho_0 \mathbf{b} N_a d\Omega_0 \tag{4.23}$$

where indeces a and b run over the mesh nodes.

In general, the spaces S_h and Q_h cannot be chosen independently, because the pair (S_h, Q_h) is required to satisfy the discrete LBB inf-sup condition (Brezzi and Fortin, 1991):

$$\inf_{q \in Q_h} \sup_{\mathbf{u} \in S_h} \frac{\int_{\Omega_t} q \nabla_x \cdot \mathbf{u} d\Omega_t}{||\mathbf{u}||_{S_h} ||q||_{Q_h}} \geq \delta > 0 \tag{4.24}$$

There are different pairs of approximation spaces that satisfy the condition (4.24), for example the Taylor Hood elements P_2 $/P_1$, where P_2 denotes the set of polynomials of degree less than or equal to 2 while P_1 denotes the set of polynomials of degree less than or equal to 1. In the present work, an equal order interpolation P_1/P_1 has been used for practical reasons, in fact the solution strategy, which will be described in the second part of this chapter, requires a continuous retriangulation and hence the necessity to store all the information in the nodes. For this reason, linear shape functions have to be used for both velocity and pressure. This implies that the stability condition cannot be satisfied and a stabilization technique must be introduced (see section 4.4).

4.2 Time discretization

To solve the incompressible Navier-Stokes system, a time discretization is still necessary. A θ method is here applied to discretize the time interval $[0, T]$, which is considered partitioned into N time steps of same length Δt. For a generic function f, f^n denotes the approximation of $f(t_n)$, $t_n = n \cdot \Delta t$ and $\theta \in [0, 1]$:

$$f^{n+\theta} = \theta f^{n+1} + (1 - \theta) f^n \tag{4.25}$$

The backward-Euler integration scheme is here adopted ($\theta = 1$). Hence, in the time interval $t^n \rightarrow t^{n+1}$, the acceleration and the current position are expressed as follow:

$$\begin{aligned} \frac{D\mathbf{V}}{Dt} &= \frac{\mathbf{V}^{n+1} - \mathbf{V}^n}{\Delta t} \\ \mathbf{x}^{n+1} &= \mathbf{x}^n + \mathbf{V}^{n+1} \Delta t \end{aligned} \tag{4.26}$$

Choosing as a reference the configuration at time t^n the completely discretized system results:

$$\frac{1}{\Delta t}\mathbf{M}(\mathbf{x}^{n+1})(\mathbf{V}^{n+1}-\mathbf{V}^n)+\mathbf{K}(\mathbf{x}^{n+1})\mathbf{V}^{n+1}+\mathbf{D}^T(\mathbf{x}^{n+1})\mathbf{P}^{n+1}=\mathbf{B}^{n+1} \tag{4.27}$$

$$\mathbf{D}(\mathbf{x}^{n+1})\mathbf{V}^{n+1}=\mathbf{0} \tag{4.28}$$

The obtained system can then be expressed as:

$$\mathbf{A}\mathbf{Y}^{n+1}=\mathbf{F}^{n+1} \tag{4.29}$$

where

$$\mathbf{A}=\begin{bmatrix}\mathbf{C} & \mathbf{D}^T\\ \mathbf{D} & \mathbf{0}\end{bmatrix} \tag{4.30}$$

$$\mathbf{Y}^{n+1}=\begin{bmatrix}\mathbf{V}^{n+1}\\ \mathbf{P}^{n+1}\end{bmatrix} \tag{4.31}$$

$$\mathbf{F}^{n+1}=\begin{bmatrix}\mathbf{B}^{n+1}+\frac{1}{\Delta t}\mathbf{M}\mathbf{V}^n\\ \mathbf{0}\end{bmatrix} \tag{4.32}$$

$$\mathbf{C}=\frac{1}{\Delta t}\mathbf{M}+\mathbf{K} \tag{4.33}$$

It should be noted that the matrices in (4.27) and (4.28) are configurational, i.e. their entries are not constant, but depend on the current configuration. As a consequence, the system (4.27)-(4.28) is nonlinear. In this work, this system of equations has been solved using two different approaches, a monolithic scheme or a fractional step scheme. The monolithic approach consists of the direct solution of the linear system (4.29), while the Fractional Step Method is described in what follows.

4.3 Fractional step schemes

The fractional step method (Codina, 2001), is here applied to equations (4.27) and (4.28) to uncouple the pressure and velocity fields, solving a more stable problem of reduced size, introducing an approximation. The three steps of the

algebraic version of the Chorin-Teman projecton method (Chorin, 1967; Temam, 1968) can be summarized as follow:

$$\frac{1}{\Delta t}\mathbf{M}[\tilde{\mathbf{V}}^{n+1} - \mathbf{V}^n] + \mathbf{K}(\mathbf{x}^{n+1})\mathbf{V}^{n+1} + \gamma\mathbf{D}^T\mathbf{P}^n = \mathbf{B}^{n+1} \tag{4.34}$$

$$\frac{1}{\Delta t}\mathbf{M}[\mathbf{V}^{n+1} - \tilde{\mathbf{V}}^{n+1}] + \mathbf{D}^T(\mathbf{P}^{n+1} - \gamma\mathbf{P}^n) = \mathbf{0} \tag{4.35}$$

$$\mathbf{D}\mathbf{V}^{n+1} = \mathbf{0} \tag{4.36}$$

where $\tilde{\mathbf{V}}^{n+1}$ is an auxiliary intermediate velocity, and γ is a scalar parameter. The system of equations (4.34)-(4.35)-(4.36) defines the fractional step method with algebraic decomposition; with $\gamma = 0$ the first order scheme is obtained, while $\gamma = 1$ gives the second order one. Substituting $\tilde{\mathbf{V}}$ from eq. (4.35) into eq. (4.34) the original system of equations is recovered.

An approximation is now introduced in the Fractional Step Method to allow to compute the intermediate velocity in the first step:

$$\mathbf{K}(\mathbf{x}^{n+1})\mathbf{V}^{n+1} \approx \mathbf{K}(\tilde{\mathbf{x}}^{n+1})\tilde{\mathbf{V}}^{n+1} \tag{4.37}$$

$\mathbf{V}^{n+1}$ is expressed as a function of $\tilde{\mathbf{V}}^{n+1}$ through eq.(4.35) and then it is substituted in equation (4.36). The fractional step method is finally formulated in terms of the following system of equations:

$$\frac{1}{\Delta t}\mathbf{M}[\tilde{\mathbf{V}}^{n+1} - \mathbf{V}^n] + \mathbf{K}\tilde{\mathbf{V}}^{n+1} = \mathbf{B}^{n+1} \tag{4.38}$$

$$\Delta t\mathbf{D}\mathbf{M}^{-1}\mathbf{D}^T\mathbf{P}^{n+1} = \mathbf{D}\tilde{\mathbf{V}}^{n+1} \tag{4.39}$$

$$\frac{1}{\Delta t}\mathbf{M}[\mathbf{V}^{n+1} - \tilde{\mathbf{V}}^{n+1}] + \mathbf{D}^T\mathbf{P}^{n+1} = \mathbf{0} \tag{4.40}$$

In the first equation the intermediate velocity is estimated, while at the second and third equations pressures and velocities unknowns are computed, respectively. The scheme allows to uncouple the variables $\mathbf{P}^{n+1}$ and $\mathbf{V}^{n+1}$, introducing the intermediate velocity $\tilde{\mathbf{V}}^{n+1}$ and the approximation given by (4.37).

Other fractional-step methods can be based on the Helmholtz decomposition. Between the algebraic decompositions (see e.g. Guermond et al., 2006 for a review), the same result of the Chorin-Teman projecton method of the first order

can be achieved with an incomplete factorization block **LU** (Perot, 1993; Quarteroni et al., 2000). The advantage of the Fractional step Method is certainly the reduced computational cost in the solution of the linear system. A further advantage of the approach is merely numeric. In fact, in the monolithic scheme a single linear system in the unknowns of velocity and pressure is solved, at each iteration. Because of the different nature of the unknowns, the coefficients of the matrix **A** (equation 4.30) have values that may differ by several orders of magnitude leading to a ill-conditioned matrix.

4.4 Stabilization of the solution

An important advantage of the Lagrangian approach, compared to the Eulerian one, is the absence of convective term, which is a source of numerical instability. On the other hand, the problem of excessive distortion of the elements, due to large deformations undergone by the moving fluid, is solved by a continuous redefinition of the finite element connectivities. However, this procedure makes it necessary to condense all the information on the current state of the model in the nodes, and consequently to use linear shape functions. The choice of equal shape functions for both pressure and velocity does not respect the so-called (Ladyzhenskaya-Babuska-Brezzi) LBB inf-sup compatibility condition (4.24) (Brezzi and Fortin, 1991). This causes spurious oscillations in the pressures field and, therefore, the necessity to add stabilization terms in the weak form of the balance equations.

Various stabilization schemes exist for the monolithic approach. For example, in the Eulerian formulation a pressure-stabilizing Petrov-Galerkin method has been proposed by Tezduyar et al., 1992, for finite Reynold numbers, that has been derived from the well known streamline-upwind/Petrov-Galerkin (SUPG) method (Brooks and Hughes, 1982; Balestra et al., 1986). In the Lagrangian approach followed in this work, the stabilization of the convective term is not required. For this reason, the *pressure-stabilizing/Petrov-Galerkin* (PSPG) sta-

bilization technique (Tezduyar et al., 1992) has been chosen. A modification for the Lagrangian approach can be found in (Cremonesi et al., 2010) and it is here adopted.

In equation (4.12) the additional stabilization term is added, which consists of the integral of the product of a stabilization parameter and of the residual of the momentum conservation equation. As already mentioned, in the Lagrangian formulation the convective term disappears and the stabilization of equation (4.11) is not necessary. The weak form of the mass conservation equation with the PSPG stabilization writes:

$$\int_{\Omega_0} q\,\nabla_X \cdot (J\mathbf{F}^{-1}\mathbf{U})d\Omega_0 + \sum_{e=1}^{N_{el}} \int_{\Omega_0^e} \tau_{pspg}^e \frac{1}{\rho_0}\nabla_X q \cdot \Big(\rho_0 \frac{\partial \mathbf{U}}{\partial t}\Big|_X + \frac{1}{J}\nabla_X \cdot (Jp\mathbf{F}^{-T}) - \frac{1}{J}\mu\nabla_X \cdot (J\nabla_X \mathbf{U}\mathbf{F}^{-1}\mathbf{F}^{-T}) - \rho_0 \boldsymbol{b}\Big) d\Omega_0 = 0 \quad \forall q \in Q \tag{4.41}$$

where the stabilization parameter is defined as:

$$\tau_{pspg}^e = \frac{z_e}{2||\boldsymbol{u}||} \tag{4.42}$$

and z_e is the diameter of the circle with area equivalent to element e. It is possible to introduce a dimensionless parameter α, to improve the stabilization effect:

$$\tau_{pspg}^e = \alpha\frac{z_e}{2||\boldsymbol{u}||} \tag{4.43}$$

Introducing the finite element space discretization, equations (4.11) and (4.41), take the following semi-discretized form:

$$\mathbf{M}(\mathbf{x})\frac{D\mathbf{V}}{Dt} + \mathbf{K}(\mathbf{x})\mathbf{V} + \mathbf{D}^T(\mathbf{x})\mathbf{P} = \mathbf{B} \tag{4.44}$$

$$\mathbf{C}(\mathbf{x})\frac{D\mathbf{V}}{Dt} + \mathbf{D}(\mathbf{x})\mathbf{V} + \mathbf{L}_\tau(\mathbf{x})\mathbf{P} = \mathbf{Q}(\mathbf{x}) \tag{4.45}$$

where the matrices $\mathbf{C}$, $\mathbf{L}_\tau$, $\mathbf{H}$ are defined as:

$$\mathbf{C}_{ab} = \sum_{e=1}^{N_{el}} \int_{\Omega_0^e} \tau_{pspg}^e (\nabla_X N_a) N_b d\Omega_0 \tag{4.46}$$

$$\mathbf{L}_{\tau_{ab}} = \sum_{e=1}^{N_{el}} \int_{\Omega_0^e} \frac{\tau_{pspg}^e}{\rho_0} (\nabla_X N_a) \cdot (\nabla_X N_b) \mathbf{F}^{-1} d\Omega_0 \tag{4.47}$$

$$\mathbf{Q}_a = \sum_{e=1}^{N_{el}} \int_{\Omega_0^e} \frac{\tau_{pspg}^e}{\rho_0} (\nabla_X N_a) \cdot \mathbf{b} d\Omega_0 \tag{4.48}$$

The second order term $\nabla_X \cdot (J \nabla_X \mathbf{U} \mathbf{F}^{-1} \mathbf{F}^{-T})$ in equation (4.41) vanishes for linear (triangular and tetrahedral) elements. The time integrated form of the monolithic system (4.27) and (4.41) can be obtained following the same steps done for write the equation (4.29).

In the Fractional Step Method, introducing the Laplace operator $\mathbf{L}$ in the equation (4.39), (Codina, 2001) gives a stabilization effect. Indeed the matrix product $\mathbf{D}\mathbf{M}^{-1}\mathbf{D}^T$ represents an approximation of the Laplace operator.

$$\mathbf{D}\mathbf{M}^{-1}\mathbf{D}^T \approx \mathbf{L} \tag{4.49}$$

The system of equations, with the Laplace term, is already stabilized.

$$\frac{1}{\Delta t}\mathbf{M}[\tilde{\mathbf{V}}^{n+1} - \mathbf{V}^n] + \mathbf{K}\tilde{\mathbf{V}}^{n+1} = \mathbf{B}^{n+1} \tag{4.50}$$

$$\Delta t \mathbf{L}\mathbf{P}^{n+1} = \mathbf{D}\tilde{\mathbf{V}}^{n+1} \tag{4.51}$$

$$\frac{1}{\Delta t}\mathbf{M}[\mathbf{V}^{n+1} - \tilde{\mathbf{V}}^{n+1}] + \mathbf{D}^T\mathbf{P}^{n+1} = \mathbf{0} \tag{4.52}$$

In the previous equations, the pressure field results stabilized, without imposing any further approximation to velocity or pressure. The system of equations (4.50)-(4.52) can be written in a monolithic scheme substituting the term $\mathbf{V}^n$ with

$$\mathbf{V}^n = \tilde{\mathbf{V}}^n - \Delta t \mathbf{M}^{-1}\mathbf{D}^T\mathbf{P}^n \tag{4.53}$$

equations (4.50)-(4.52) then leads to

$$\frac{1}{\Delta t}\mathbf{M}[\tilde{\mathbf{V}}^{n+1} - \tilde{\mathbf{V}}^n] + \mathbf{K}\tilde{\mathbf{V}}^{n+1} + \mathbf{D}^T\mathbf{P}^n = \mathbf{B}^{n+1} \tag{4.54}$$

$$\mathbf{D}\tilde{\mathbf{V}}^{n+1} - \Delta t\mathbf{L}\mathbf{P}^{n+1} = 0 \tag{4.55}$$

This formulation can be view as a stabilized scheme, where the effect of the product between the Laplace operator and the pressure is comparable to the Galerkin/Least-Squares method (Balestra et al., 1986). A different approach has been proposed by Zienkiewicz and Codina, 1995 where the idea was to rewrite the problem in terms of $\tilde{\mathbf{V}}^{n+1} = \mathbf{V}^{n+1} + \Delta t\mathbf{M}^{-1}\mathbf{D}^T\mathbf{P}^{n+1}$. Equations (4.50)-(4.52), can hence be written as follows:

$$\frac{1}{\Delta t}\mathbf{M}[\mathbf{V}^{n+1} - \mathbf{V}^n] + \mathbf{K}\mathbf{V}^{n+1} + \mathbf{E}(\mathbf{V}^{n+1}) + \mathbf{D}^T\mathbf{P}^{n+1} = \mathbf{B}^{n+1} \tag{4.56}$$

$$\mathbf{D}\mathbf{V}^{n+1} - \Delta t(\mathbf{D}\mathbf{M}^{-1}\mathbf{D}^T - \mathbf{L})\mathbf{P}^{n+1} = \mathbf{0} \tag{4.57}$$

where $\mathbf{E}(\mathbf{V}^{n+1})$ can be thought of as the splitting error, which results to be of order $O(\Delta t)$ (Codina, 2001). The stabilization effects, in this case, is due to the term $\Delta t\mathbf{Q}\mathbf{P}^{n+1}$, where $\mathbf{Q} := \mathbf{D}\mathbf{M}^{-1}\mathbf{D}^T - \mathbf{L}$. In (Zienkiewicz et al., 1998) it is demonstrated that this matrix is semi positive definite.

The introduction of the Laplacian pressure matrix, in the case of free surface problems, requires the imposition of a Dirichlet condition for the pressure at the free surface. So that, in some situations, it can happen that all the nodes of an element belong to the free surface (see for example the element e in figure 4.1). In this case, in all the nodes of the element the pressure is enforced to be zero from the boundary condition and in the third step of the fractional step method (4.52), velocity in not enforced by the pressure to respect the incompressibility constraint. Consequently, mass conservation is not respected leading to possible mass loss. Possible solutions to this problem can be found in Aubry et al., 2006.

In this work, both the stabilized monolithic and fractional step method have been used. In particular, the laboratory tests and the large scale simulations of chapter 6 and 7 have been solved using a fractional step approach.

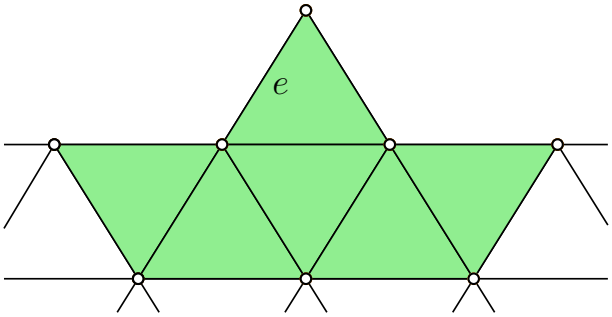

Figure 4.1: Example of element with three nodes on the free surface

4.5 Iterative resolution method

The discritized equations (4.44) and (4.45) in the monolithic approach, and (4.50)-(4.51)-(4.52) in the fractional step approach, are non linear for the presence of the deformation gradient $\mathbf{F}$, hence, have to be solved iteratively at each time step. Following Idelsohn et al. 2006, the Picard method is used here, instead of a full Newton-Raphson scheme (Radovitzky and Ortiz, 1998).

Given the problem:

$$\mathbf{A}(\mathbf{x})\mathbf{x} = \boldsymbol{b}(\mathbf{x})$$

at each iteration the following system has to be solved:

$$\mathbf{A}(\mathbf{x}_{k-1}^{n+1}) \cdot \mathbf{x}_{k}^{n+1} = \boldsymbol{b}(\mathbf{x}_{k-1}^{n+1}) \tag{4.58}$$

The matrix in the equations (4.41) and (4.18), in the monolithic case, or in the equations (4.38), (4.51) and (4.40) in the Fractional Step Method, at iteration k, are evaluated on the configuration of iteration $k-1$. These means that the reference configuration is choose as $\Omega_0 = \Omega_t(t = t_k^n)$. In this case the deformation gradient $\mathbf{F}$ coincides with the identity matrix and $J = 1$, but a re-triangulation has in principle to be performed at every nonlinear iteration (Idelsohn et al., 2004, 2003). The Picard algorithm is preferred to the Newton-Raphson one in order to have less extra storage (Aubry et al., 2005). Iterations are repeated until

the correct geometry at the time step t^{n+1} is found; in particular the following convergence criterion has been used:

$$\frac{||\mathbf{U}_k^{n+1} - \mathbf{U}_{k-1}^{n+1}||}{||\mathbf{U}_{k-1}^{n+1}||} \leq \epsilon \tag{4.59}$$

ϵ being a small number, in this work $\epsilon = 10^{-2}$.

4.6 Descriprion of the numerical method

The numerical method, used in this work, is called Particle Finite Element Method (PFEM), as, in view of the Lagrangian formulation of the problem, the mesh nodes can be interpreted as material particles. The PFEM is a Lagrangian method used to solve efficiently fluid dynamics problems including free-surface flow and breaking waves, but also fluid-structure interactions or fluid-object interactions (Becker et al., 2015; Idelsohn et al., 2006). This method has been applied to different engineering problems and also validated against several experiments (see Idelsohn and Oñate, 2006; Onate et al., 2004; Idelsohn et al., 2006; Larese et al., 2008). It is important to note that there is not a priori specified solution domain, but it must be found from the position of the set of particles: once the domain is identified, it is possible to solve the integral form of the governing differential equations. Indeed, the method is based on a continuous re-meshing of the moving domain, driven by the alpha-shape method and achieved by means of Delaunay triangulation.

4.6.1 The Delaunay Triangulation

An efficient technique to generate a mesh starting from a set of points is the so called Delaunay triangulation, which defines univocally the convex hull that contains the whole set of points. Let us consider a set of N nodes P_i; at each node let us associate a region V_i, as the locus of points X_i such that:

$$d(X_i, P_i) < d(X_i, P_j) \quad \forall i \neq j \tag{4.60}$$

where $d(\mathbf{x}, \mathbf{x_i}) = \|\mathbf{x} - \mathbf{x_i}\|$ is the Eucledian distance. Each region V_i is called

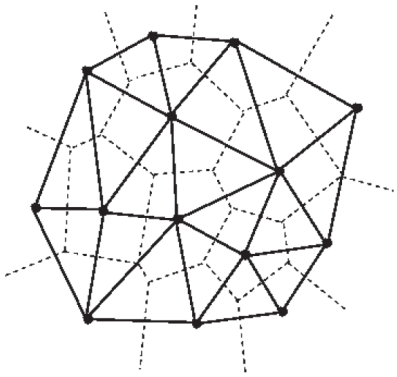

Figure 4.2: Voronoi cells (dashed line) and Delaunay triangulation (solid line).

Voronoi Cell and it is closed and convex if it is internal, whilst open if it is at the boundary. Moreover, the union of all the sides of Voronoi Cells is called Voronoi Diagram. It is worth noting that each side of a Voronoi Cell belongs to two regions T_i and T_j, consequently it is the locus of points equidistant to P_i and P_j. In other words, it lays on the axis of the segment $\overline{P_iP_j}$. Furthermore, each vertex of the Voronoi Diagram belongs to three region V_i, V_j, V_k and for this region it is equidistant to the three points P_i, P_j, P_k; in other words, it is the center of the circumference (Voronoi Sphere) passing through the three points.

The Delaunay triangulation is the dual of the Voronoi Diagram; it can be constructed joining the points P_i, P_j, P_k whose Voronoi Cells have a common boundary. The duality between Delaunay triangulation and Voronoi Diagram, depicted in figure 4.2 can be summarized as follows:

- point of Delaunay triangulation $\longleftrightarrow$ Voronoi region;
- Side of Delaunay triangulation $\longleftrightarrow$ side of Voronoi region;
- Delaunay triangle $\longleftrightarrow$ Voronoi vertex.

The main features of Delaunay triangulation in 2D are listed below:

1. the circle circumscribed to any triangle, does not contain any other node of the triangulation;

2. given a set of nodes in a plane ($\mathbb{R}^2$), Delaunay triangulation is unique unless four or more points lay on the same circumference;

3. Delaunay triangulation maximizes the minimum angle of any triangles of the mesh, i.e. it creates a regular mesh, that is obviously fundamental in FE context;

4. the set given by the union of the generated triangles is the convex hull of the points, in other words it is the convex figure of minimum area that encloses all the points of the set.

In the 3D case, the Voronoi regions are polyhedra and the Delaunay triangles are tetrahedra. In this cases the main features become:

1. the circumsphere of every tetrahedra does not contain any other node of the triangulation;

2. given a set of nodes in a space ($\mathbb{R}^3$), Delaunay triangulation is unique unless five or more points lay on the same sphere;

3. Delaunay triangulation minimizes the maximum radius of a tetrahedra enclosing sphere (the enclosing sphere is the smallest sphere containing a tetrahedra).

4.6.2 Alpha-shape method

In the Lagrangian formulation, the reference volume Ω and its boundary $\partial\Omega$ are defined from the position of the set of nodes (or particles). The Delaunay triangulation determines the minimum convex domain of the set of points but in most cases, in the presence of complex geometry, e. g. with re-entrant corners,

the generated domain does not correspond to the real domain of the problem. An algorithm which eliminates all the exceeding elements is indeed necessary. In figure 4.3(a) a set of points is shown, while in figure 4.3(b) the Delaunay triangulation using tetrahedral elements is performed. The alpha-shape method is used

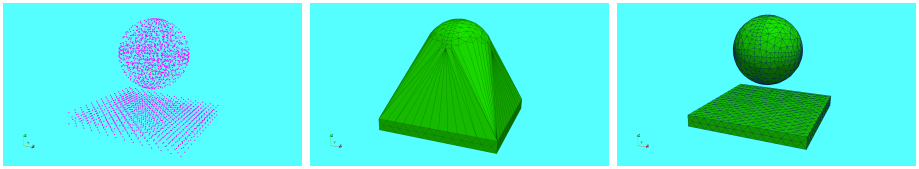

(a) (b) (c)

Figure 4.3: Boundary identification by means of alpha shape method: sphere and horizontal plane.

to eliminate the distorted elements in figure 4.3(c). The idea is to compute a distortion parameter for each elements of the meshed convex domain and eliminate all the elements which do not respect the geometric condition. Here the alpha-shape method (Edelsbrunner and Mücke, 1994) is based on the smallest element h_e and on the radius of the circumsphere R_e of each element. Computed the average smallest edge of all the elements, h, the distortion factor is defined as:

$$\alpha_e = \frac{R_e}{h} \tag{4.61}$$

For a fixed value of α, all the elements with $\alpha_e > \alpha$ (α greater then 1) are eliminated. Figure 4.3(c) shows the real domain after the application of the α-shape correction, which allows the identification of the boundary. Figure 4.4 is another example of application of the described procedure.

This method is also used to identify particles separating from the rest of the domain. When a node belongs only to a distorted tetrahedron or tetrahedra (or triangle in 2D), the element is removed and the particle is separated from the rest of the domain (see figure 4.5(a)). The motion of the isolated particle is then governed exclusively by gravity acceleration and initial velocity. Similarly, the

method allows to add an isolated particle to the fluid domain when it approaches the free surface edge and the new generated tetrahedron (or triangle in 2D) verifies the condition $\alpha_e < \alpha$ (see figure 4.5(b)).

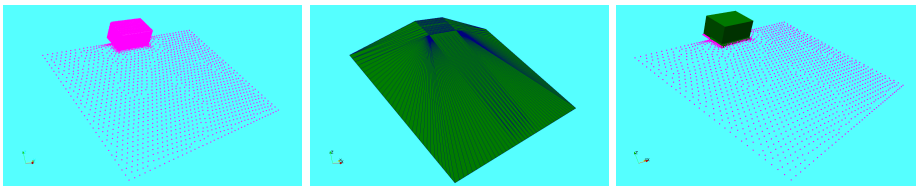

(a) (b) (c)

Figure 4.4: (a) Set of points, (b) Delaunay triangulation, (c) real domain

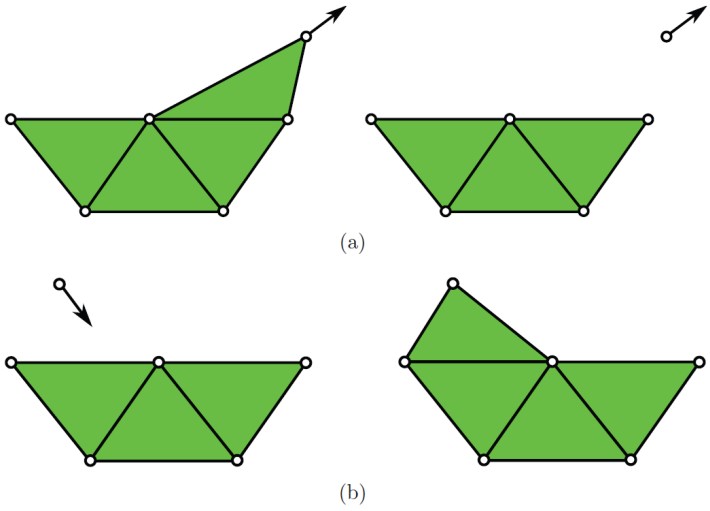

(a)

(b)

Figure 4.5: Separation of a particle (element node) from the bulk (a). Incorporation of a particle when it approaches the bulk (b).

4.6.3 Remeshing strategy

Ideally, in the solution scheme, the triangulation should be performed at every time step. However, to reduce the computing time, the mesh can be regenereted only when it is too distorted in the average. To this purpose, an index of mesh distortion is necessary. Starting from the shape factor α_e, defined in equation (4.61), a simple measure of the mesh quality can be obtained defining for each element a distortion factor β_e

$$\beta_e = \sqrt{3}\alpha_e \geq 1 \quad \textit{in 2D;} \qquad \beta_e = \frac{4}{\sqrt{6}}\alpha_e \geq 1 \quad \textit{in 3D} \tag{4.62}$$

where in 2D the equilateral triangle ($\alpha_e = 1/\sqrt{3}$) and in 3D the regular tetrahedron ($\alpha_e = \frac{4}{\sqrt{6}}$) have been considered as the best possible element. Then the quality of the entire mesh is evaluated by an arithmetic mean over all the N_{el} elements:

$$\beta = \frac{1}{N_{el}} \sum_{e=1}^{N_e l} \beta_e \tag{4.63}$$

The mesh is regenerated only if $\beta > \bar{\beta}$, where $\bar{\beta} > 1$ is a fixed parameter.

4.6.4 Adding and removing particles

In the Lagrangian approach, the particles move as a consequence of the material flow. So it may happen that some particles concentrate in a region of the domain and, on the contrary, in another region the number of particles becomes too low to obtain an accurate solution. To overcome these difficulties in the proposed implementation, the possibility to removing and adding particles has been introduced. In figure 4.6 the highlighted node is removed because the distance from the closest node is too small. Similarly, in figure 4.7, the highlighted node is removed because the node is too close to the boundary. Figure 4.8 shows on the other hand the adding procedure. A node is added into a large element 4.8(a) which is eliminated and three new triangles are formed 4.8(b). In figure 4.8(c) a new Delaunay triangulation is performed. The information on removed particles

is eliminated and new values of pressure and velocity are stored into the added particle through a linear interpolation of the closest nodes. The removed particles compensate the newly added ones, so that the number of the mesh nodes is constant during the entire simulation.

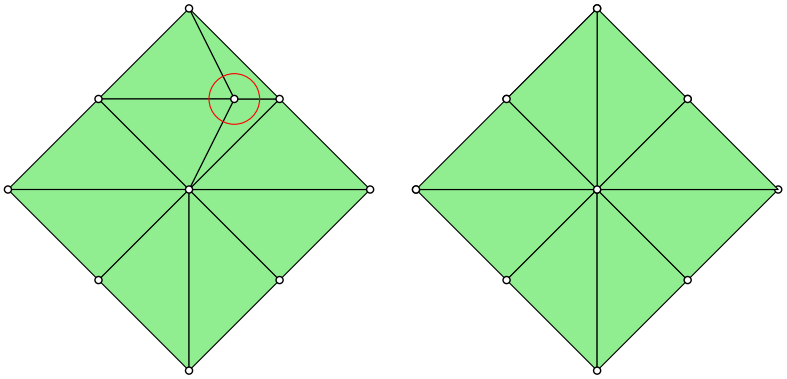

(a) (b)

Figure 4.6: Example of particle removal

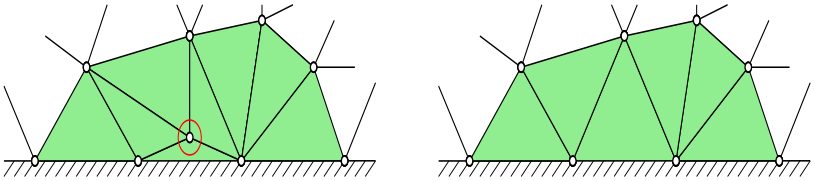

(a) (b)

Figure 4.7: Example of particle removal near the boundary

4.6.5 Summary of the principal steps

The code developed in (Cremonesi et al., 2010) to solve problems with two-dimensional incompressible Newtonian and non-Netonian fluid-like materials is here extended to three-dimensional problems.

The operational steps of the method are:

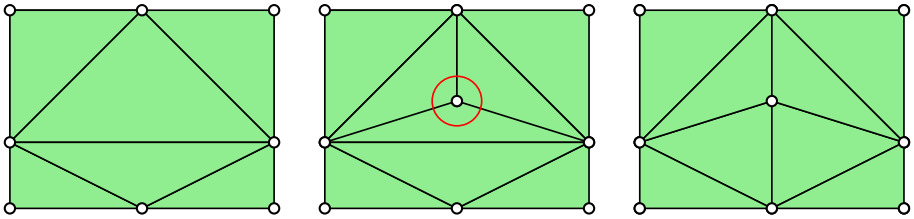

Figure 4.8: Example of particle addition

1. Definition of the material domain as a set of points or particles. The accuracy of the solution depends, obviously, on the considered number of particles (or nodes).

2. Generation of the finite element mesh, triangles for 2D and tetrahedra for 3D (through Delaunay triangulation).

3. Internal and external boundary identification by means of the alpha-shape method.

4. Iterative solution of the nonlinear system of equations in terms of velocity and pressure fields.

5. Definition of the new configuration using values of pressure and velocity obtained in the previous step.

6. Check elements distortion. If the elements are too distorted, then return to step 2.

7. Incrementation of time. Go to step 4 and repeat for the next time step.

From the computational point of view, the largest amount of time is spent for the numerical resolution of the nonlinear system of equations, but also the generation of the mesh and the identification of the boundary can be highly time consuming if the number of nodes is large. In figure 4.9 a flowchart of the solution scheme is presented.

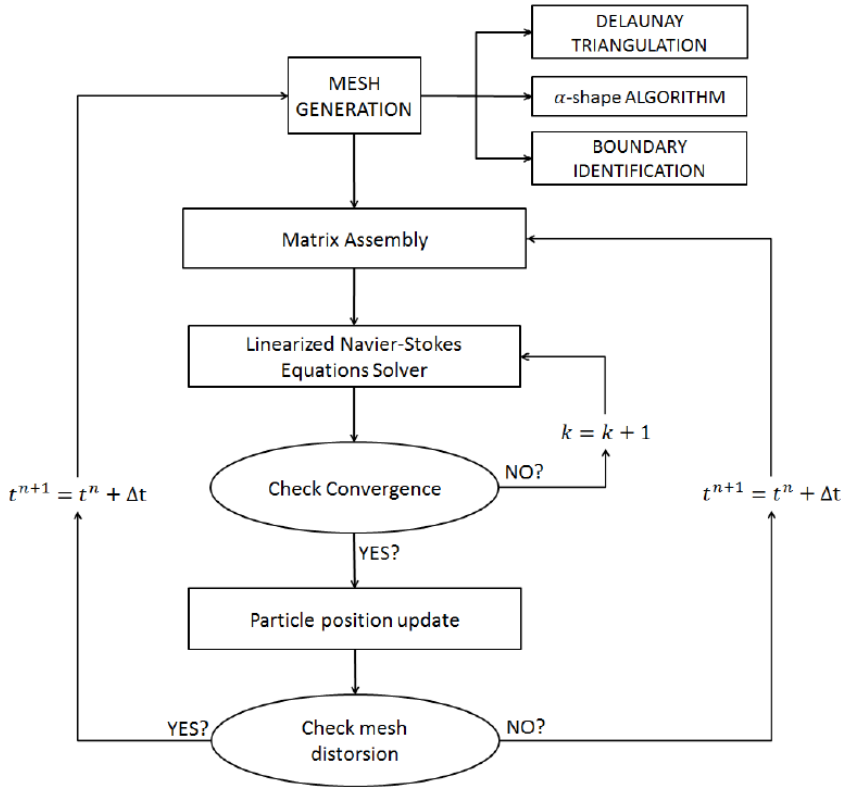

Figure 4.9: Flowchart of the colution scheme

4.6.6 Structure of the computational code

The general structure of the numerical code is summarized in Table 4.1. The routine **main** is used to call the subroutine **fluid_sol**, which reads the input (node coordinates, boundary conditions, numerical and computational parameters) The subroutine **fluid_sol** calls the subroutine **fluid_solution_dt** which is the core of the code, with the computational algorithm in the interval Δt.

The subroutine **tessellation** is used to perform the Delaunay triangulation if the distortion check has been activated. The Delaunay triangulation is carried out using the public domain tool *Tetgen* (Si, 2006). The generation of the convex hull domain, the α-method and the boundary identification are also performed in the subroutine **tessellation**. In the subroutine **matrix**, the system matrices are computed and assembled and the boundary conditions are applied for both velocities (no-slip boundaries) and pressures (free-surface boundaries). The matrices are stored using the Compressed Sparse Row method. The linear system is then solved in the **solver** routine with a monolithic or fractional step approach. In both cases, the *PARDISO* solver (Schenk et al., 2005, 2007; Kuzmin et al., 2013) is used to solve the linear system of equations. The motion of the particles that may have separated from the domain is computed in the subroutine **alone_particle**. The position of the mesh nodes is updated using the velocity of each node in **displacement_update** and the stress tensor of each element is computed in **fluid_stress**. The subroutine **add_remove** performs the addition and removal of particles (see section 4.6.4).

- **main**
- **fluid_sol**
  - **read_input**
  - **fluid_solution_dt**
    a. **tessellation**
    b. **matrix**
    c. **solver**
    d. **alone_particle**
    e. **displacement_update**
    f. **fluid_stress**
  - **output**
  - **add_remove**

Table 4.1: Graphic scheme of the implemented code

5

A Lagrangian method with slip boundary conditions on Eulerian nodes

In this chapter the slip boundary conditions for granular materials are presented and discussed, and a special mixed Eulerian-Lagrangian formulation is introduced for the elements on the basal interface to accommodate the new slip conditions into the numerical method.

5.1 Slip boundary conditions

No-slip boundary conditions are usually assumed in the solution of Navier-Stokes equations for fluid dynamics problems. However, wall slip is known to occur in many industrial processes, such as in polymer extrusion (Denn, 2001), ..., and the definition of appropriate slip boundary condition is still the object of discussion (Schowalter, 1988).

In the case of granular flows, the slip velocity between the flowing mass and

the basal surface has been observed to increase with the average grain diameter in Schaefer et al., 2010, where the velocity profiles in granular landslides have been experimentally studied. As a consequence of the frictional relative slip, a new basal dissipation mechanism need to be characterized in addition to the viscous dissipation inside the material bulk. This is usually done introducing a basal friction coefficient, which however is not easy to identify for real landslides. A recent and comprehensive study (Lucas et al., 2014) has shown that the effective friction coefficient is not a constant property of the interface, but decreases with the slip velocity and with the total mass of the moving landslide. This frictional weakening can possibly be produced by micro-mechanical processes such as flash-heating, whereby frictional heating is produced at the micro-contact scale. For high slip velocities, heat dissipation is prevented and thermal weakening effects like melting or other phase transformations and phenomena, are activated (Habib, 1976; Voight and Faust, 1982; Vardoulakis, 2002; Cecinato et al., 2011).

The consideration of slip boundary conditions together with Navier-Stokes equation is not standard. The classical no-slip boundary condition in fluid dynamics is microscopically acceptable in most cases and it is based on physical and mathematical considerations at the microscale (Richardson, 1973), but it is not physically acceptable in several types of liquid flow at solid surface (Thompson and Troian, 1997) and, as already mentioned, for increasing diameter granular flows (Schaefer et al., 2010). The simplest, classical alternative to the no-slip boundary conditions are the so-called Navier boundary conditions, that establish a linear dependence, through a material friction-like parameter, of the basal tangential stress on the slip velocity. In practice, one can imagine a variety of different conditions, passing from maximum tangential stress and no-slip, to zero tangential stress and free slip in tangential direction.

A convenient geometrical parameter to describe this variety of condition is the slip length (Thompson and Robbins, 1990). The meaning of the slip length is shown in figure 5.1, where a Couette flow between two rigid walls at a distance h is shown. The upper wall is moving with assigned horizontal velocity U, while

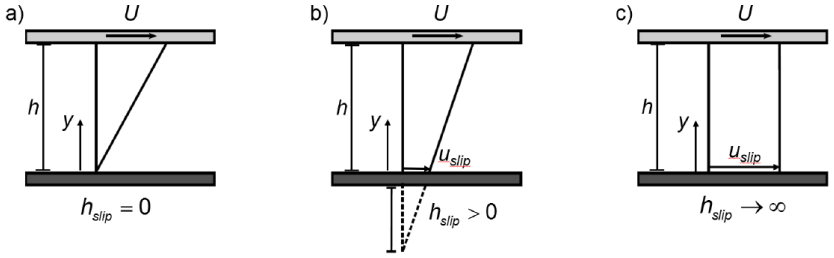

Figure 5.1: Example of slip boundary condition for a Couette flow. The top plate (light gray) moves with a prescribed velocity, while the bottom one (dark gray) has a slip boundary condition imposed. Pictures represent the velocity profiles.

the lower wall is fixed. The case of perfect no-slip condition is shown in figure 5.1a. In figure 5.1b, a certain amount of slip is present, with a non-zero fluid tangential velocity u_{slip} at the lower plate interface ($y = 0$). The slip length h_{slip} is defined as the distance from the lower plate to the point at zero velocity obtained extrapolating the velocity profile. Figure figure 5.1c shows the limit case of free slip, where an infinite slip length is obtained. Negative slip lengths can also occur in some cases (Thompson and Robbins, 1990) when the lower fluid layers are locked to the plate and the no-slip condition extends to some layers inside the fluid channel. The slip length can be considered to be a property of the fluid-wall interface.

In practical cases, the slip often occurs only when a critical value of the tangential stress is reached, in analogy with the classical Bingham model. In this cases the Navier boundary condition can be modified by adding a constant threshold to the linear function of the slip velocity. However, from the mathematical point of view, this implies a significant complication since the weak form of the balance equations has to be formulated as a variational inequality (Fortin et al., 1991). To avoid this difficulties, a regularization similar to the one usually adopted for the Bingham flows (Papanastasiou, 1987; Pitman et al., 2003) is here adopted.

Defining by $\mathbf{n}$ the unit normal to the basal interface and $\mathbf{u}$ the velocity at

a point, the imposition of the slip boundary condition requires that also the no-flux condition $\mathbf{u} \cdot \mathbf{n} = \mathbf{0}$ is enforced. These conditions are known to lead to the so called Babuska's paradox (Verfürth, 1987), with non-convergent approximations in the presence of curved boundaries, where polygonal finite element discretizations are used. A difficulty connected with the type of boundary conditions, especially in combination with the incompressibility constraint, is the non unique definition of the normal vector a boundary nodes with piecewise linear discretization, see Engelman et al., 1982, for a technique for the computation of a unique normal, based on mass conservation and see also Behr, 2004 for a discussion. Other difficulty is the particular way in which the evolving boundary conditions are treated in the PFEM with continuous remeshing. To alleviate these problems, in this work the no-flux condition is enforced through a penalization technique, following Dione et al., 2013; Dione and Urquiza, 2015, together with a reduced integration of the penalty integral term.

5.2 ALE framework

The classical Lagrangian and Eulerian descriptions of motion have been described in chapter 3. The Arbitrary Lagrangian-Eulerian description (ALE) has been developed in order to combine the best features of both the Lagrangian and the Eulerian approaches. In the ALE description of motion, the reference coordinates $\boldsymbol{\Upsilon}$ not necessary coincides with the material $\mathbf{X}$ or spatial coordinates $\mathbf{x}$. In the reference configuration R_Υ the reference coordinates $\boldsymbol{\Upsilon}$, are introduced to identify the grid points. In fact, the mapping κ from the reference domain to the spatial domain can be understood as the motion of the grid points in the spatial domain (Donea and Huerta, 2003). With this considerations the mesh velocity is defined as

$$\mathbf{r}(\Upsilon, t) = \left.\frac{\partial \mathbf{x}}{\partial t}\right|_\Upsilon \tag{5.1}$$

In figure 5.2 the transformation $\chi(\mathbf{X}, t)$ can be seen has a composition of the

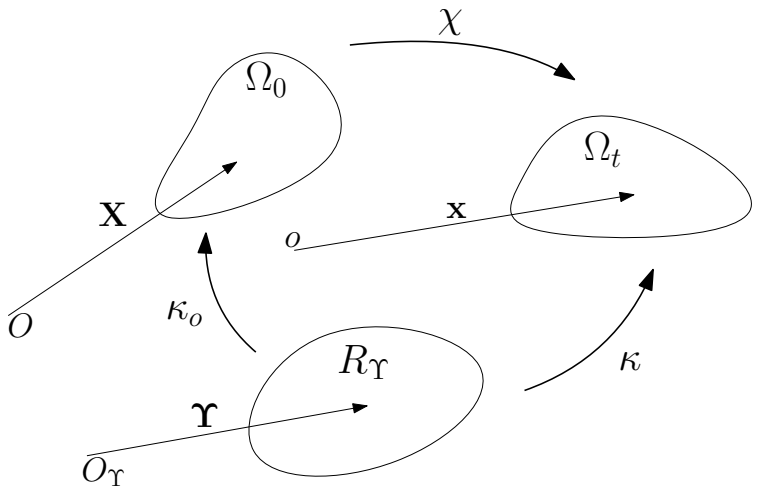

Figure 5.2: The body B depicted in the configurations Ω_0 and Ω_t. R_Υ represent the referential configuration in the ALE description. The motion of the ALE computational mesh is independent from the material motion

two transformations $\kappa(\mathbf{X}, t)$ and $\kappa_0^{-1}(\mathbf{X}, t)$ as follow

$$\mathbf{x} = \chi(\mathbf{X}, t) = \kappa[\kappa_0^{-1}(\mathbf{X}, t)] \tag{5.2}$$

Differentiating the previous relation it is possible to find a relation between the mesh and the particle velocity (Donea and Huerta, 2003)

$$\mathbf{u} = \mathbf{r} + \frac{\partial \mathbf{x}}{\partial \boldsymbol{\Upsilon}} \cdot \frac{\partial \boldsymbol{\Upsilon}}{\partial t}\Big|_X \tag{5.3}$$

The equation may be rewritten as

$$\mathbf{c} = \mathbf{u} - \mathbf{r} = \frac{\partial \mathbf{x}}{\partial \boldsymbol{\Upsilon}} \cdot \frac{\partial \boldsymbol{\Upsilon}}{\partial t}\Big|_X \tag{5.4}$$

where $\mathbf{c}$ is the convective velocity which represents the relative velocity between the material and the mesh. Consider now two special cases in the ALE formulation, the first one when $\kappa = \chi$ and $\kappa_0 = \mathbf{I}$ and the second one when $\kappa = \mathbf{I}$ and $\kappa_0 = \chi^{-1}$. In the first case $\boldsymbol{\Upsilon} = \mathbf{X}$ and the Lagrangian framework is recovered while in the second one $\boldsymbol{\Upsilon} = \mathbf{x}$, which corresponds to the Eulerian framework. In

equation (5.4) if $\boldsymbol{\Upsilon} = \mathbf{X}$ the term $\frac{\partial \Upsilon}{\partial t}|_X = 0$ and so the convective velocity is zero. Otherwise if $\Upsilon = \mathbf{x}$, the convective velocity $\mathbf{c}$ is equal to the particle velocity $\mathbf{u}$, in fact the term $\frac{\partial \mathbf{x}}{\partial \Upsilon} = 1$.

The Navier-Stokes equations in the ALE formulation is written as

$$\rho\left(\frac{\partial \mathbf{u}}{\partial t}\Big|_{\Upsilon} + (\mathbf{c}\cdot\nabla_x)\mathbf{u}\right) = \nabla_x\cdot\sigma + \rho\mathbf{b} \qquad in \quad \Omega_t\times(0,T) \tag{5.5}$$

$$\nabla_x\cdot\mathbf{u} = 0 \qquad in \quad \Omega_t\times(0,T) \tag{5.6}$$

In this work, the equations (5.5)-(5.6) are solved in a Lagrangian framework in all the domain except on the part of boundary where slip conditions are imposed.

Equations (5.5),(5.6) need be supplemented with proper initial and boundary conditions.

5.3 Navier type boundary conditions

The boundary $\partial\Omega_t$ is now partitioned into three non-overlapping subsets $\partial\Omega_t = \Gamma_t^D \cup \Gamma_t^N \cup \Gamma_t^S$. On Γ_t^D and Γ_t^N standard Dirichlet and Neumann boundary conditions are imposed

$$\begin{aligned} \mathbf{u}(\mathbf{x},t) &= \bar{\mathbf{u}}(\mathbf{x},t) \qquad \text{on}\,\Gamma_t^D \\ \boldsymbol{\sigma}(\mathbf{x},t)\cdot\mathbf{n} &= \mathbf{h}(\mathbf{x},t) \qquad \text{on}\,\Gamma_t^N \end{aligned} \tag{5.7}$$

where $\bar{\mathbf{u}}(\mathbf{x},t)$ and $\mathbf{h}(\mathbf{x},t)$ are assigned functions and $\mathbf{n}$ is the outward normal to the boundary, while on Γ_t^S slip boundary conditions are considered.

Let $\mathbf{u}_{slip}$ be the relative velocity between the moving soil and the basal surface Γ_t^S and $\mathbf{t}$ the tangential traction acting on the landslide material along the same surface (Figure 5.3):

$$\mathbf{u}_{slip} = (\mathbf{I} - \mathbf{n}\otimes\mathbf{n})\,\mathbf{u}, \quad \mathbf{t} = (\mathbf{I} - \mathbf{n}\otimes\mathbf{n})\,[(\boldsymbol{\sigma}_D - p\mathbf{I})\,\mathbf{n}] \tag{5.8}$$

Navier type boundary conditions are assumed along Γ_t^S:

$$\mathbf{u}_{slip} = -\beta\mathbf{t} \tag{5.9}$$

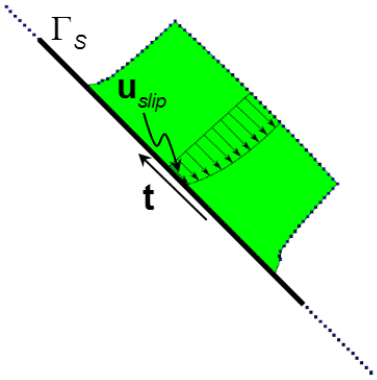

Figure 5.3: Slip velocity profile and basal tangential traction.

where

$$\beta = h_{slip}/\tilde{\mu}_{basal} \tag{5.10}$$

is a parameter, having the dimension of a length over a viscosity, characterizing the basal interface, h_{slip} is the slip length for an ideal Couette flow and $\tilde{\mu}_{basal}$ is the apparent viscosity at the interface defined as:

$$\tilde{\mu}_{basal} = \frac{2}{3}\left[\mu + \frac{p\tan\varphi_{basal}}{\dot{\gamma}}\left(1 - e^{-N\dot{\gamma}}\right)\right] \tag{5.11}$$

Indeed the interface is characterized by two parameters, h_{slip} (or β) and φ_{basal}.

With these definitions, the complete set of boundary conditions consists of (5.7) on Γ_t^D and Γ_t^N, supplemented by the conditions on Γ_t^S, that include the no-flux condition through the basal interface:

$$\left.\begin{array}{l} \mathbf{t} = -\frac{1}{\beta}\mathbf{u}_{slip} \\ \mathbf{u}\cdot\mathbf{n} = 0 \end{array}\right\} \quad \text{on} \quad \Gamma_t^S \tag{5.12}$$

5.4 Navier type boundary conditions with pressure dependent velocity

Considering now a pressure dependent threshold, the Navier type boundary conditions along Γ_t^S become:

$$\mathbf{u}_{slip} = -\beta \frac{\mathbf{t}}{\|\mathbf{t}\|} \langle \|\mathbf{t}\| - p \tan \varphi_{basal} \rangle \tag{5.13}$$

where β is a parameter defined in equation (5.10). Condition (5.13) states that the slip is resisted by a tangential force proportional to the slip velocity. For $\beta = 0$, the no-slip boundary condition is recovered, while $\beta \to \infty$ represents the stress free boundary condition. According to (5.13), slippage occurs only when the pressure dependent threshold value $p \tan \varphi_{basal}$ is exceeded by the tangential traction $\mathbf{t}$.

From (5.13) one has

$$\beta \langle \|\mathbf{t}\| - p \tan \varphi_{basal} \rangle = \|\mathbf{u}_{slip}\| \tag{5.14}$$

and solving for $\|\mathbf{t}\|$

$$\|\mathbf{t}\| = \frac{1}{\beta} \|\mathbf{u}_{slip}\| + p \tan \varphi_{basal} \quad \text{for} \quad \|\mathbf{t}\| - p \tan \varphi_{basal} > 0 \tag{5.15}$$

Replacing the expression (5.14) in (5.13) and solving for $\mathbf{t}$ one has

$$\mathbf{t} = -\frac{\|\mathbf{t}\|}{\|\mathbf{u}_{slip}\|} \mathbf{u}_{slip} \quad \text{for} \quad \|\mathbf{t}\| - p \tan \varphi_{basal} > 0 \tag{5.16}$$

Finally, replacing the expression (5.15) of $\|\mathbf{t}\|$ one obtains (see e.g. Fortin et al. (1991))

$$\mathbf{t} = -\left(\frac{1}{\beta} + \frac{p \tan \varphi_{basal}}{\|\mathbf{u}_{slip}\|} \right) \mathbf{u}_{slip} \quad \text{for} \quad \|\mathbf{t}\| - p \tan \varphi_{basal} > 0 \tag{5.17}$$

The expression in (5.17) is formally similar to the expression in (3.68) and it can be regularized using the same technique:

$$\mathbf{t} = -\frac{1}{\tilde{\beta}} \mathbf{u}_{slip}, \quad \frac{1}{\tilde{\beta}} = \frac{1}{\beta} + \frac{p \tan \varphi_{basal}}{\|\mathbf{u}_{slip}\|} \left(1 - e^{-N \|\mathbf{u}_{slip}\|} \right) \tag{5.18}$$

The simple expression in $(5.18)_1$, which is equivalent to adopting a non-linear Navier type boundary condition with stress dependent slip length, has been used to model the relation between the slip velocity and the tangential traction acting along the basal interface.

With these definitions, the complete set of boundary conditions consists of (5.7) on Γ_t^D and Γ_t^N, supplemented by the conditions on Γ_t^S, that include the no-flux condition through the basal interface:

$$\left.\begin{array}{l} \mathbf{t} = -\frac{1}{\tilde{\beta}}\mathbf{u}_{slip} \\ \mathbf{u}\cdot\mathbf{n} = 0 \end{array}\right\} \quad \text{on} \quad \Gamma_t^S \tag{5.19}$$

5.5 Variational form of the balance equations

Without loss of generality, in the following $\mathbf{h}(\mathbf{x},t) = 0$ and $\bar{\mathbf{u}}(\mathbf{x},t) = 0$ will be assumed on Γ_t^N and Γ_t^D, respectively. The weak form of the balance equations (5.5)-(5.6), with the boundary conditions (5.7) and (5.19) is obtained following a standard Galerkin approach:

$$\begin{aligned} &\int_{\Omega_t} \rho\left[\left.\frac{\partial \mathbf{u}}{\partial t}\right|_{\Upsilon} + (\mathbf{c}\cdot\nabla_x)\mathbf{u}\right]\cdot\mathbf{w}\, d\Omega_t - \int_{\Omega_t}(\nabla_x\cdot\boldsymbol{\sigma}+\rho\mathbf{b})\cdot\mathbf{w}\, d\Omega_t + \int_{\Gamma^N}(\boldsymbol{\sigma}\mathbf{n})\cdot\mathbf{w}d\Gamma + \\ &\qquad + \int_{\Gamma^S}\left(\mathbf{t}+\frac{1}{\tilde{\beta}}\mathbf{u}_{slip}\right)\cdot\mathbf{w}d\Gamma = 0 \\ &\int_{\Omega_t}(\nabla_x\cdot\mathbf{u})\, q\, d\Omega_t = 0 \end{aligned} \tag{5.20}$$

where $\mathbf{w}$ and q are respectively vector and scalar test functions, with $\mathbf{w} = \mathbf{0}$ on Γ^D, $\mathbf{w}\cdot\mathbf{n} = 0$ on Γ^S, $q = 0$ on Γ^N. Integrating by parts the second integral in $(5.20)_1$, the usual variational form is recovered

$$\begin{aligned} &\int_{\Omega_t} \rho\left[\left.\frac{\partial \mathbf{u}}{\partial t}\right|_{\Upsilon} + (\mathbf{c}\cdot\nabla_x)\mathbf{u}\right]\cdot\mathbf{w}\, d\Omega_t + \int_{\Omega_t}\boldsymbol{\sigma}_D : \nabla_x\mathbf{w}\, d\Omega_t - \int_{\Omega_t} p(\nabla_x\cdot\mathbf{w})\, d\Omega_t - \\ &\qquad \int_{\Omega_t}\rho\mathbf{b}\cdot\mathbf{v}\, d\Omega_t + \int_{\Gamma^S}\left(-\boldsymbol{\sigma}\mathbf{n}+\mathbf{t}+\frac{1}{\tilde{\beta}}\mathbf{u}_{slip}\right)\cdot\mathbf{w}d\Gamma = 0 \\ &\int_{\Omega_t}(\nabla_x\cdot\mathbf{u})\, q\, d\Omega_t = 0 \end{aligned} \tag{5.21}$$

Noting that

$$\int_{\Gamma^S} (-\boldsymbol{\sigma}\mathbf{n} + \mathbf{t}) \cdot \mathbf{w} d\Gamma = -\int_{\Gamma^S} \mathbf{w} \cdot (\mathbf{n} \otimes \mathbf{n}) (\boldsymbol{\sigma}\mathbf{n}) \, d\Gamma = -\int_{\Gamma^S} (\mathbf{w} \cdot \mathbf{n}) \mathbf{n} \cdot \boldsymbol{\sigma}\mathbf{n} d\Gamma = 0 \tag{5.22}$$

the variational form of the balance equations is finally written as

$$\begin{aligned} \int_{\Omega_t} \rho \left[\frac{\partial \mathbf{u}}{\partial t}\Big|_{\Upsilon} + (\mathbf{c} \cdot \nabla_x)\mathbf{u} \right] \cdot \mathbf{w} \, d\Omega_t + \int_{\Omega_t} \boldsymbol{\sigma}_D : \nabla_x \mathbf{w} \, d\Omega_t - \int_{\Omega_t} p(\nabla_x \cdot \mathbf{w}) \, d\Omega_t - \\ \int_{\Omega_t} \rho \mathbf{b} \cdot \mathbf{w} \, d\Omega_t + \int_{\Gamma^S} \left(\frac{1}{\tilde{\beta}} \mathbf{u}_{slip} \right) \cdot \mathbf{w} d\Gamma = 0 \\ \int_{\Omega_t} (\nabla_x \cdot \mathbf{u}) \, q \, d\Omega_t = 0 \end{aligned} \tag{5.23}$$

As noted by several authors (see e.g. Verfürth (1987); Engelman et al. (1982); Behr (2004)), the enforcement of the no-flux condition $(5.19)_2$ in the presence of curved boundaries may lead to numerical inconsistencies. For this reason, the no-flux condition is here replaced by a penalized form, in the line of what proposed in Dione et al. (2013), together with a reduced integration of the penalty integral term. Let us set

$$\mathbf{n} \cdot \boldsymbol{\sigma}\mathbf{n} = -\frac{1}{\epsilon} \mathbf{u} \cdot \mathbf{n} \tag{5.24}$$

on Γ^S, ϵ being a small number. With this definition, the last integral in $(5.20)_1$ becomes

$$\int_{\Gamma^S} \left[\left(\mathbf{t} + \frac{1}{\tilde{\beta}} \mathbf{u}_{slip} \right) + \left(\mathbf{n} \cdot \boldsymbol{\sigma}\mathbf{n} + \frac{1}{\epsilon} \mathbf{u} \cdot \mathbf{n} \right) \mathbf{n} \right] \cdot \mathbf{w} d\Gamma \tag{5.25}$$

where now $\mathbf{w}$ is not required anymore to satisfy $\mathbf{w} \cdot \mathbf{n} = \mathbf{0}$ on Γ^S. After integration by parts and taking into account that $\mathbf{t} + (\mathbf{n} \cdot \boldsymbol{\sigma}\mathbf{n})\mathbf{n} = \boldsymbol{\sigma}\mathbf{n}$, the last integral in $(5.21)_1$ transforms into

$$\begin{aligned} \int_{\Gamma^S} \left[-\boldsymbol{\sigma}\mathbf{n} + \left(\mathbf{t} + \frac{1}{\tilde{\beta}} \mathbf{u}_{slip} \right) + \left(\mathbf{n} \cdot \boldsymbol{\sigma}\mathbf{n} + \frac{1}{\epsilon} \mathbf{u} \cdot \mathbf{n} \right) \mathbf{n} \right] \cdot \mathbf{w} d\Gamma = \\ = \int_{\Gamma^S} \left[\frac{1}{\tilde{\beta}} \mathbf{u}_{slip} + \frac{1}{\epsilon} (\mathbf{u} \cdot \mathbf{n}) \mathbf{n} \right] \cdot \mathbf{w} d\Gamma \end{aligned} \tag{5.26}$$

5.6 Space discretization

The weak form (5.21), with the modified conditions (5.26) on the slip boundary Γ^S, is discretized for implementation in the Particle Finite Element Method (PFEM), described in Chapter 4.

A key point in the PFEM is the algorithm for boundary identification and for contact detection (see section 4.6.2). In the case of landslides runout, the computational domain consists of the initial volume occupied by the soil mass plus the whole surface of the slope on which the landslide can possibly slide during its runout. In the spirit of the method, nodes are placed on the whole sliding surface, so that finite elements can be generated automatically by the remeshing procedure whenever the soil mass is approaching that part of the boundary. These nodes are not active, and therefore are not identified as material particles (i.e. they do not possess any degree of freedom), until they become the vertex of a finite element of sufficiently regular shape (i.e. that is not removed by the alpha-shape method). In figure 5.4, two different instants ($t = 30$ and 31 s) are considered in the Frank rock avalanche simulation which will be discussed in detail in chapter 7. Among the slip nodes of figure 5.4(c), blue nodes are not active at $t = 30$ and 31 s, green nodes are active at both instants, red nodes are active only at $t = 30$ s and yellow ones only at $t = 31$ s.

Slip boundary conditions are difficult to enforce in this fully Lagrangian framework, in which nodes on the basal surface have to move according to the soil velocity, but at the same time have to define the position of the boundary. If slip nodes are moved following their velocity, the definition of the boundary is lost and the boundary tracking algorithm cannot work anymore. To overcome this difficulty, all nodes in the mesh are treated as Lagrangian (i.e. $\boldsymbol{\Upsilon} = \mathbf{X}$ in (5.5)-(5.6)) except those on Γ^S (where slip conditions are imposed), which are treated as Eulerian (i.e. $\boldsymbol{\Upsilon} = \mathbf{x}$) and therefore remain fixed in their initial position. This special treatment gives rise to a mixed Lagrangian-Eulerian formulation, whereby some nodes are Lagrangian and some others (more specifically those on Γ^S) are

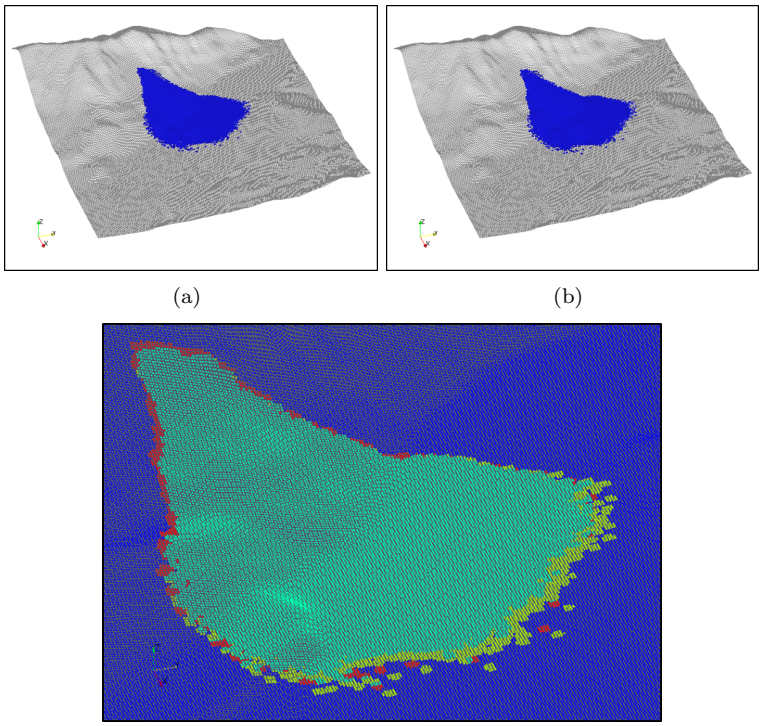

(a) (b)

(c)

Figure 5.4: Simulation of the Frank Rock avalanche at 30 s (a) and 31 s (b); (c) slip boundary nodes: in yellow the nodes which belongs to the set of elements (b) but not to (a) and in red the nodes which belongs to the set of elements (a) but not to (b).

Eulerian. In particular, elements having a node on the boundary Γ^S will have degrees of freedom of mixed nature (Figure 5.5).

Proceeding now with a standard finite element discretization with linear interpolation functions for both pressure and velocity, the following semidiscretized form is obtained:

$$\begin{aligned} \mathbf{M}\dot{\mathbf{V}} + (\mathbf{K} + \mathbf{K}_{slip} + \mathbf{K}_c)\mathbf{V} + \mathbf{D}^T\mathbf{P} &= \mathbf{B} \\ \mathbf{D}\mathbf{V} &= \mathbf{0} \end{aligned} \tag{5.27}$$

where in equations (4.20) to (4.23) a detailed Lagrangian definition of $\mathbf{M}$, $\mathbf{K}$,

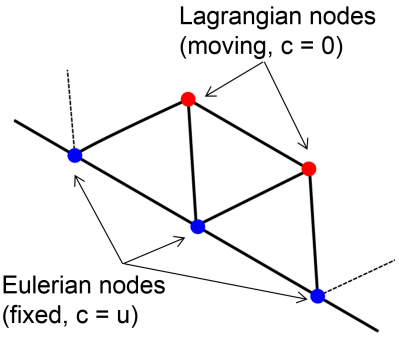

Figure 5.5: Schematic illustration of the distinction between Lagrangian and Eulerian nodes.

D and **B** has been provided. **V** and **P**, as usual, contain the nodal values of velocity and pressure respectively, **M** is the mass matrix, **K** is the matrix of viscoplastic coefficients, having the same structure of the deviatoric part of the stiffness matrix, **D** is the discretization of the divergence operator, **B** is the vector of body forces and boundary tractions, $\mathbf{K}_c$ is the discretization of the convective term on the slip boundary and $\mathbf{K}_{slip}$ is the discretization of the integral in (5.26). Their definition is given below.

Let n_{dim} define the problem dimension ($n_{dim} = 2$ in 2D, $n_{dim} = 3$ in 3D) and let n_{node} be the number of nodes per element ($n_{node} = 3$ for triangular elements, $n_{node} = 4$ for tetrahedra). Defining with Ω_t^S the subdomain of Ω_t containing elements with at least one node on Γ^S and setting $\mathbf{c}^e(\mathbf{x}) = \mathbf{N}^e(\mathbf{x})\mathbf{C}^e$, $\mathbf{C}^e$ being nodal values of the velocity $\mathbf{c}(\mathbf{x})$ on element Ω^e, the components of matrix $\mathbf{K}_c^e$ are obtained as:

$$[\mathbf{K}_c^e]_{a_h b_m} = \int_{\mathbf{\Omega}^e \in \Omega^S} N_{a,j}^e C_{dj}^e N_d^e N_b^e \delta_{hm} \, d\Omega^e \tag{5.28}$$

where $a, b, d = 1, \ldots n_{node}$, $i, j, h, m = 1 \ldots n_{dim}$, δ_{hm} is the Kronecker delta, N_a is the shape function of node a, $N_{a,j} = \partial N_a / \partial \mathbf{x}_j$, and summation on repeated indexes d and j is assumed. In (5.28), $[\mathbf{K}_c^e]_{a_h b_m}$ denotes the hm component of

the submatrix (of dimensions $n_{dim} \times n_{dim}$) $[\mathbf{K}^e_c]_{ab}$, C^e_{dj} is the j-th component of $\mathbf{c}$ at node d, with $C^e_{dj} = 0$ if d is an interior node (Lagrangian node in Figure 5.5) and $C^e_{dj} = V^e_{dj}$ if d is a node on Γ^S (Eulerian node in Figure 5.5).

$\mathbf{K}_{slip}$ for element e is defined as:

$$\mathbf{K}^e_{slip} = \int_{\Gamma^S_e} \mathbf{Q}^{e\,T} \mathbf{N}^{e\,T} \begin{bmatrix} \frac{1}{\epsilon} & 0 & 0 \\ 0 & \frac{1}{\beta} & 0 \\ 0 & 0 & \frac{1}{\beta} \end{bmatrix} \mathbf{N}^e \mathbf{Q}^e d\Gamma \tag{5.29}$$

where $\mathbf{N}^e$ is the matrix gathering the shape functions of element e and $\mathbf{Q}^e = \text{diag}[\mathbf{Q}^e_a]$, $a = 1, \ldots n_{node}$, is a block diagonal matrix. For a denoting a node on Γ^S, $\mathbf{Q}^e_a$ is the orthogonal matrix transforming the velocity components u_x, u_y, u_z with respect to the global reference system into the components u_n, u_{t_1}, u_{t_2}, locally normal and tangent to the basal surface at each element node a on Γ^S:

$$\begin{bmatrix} u_n \\ u_{t_1} \\ u_{t_2} \end{bmatrix}_a = \mathbf{Q}_a \begin{bmatrix} u_x \\ u_y \\ u_z \end{bmatrix}_a \tag{5.30}$$

In contrast, for a denoting an interior node, one has $\mathbf{Q}^e_a = \mathbf{0}$.

All matrices $\mathbf{K}^e_c$ and $\mathbf{K}^e_{slip}$ not pertaining to elements with nodes on Γ^S are zero.

5.7 Time integration and solution scheme

Considering the time interval $(0, T)$ divided in a fixed number of time step ΔT and assuming that the state of the system is known at $t = t^n$ in terms of the positions $\mathbf{x}^n = \mathbf{x}(t^n)$, velocities $\mathbf{V}^n = \mathbf{V}(t^n)$ and pressures $\mathbf{P}^n = \mathbf{P}(t^n)$, the state at time $t = t^{n+1}$ is determined enforcing equations (5.27) at $t = t^{n+1}$ using a backward Euler integration scheme (see section 4.2). The final fully discretized nonlinear problem writes:

$$\mathbf{M}\frac{\mathbf{V}^{n+1} - \mathbf{V}^n}{\Delta t} + (\mathbf{K} + \mathbf{K}_{slip} + \mathbf{K}_c)\mathbf{V}^{n+1} + \mathbf{D}^T\mathbf{P}^{n+1} = \mathbf{B} \tag{5.31}$$

$$\mathbf{D}\mathbf{V}^{n+1} = \mathbf{0} \tag{5.32}$$

It is important to recall that all the matrix and vector operators generally depend non-linearly on the unknown configuration $\mathbf{x}^{n+1}$. Using linear shape functions for both velocity and pressure, stabilization terms should be added to equation (5.31)-(5.32) (see section 4.4).

System (5.31)-(5.32) can be solved directly with a monolithic approach, recalling that a stabilization is necessary (see section 4.4). Alternately, a fractional step-like schemes can be derived from the discretized equation (5.31)-(5.32) (see section 4.3), leading to the system of equations:

$$\frac{1}{\Delta t}\mathbf{M}(\tilde{\mathbf{V}}^{n+1} - \mathbf{V}^{n}) + (\mathbf{K} + \mathbf{K}_{slip} + \mathbf{K}_{c})\tilde{\mathbf{V}}^{n+1} = \mathbf{B}^{n+1} \tag{5.33}$$

$$\Delta t \mathbf{L}\mathbf{P}^{n+1} = \mathbf{D}\tilde{\mathbf{V}}^{n+1} \tag{5.34}$$

$$\frac{1}{\Delta t}\mathbf{M}(\mathbf{V}^{n+1} - \tilde{\mathbf{V}}^{n+1}) + \mathbf{D}^{T}\mathbf{P}^{n+1} = \mathbf{0} \tag{5.35}$$

In equation (5.28) the non linear convective term is linearised considering the vector velocity $\mathbf{C}^{e}$ at the iteration k, computed considering the nodal velocity at iteration $k-1$:

$$[\mathbf{K}_{c}^{e}]_{a_h b_k}^{n+1,k} = \int_{\mathbf{\Omega}^{e} \in \Omega^{S}} N_{a,j}^{e} C_{dj}^{e^{n+1,k-1}} N_{d}^{e} N_{b}^{e} \delta_{hk} \, d\Omega^{e} \tag{5.36}$$

Similarly, the viscous term is linearised as follow:

$$\tilde{\mu}^{n+1,k} = \frac{2}{3}\left[\mu + \frac{p^{n+1,k-1}\tan\varphi}{\dot{\gamma}^{n+1,k-1}}\left(1 - e^{-N\dot{\gamma}^{n+1,k-1}}\right)\right] \tag{5.37}$$

where

$$\dot{\gamma}^{n+1,k-1} = \frac{f}{\mu} = \frac{< q^{n+1,k-1} - p^{n+1,k-1}\tan\varphi >}{\mu} \tag{5.38}$$

The last necessary linearisation takes into account the non linear slip boundary condition with pressure dependent threshold. In particular the definition of the parameter $\tilde{\beta}$ which appears in equation$(5.18)_2$ is linearised as follow:

$$\frac{1}{\tilde{\beta}^{n+1,k}} = \frac{1}{\beta^{n+1,k}} + \frac{p^{n+1,k-1}\tan\varphi_{basal}}{\|\mathbf{u}_{slip}^{n+1,k-1}\|}\left(1 - e^{-N\|\mathbf{u}_{slip}^{n+1,k-1}\|}\right) \tag{5.39}$$

5.8 Couette flow

The analytical solutions for Couette and Poiseuille flows with linear and non-linear Navier slip laws have been presented in Ferrás et al., 2012. To validate the implementation of the slip boundary conditions, a simple test is considered, consisting in a Couette flow of water ($\rho = 10^{-3}$ kg/m^3, $\mu = 10^{-3}$ Pa s, $\varphi = \varphi_{basal} = 0$) between two parallel plates at distance h, where the top plate moves with a fixed velocity U, while at the bottom the Navier slip condition is imposed (Figure 5.1). The analytical solution consists of a linear velocity profile along the channel height:

$$u(y) = \frac{U(y-h)}{h + h_{slip}} + U \tag{5.40}$$

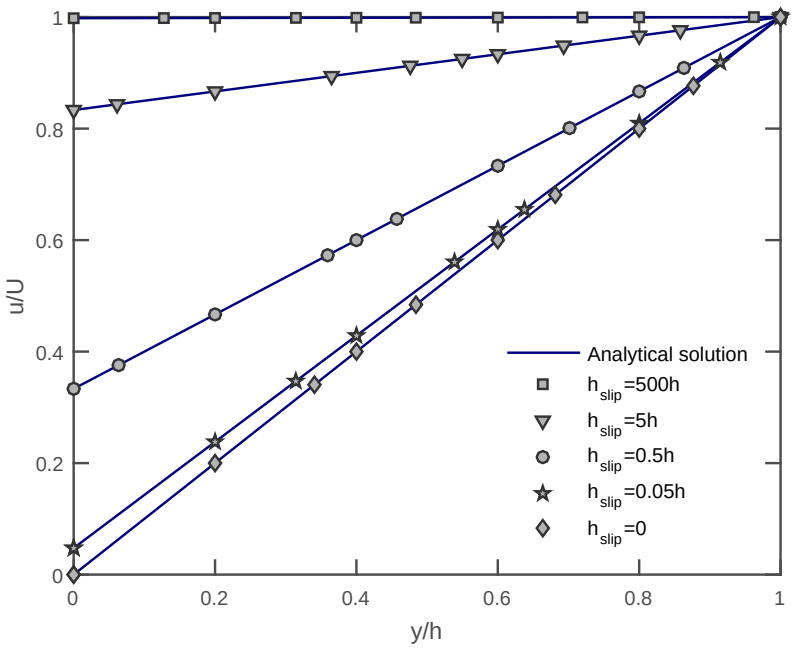

Figure 5.6: Couette flow. Comparisons between analytical and numerical solution.

Figure 5.6 shows a comparison between the analytical and the numerical solutions, the latter obtained using the formulation discussed in this section ,varying the slip parameter h_{slip}. A perfect match with the expected solutions is obtained.

5.9 PFEM with nodal integration

Another subject considered in this work, is the implementation of a nodally integrated formulation instead of the standard elementally integrated formulation. An advantage of the Lagrangian approach is that the convective terms in the momentum conservation disappear, and the difficulty is transmitted to the necessity to frequently retriangulate the mesh. When retriangulation is performed, data have to be transferred from the old mesh to the new one. In this approach, to avoid interpolation from mesh to mesh, only degrees of freedom of particles located at the vertices of triangles, in 2D, and tetrahedra, in 3D, are used, so that only linear shape functions can be used for both velocity and pressure. Nevertheless, some quantities like strains, stresses and densities have to be evaluated in the elements to perform the integration. This can lead to some difficulties if more than one material is considered (e.g. terrain and water) or if a nonlinear material with internal variables is to be used. To avoid this obstacle a 2D approach based on nodal integration has been developed. Considering a nodal integration, all the previous quantities can be computed for each node and can be stored in the node when a new triangulation is performed. Another advantage can be obtained if more complex plastic laws are adopted, since history variables can be defined in the nodes. Only few tests have been performed using the nodal integration described in this section, nevertheless primary results show a good agreement compared with the standard elemental formulation. A more detailed study is needed for a rigid visocplastic material.

In the balance equations (4.7)

$$\int_{\Omega_t} \rho \frac{\partial \mathbf{u}}{\partial t}\bigg|_X \cdot \mathbf{w} d\Omega_t = -\int_{\Omega_t} \mu \nabla_x \mathbf{u} : \nabla_x \mathbf{w} d\Omega_t + \int_{\Omega_t} p(\nabla_x \cdot \mathbf{w}) d\Omega_t + \int_{\Omega_t} \rho \mathbf{b} \cdot \mathbf{w} d\Omega_t + \int_{\Gamma_t^N} \mathbf{w} \cdot \mathbf{h} d\Gamma_t^N \qquad \forall \mathbf{w} \in S_0 \tag{5.41}$$

$$\int_{\Omega_t} (\nabla_x \cdot \mathbf{u}) q d\Omega_t = 0 \qquad \forall q \in Q \tag{5.42}$$

focusing on the term $\int_{\Omega_t} \mu \nabla_x \mathbf{u} : \nabla_x \mathbf{w} d\Omega_t$, in 2D, the two gradients can be written in matrix form, leading to

$$\int_{\Omega_t} \mu \nabla_x \mathbf{u} : \nabla_x \mathbf{w} d\Omega_t = \int_{\Omega_t} \mu \boldsymbol{\lambda}^T \boldsymbol{\eta} d\Omega_t \tag{5.43}$$

where

$$\boldsymbol{\eta} = \mathcal{G}\mathbf{u} \tag{5.44}$$

$$\boldsymbol{\lambda} = \mathcal{G}\mathbf{w} \tag{5.45}$$

$$\mathcal{G} = \begin{bmatrix} \frac{\partial}{\partial x} & 0 & \frac{\partial}{\partial y} \\ 0 & \frac{\partial}{\partial y} & \frac{\partial}{\partial x} \end{bmatrix}^T$$

The finite element discretization is assumed

$$w_i(\mathbf{X}, t) = \sum_J N_J(\mathbf{X}) \theta_{Ji}(t) \tag{5.46}$$

$$u_i(\mathbf{X}, t) = \sum_J N_J(\mathbf{X}) u_{Ji}(t) \tag{5.47}$$

where $J = 1, \ldots, N_{node}$ and N_{node} is the total number of the mesh nodes.

Following the idea of Krysl and Zhu, 2008; Castellazzi et al., 2015, inside each triangle the matrix form of the velocity gradient can be expressed as :

$$\boldsymbol{\eta} = \sum_J \mathbf{G}_J|_e \mathbf{u}_J \tag{5.48}$$

where $\boldsymbol{\eta}$ within element e is introduced, and $\mathbf{u}_J$ is the nodal velocity at node J. $\mathbf{G}_J|_e$ is the matrix of the shape function derivatives, which is constant inside each

triangle. Now the adopted velocity gradient matrix, is defined at each quadrature point (node) K, and has the form:

$$\bar{\boldsymbol{\eta}}|_K = \sum_J \overline{\mathbf{G}_J}|_K \mathbf{u}_J \tag{5.49}$$

where $\overline{\mathbf{G}_J}|_K$ is the assumed velocity gradient matrix of each node J connected to node K (K included). In this case $\bar{\boldsymbol{\eta}}|_K$ is defined in the integration point (node) K while in equation (5.48) it depends on the location. At this point the assumed velocity gradient is not known. For triangles, the nodal quadrature for a generic argument $(\bullet)$ is specified as:

$$\int_\Omega (\bullet)(\mathbf{x}) d\Omega \approx \sum_e \sum_{K \in nodes(e)} (\bullet)(\mathbf{x}_K) \jmath(\mathbf{x}_K) w_K \tag{5.50}$$

where e iterates all the elements in the mesh, and K runs over all the quadrature points in the element. Furthermore $\mathbf{x}_K$ is the location of the quadrature point (node), $\jmath(\mathbf{x}_K)$ is the Jacobian of the isoparametric mapping, and w_K is the weight of the quadrature point. Realizing that the velocity gradient vector $\boldsymbol{\eta}$ is multivalued at node K, meaning that it is separately evaluated in each element $e|_K$ connected at node K, the summations can be switched and then the nodal quadrature expressed as

$$\int_\Omega \boldsymbol{\eta} d\Omega \approx \sum_K \sum_{e|_K} \frac{A_e}{3} \sum_J \mathbf{G}_J|_e \mathbf{u}_J \tag{5.51}$$

$$\int_\Omega \bar{\boldsymbol{\eta}} d\Omega \approx \sum_K \sum_{e|_K} \frac{A_e}{3} \sum_J \overline{\mathbf{G}_J}|_K \mathbf{u}_J = \sum_K \left(\sum_{e|_K} \frac{A_e}{3} \right) \sum_J \overline{\mathbf{G}_J}|_K \mathbf{u}_J \tag{5.52}$$

where $J, K = 1, \ldots, N_{node}$ and N_{node} is the total number of the mesh nodes. In equation (5.52), the assumed velocity gradient $\bar{\boldsymbol{\eta}}$ has the form:

$$\bar{\boldsymbol{\eta}} = \bar{\mathcal{G}} \mathbf{u}. \tag{5.53}$$

The operator $\bar{\mathcal{G}}$ will be determined below in its discretizated version $\overline{\mathbf{G}_J}|_K$. In

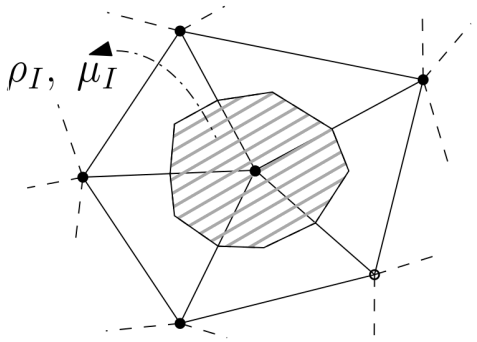

Figure 5.7: Nodal integration: area associated with node I. Material proprieties, like density ρ_I and viscosity μ_I, are directly defined in the integration point (node) I.

the previous equation the summation between parenthesis represents the area pertinent at each node (figure 5.7). Imposing that the elemental integration and the nodal integration should be equal:

$$\int_{\Omega_t} \mu \nabla_x \mathbf{u} : \nabla_x \mathbf{w} d\Omega_t - \int_{\Omega_t} \mu \overline{\nabla_x} \mathbf{u} : \nabla_x \mathbf{w} d\Omega_t = \tag{5.54}$$

$$\int_{\Omega_t} \mu \boldsymbol{\lambda}^T \boldsymbol{\eta} d\Omega_t - \int_{\Omega_t} \mu \boldsymbol{\lambda}^T \bar{\boldsymbol{\eta}} d\Omega_t = \int_{\Omega_0} \mu \boldsymbol{\lambda}^T (\boldsymbol{\eta} - \bar{\boldsymbol{\eta}}) d\Omega_0 = 0 \tag{5.55}$$

the discrete version of the previous equation leads to:

$$\sum_K \boldsymbol{\lambda}_K^T \left(\sum_{e|_K} \frac{A_e}{3} \sum_J \mathbf{G}_J|_e \mathbf{u}_J - \left(\sum_{e|_K} \frac{A_e}{3} \right) \sum_J \overline{\mathbf{G}_J}|_K \mathbf{u}_J \right) = 0 \tag{5.56}$$

but considering that the $\boldsymbol{\lambda}_K$ is arbitrary:

$$\sum_{e|_K} \frac{A_e}{3} \sum_J \mathbf{G}_J|_e \mathbf{u}_J - \left(\sum_{e|_K} \frac{A_e}{3} \right) \sum_J \overline{\mathbf{G}_J}|_K \mathbf{u}_J = \mathbf{0} \tag{5.57}$$

reversing the order of the summations,

$$\sum_J \left(\sum_{e|_K} \frac{A_e}{3} \mathbf{G}_J|_e \right) \mathbf{u}_J - \sum_J \left(\left(\sum_{e|_K} \frac{A_e}{3} \right) \overline{\mathbf{G}_J}|_K \right) \mathbf{u}_J = \mathbf{0} \tag{5.58}$$

$$\sum_J \left(\sum_{e|_K} \frac{A_e}{3} \mathbf{G}_J|_e - \left(\sum_{e|_K} \frac{A_e}{3} \right) \overline{\mathbf{G}_J}|_K \right) \mathbf{u}_J = \mathbf{0} \tag{5.59}$$

and considering that it has to be satisfied for each J separately

$$\sum_e \frac{A_e}{3} \mathbf{G}_J|_e - \left(\sum_e \frac{A_e}{3} \right) \overline{\mathbf{G}_J}|_K = \mathbf{0} \tag{5.60}$$

Finally the assumed differential operator is found:

$$\overline{\mathbf{G}_J}|_K = (\sum_{e|_K} \frac{A_e}{3})^{-1} \sum_{e|_K} \frac{A_e}{3} \mathbf{G}_J|_e \tag{5.61}$$

$$\overline{\nabla_x N_J(\mathbf{x}_K)} = \frac{\sum_{e|_K} \jmath(\mathbf{x}_K) w_K \left[\nabla_x N_J(\mathbf{x}_K) \right]}{\sum_{e|_K} \jmath(\mathbf{x}_K) w_K} \tag{5.62}$$

where

$$\nabla_x N_J(\mathbf{x}_K) = \left[\frac{\partial N_J(\mathbf{x}_K)}{\partial x}, \frac{\partial N_J(\mathbf{x}_K)}{\partial y} \right] \tag{5.63}$$

The test function $\overline{N_j}$ expressed in the nodal formulation is the same of the element formulation:

$$\overline{N_J(\mathbf{x}_K)} = \frac{\sum_{e|_K} \jmath(\mathbf{x}_K) w_K N_J(\mathbf{x}_K)}{\sum_{e|_K} \jmath(\mathbf{x}_K) w_K} = N_J(\mathbf{x}_K) = 0 \qquad \textit{if } J \neq K \tag{5.64}$$

$$\overline{N_J(\mathbf{x}_K)} = \frac{\sum_{e|_K} \jmath(\mathbf{x}_K) w_K N_J(\mathbf{x}_K)}{\sum_{e|_K} \jmath(\mathbf{x}_K) w_K} = N_J(\mathbf{x}_K) = 1 \qquad \textit{if } J = K \tag{5.65}$$

The shape function of each node can be thought of as constant with value 1 inside the area referred to the node (figure 5.7) and equal to zero outside.

Considering now figure 5.8, the new formulation leads to:

$$\overline{\nabla_x N_{J_i}(\mathbf{x}_I)} = \frac{\sum_{e|_I} \frac{V_e}{3} \left[\nabla_x N_{J_i}(\mathbf{x}_I) \right]}{\sum_{e|_I} \frac{V_e}{3}} \tag{5.66}$$

$$N_{J_i}(\mathbf{x}_I) = 0 \tag{5.67}$$

where $i = 1, \ldots, N_I$, where in figure 5.8 $N_I = 5$.

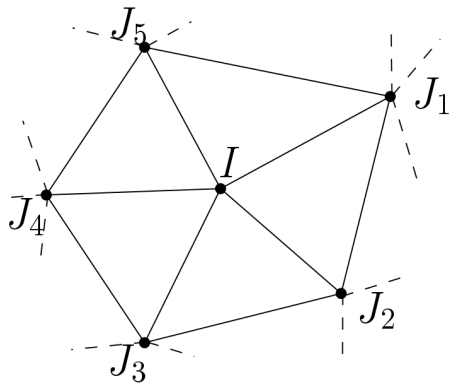

Figure 5.8: Nodal integration: patch of the node I.

The nodally integrated formulation can now be used to rewrite the discretized system of equations (5.31) and (5.32), as follow

$$\overline{\mathbf{M}}\frac{\mathbf{V}^{n+1}-\mathbf{V}^{n}}{\Delta t}+(\overline{\mathbf{K}}+\overline{\mathbf{K}}_{slip}+\overline{\mathbf{K}}_{c})\mathbf{V}^{n+1}+\overline{\mathbf{D}}^{T}\mathbf{P}^{n+1} = \overline{\mathbf{B}} \tag{5.68}$$

$$\overline{\mathbf{D}}\mathbf{V}^{n+1} = \mathbf{0} \tag{5.69}$$

where all the matrix have been computed using the nodal integration. The same stabilization technique described in chapter 4, can be formulated using the described nodal integration. In the following tests, the fractional step method has been used with nodal integration. Two 2D tests, using the new formulation are presented in what follow. Here the focus is on the comparison between the two different integration formulations. All the other simulations that will be discussed in chapters 6 and 7, instead, have been performed using the classical elemental formulation.

5.9.1 Sloshing in a rectangular tank

Figure 5.9 shows the geometry of the problem, which is the sloshing of water in rectangular tank. Material parameters are listed in table 5.1. In this case, the Newtonian constitutive law is adopted (section 3.34) and the standard boundary

conditions of perfect adhesion are considered. The fluid oscillates in the rectangular tank from its original position. In figure 5.10 the pressure contours are plotted for two different instants. The results show a good agreement between the two integration schemes.

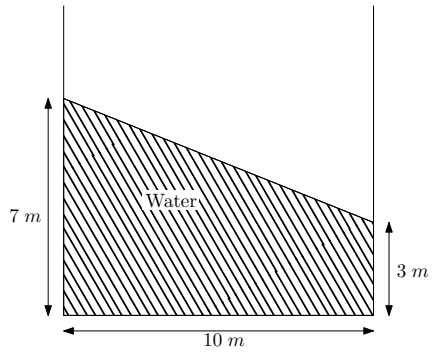

Figure 5.9: 2D geometry: sloshing of water in rectangular tank.

ρ (kg/m^3)	μ (Pa s)	nodes	T (s)	Δt (s)
1379	1	1586	10	0.0005

Table 5.1: Water material parameters, number of nodes, physical time and time step.

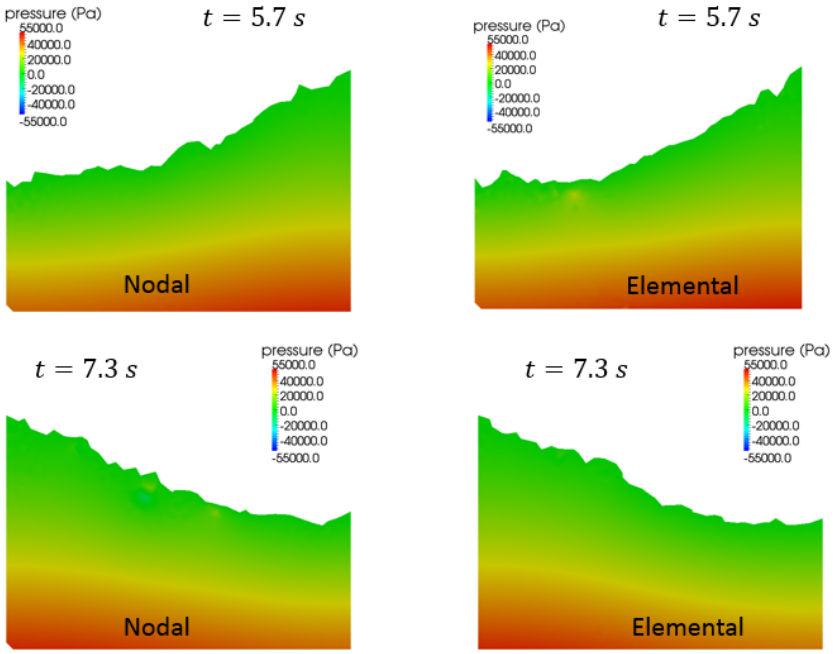

Figure 5.10: 2D sloshing of water in rectangular tank. Comparison between element and nodal integration: pressure contours at $t = 5.7, 7.3$ s.

5.9.2 Granular flow on a rigid obstruction

The second test performed with the nodal integration is the granular flow on a rigid obstruction. The experimental test has been performed in Moriguchi et al., 2009 and the geometry is represented in figure 5.11. The same test has been performed in Cremonesi and Perego, 2013. Material parameters are shown in table 5.2. The mesh is constructed with 1171 nodes and the analysis with a the time step of 0.0005 s. In this case, the rigid viscoplastic material model, described in section 3.5.2, is adopted and slip boundary conditions are applied on the boundary. Figure 5.12 shows the comparison between the elemental and nodal formulation while in figure 5.12 the impact force measured on the rigid obstruction is plotted. The comparison between the pressure fields shows that in the nodal formulation more oscillations of the pressure field appear. Nevertheless a fairly good agreement between the two formulations is obtained. The comparison in figure 5.12 shows that the nodally integrated formulation underrates the impact force. Results show that a more detailed investigation on the nodal integration is necessary.

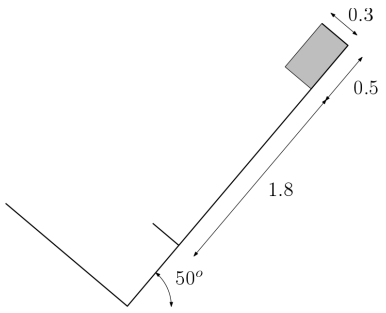

Figure 5.11: Granular flow on a rigid obstruction: schematic representation of the problem.

ρ (kg/m^3)	μ (Pa s)	ϕ	ϕ_{basal}	h_{slip} (m)	Δt (s)
1379	0.001	35°	35°	0.03	0.0005

Table 5.2: Material parameters

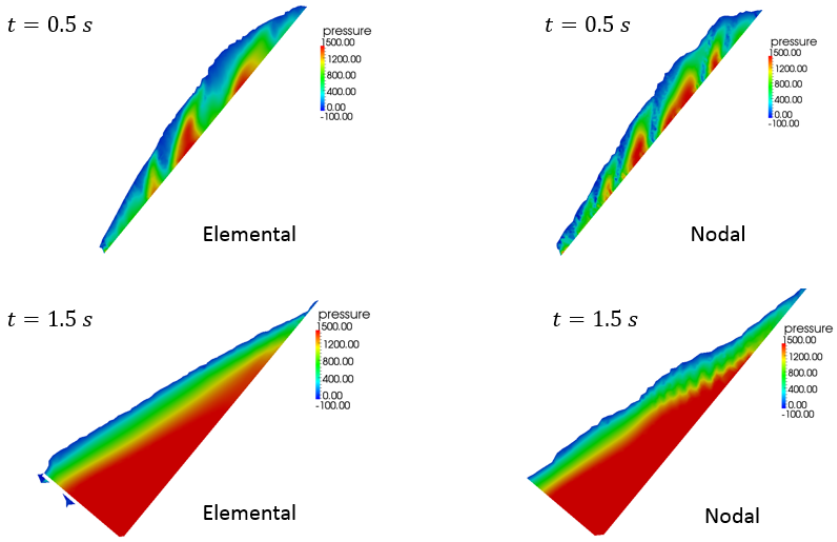

Figure 5.12: Granular flow on a rigid obstruction: comparison between elementally and nodally integrated formulation: pressure contours at $t = 0.5, 1.5$ s.

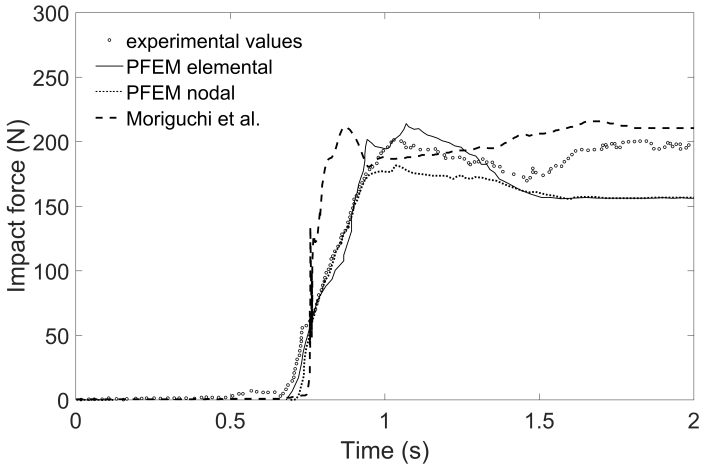

Figure 5.13: Granular flow on a rigid obstruction: impact force time histories. Comparison between experimental, numerical results of Moriguchi et al., 2009 and the nodal and elemental integration of the present work (PFEM).

6

Numerical simulation of small scale experiments

In this chapter the simulations of some laboratory tests are presented and discussed. Different geometries, materials and released volumes are considered. These tests are used to validate the model with focus on the importance of slip boundary conditions. The constitutive model discussed in the previous chapter for a rigid viscoplastic material (see section 3.5.2) with slip boundary conditions (see chapter 5.1) is here adopted. In the analyses, the following numerical parameters have been used: $\Delta t = 0.0002$ s, $N = 100$, $\alpha = 1.6$ and $\frac{1}{\varepsilon} = 10^7$, where N is the parameter of the regularized apparent viscosity (section 3.5.2), α is the parameter used in the alpha-shape algorithm (section 4.6.2) and $\frac{1}{\varepsilon}$ is the penalization term to prevent normal velocity at the slip boundary (section 5.6). Computational time information, that will be provided in this chapter and in chapter 7, are referred to a machine with the following characteristic: `Intel(R) Xeon(R) CPU ES-2687W 0 @ 3.10GHz`.

6.1 Chute of a granular mass along inclined planes

Three experimental tests performed by Manzella at the Ecole Polytechnique Fédéral de Lausanne are considered (Manzella, 2008). The tests consist of the free chute of a granular material along inclined planes. Two different geometries, with one or two inclined planes, are considered (see figure 6.1). The inclination of the plane for the first test is 45° (figure 6.1(a)) while for the second the two planes are inclined by 37.5° and 22.6° respectively (figure 6.1(b)). The test on the first geometry is performed using aquarium gravel while on the second one both aquarium gravel and Hostun sand are used.

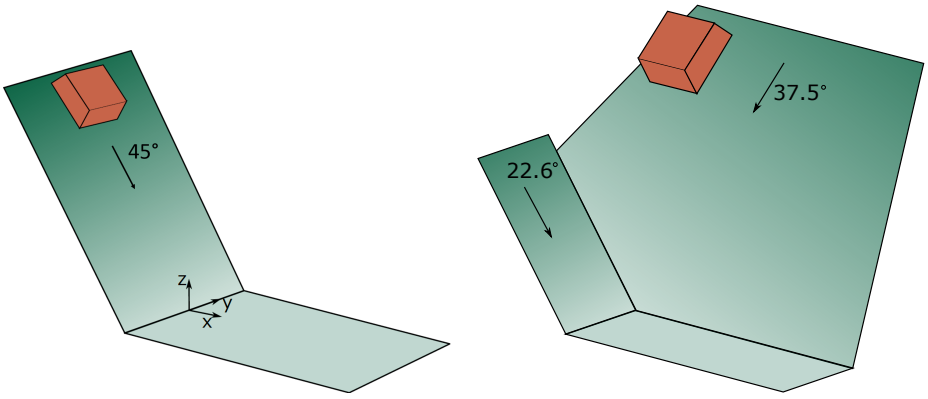

(a) (b)

Figure 6.1: Chute of a granular mass along inclined planes. Tests setup and granular mass initial positions.

The material parameters for gravel provided in (Manzella, 2008), are: density $\rho = 1430$ Kg/m^3, friction angle $\varphi = 34°$ and basal friction angle $\varphi_{basal} = 28°$. The total volume of gravel is 0.02 m^3 for the first test and 0.03 m^3 for the second. Material parameters are listed in table 6.1.

The model needs two additional parameters: the initial viscosity μ and the amount of slip β (or h_{slip} alternatively). These parameters are identified on the basis of the first test then used in the second one. An initial mesh of 240902

	material	geometry	material parameters		
			ϕ	ϕ_{basal}	ρ (kg/m^3)
test 1	aquarium gravel	fig. 6.1(a)	34°	28°	1430
test 2	aquarium gravel	fig. 6.1(b)	34°	28°	1430
test 3	Hostun sand	fig. 6.1(b)	34°	32°	1260

Table 6.1: Summary of the material parameter used in the previous tests

tetrahedra with 95422 nodes has been used for the case with 1 inclined plane, while the tests with 2 inclined planes have been simulated with a mesh of 301269 tetrahedra with 114710 nodes. The average element size is $h^e = 0.01$ m for both meshes. This information is summarized in table 6.2.

	mesh		
	h^e (m)	nodes	tetrahedra
test 1	0.01	95422	240902
test 2	0.01	114710	301269
test 3	0.01	114710	301269

Table 6.2: Mesh information for the presented simulations, where h^e is the mesh size. The number of tetrahedra is refereed to the first time step.

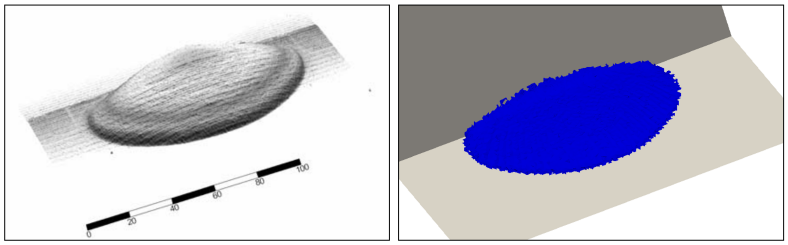

Figure 6.2: Chute of a granular mass along inclined planes. One inclined plane. Final deposit at $t = 2.3$ s: experimental (left) and numerical (right), with $\mu = 1$ Pa s, $h_{slip} = 0.04$ m.

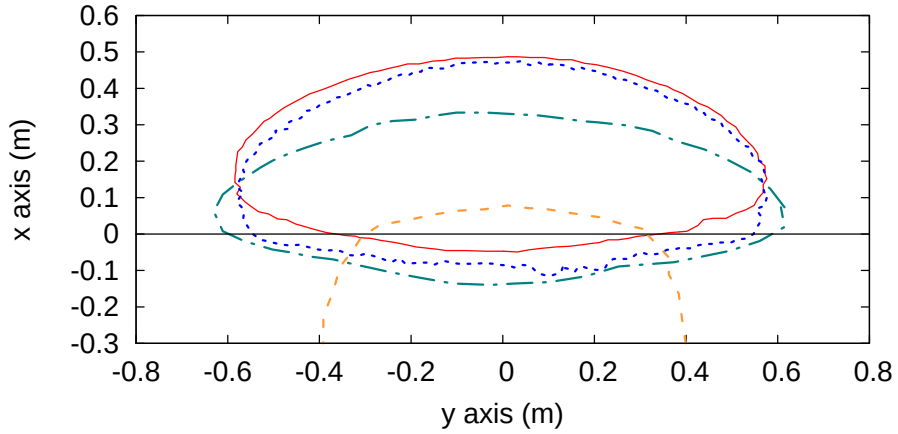

(a) top view

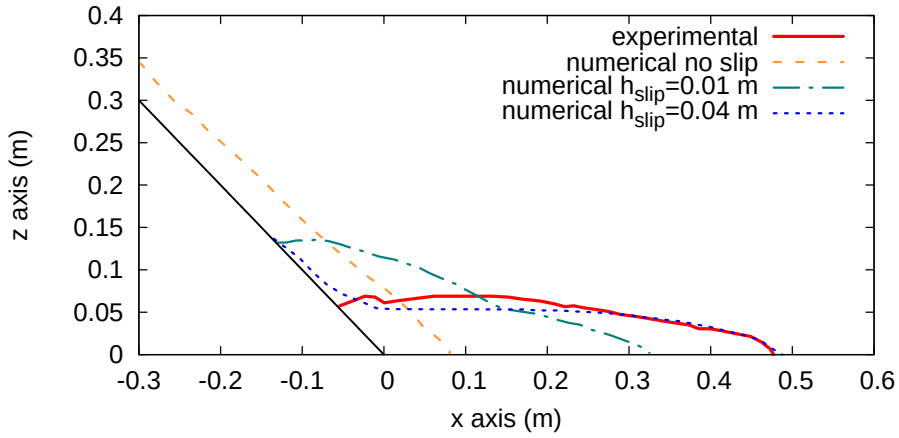

(b) section

Figure 6.3: Chute of a granular mass along inclined planes. One inclined plane. Comparison of the final deposit with $\mu = 1$ Pa s, at $t = 2.3$ s.

Experimental and numerical final deposits for the first test (one inclined plane) are compared in figure 6.2 and figure 6.3. Figure 6.3(a) shows a view of the final deposit in the $x - y$ plane (see figure 6.1 for the reference system), while its vertical section in the $x - z$ plane is shown in figure 6.3(b). The two graphs

show the effect of the amount of slip at the interface (h_{slip}) on the final results. The final deposit obtained at $t = 2.3$ s with no slip condition ($h_{slip} = 0$) differs significantly from the experimental data. It can be observed that increasing the value of the slip, the slip velocity increases and consequently a larger distance is covered by the slide. A good agreement has been obtained setting $\mu = 1$ Pa s and $h_{slip} = 0.04$ m, with a ratio $h_{slip}/h^e = 4$.

The same parameters are then used to simulate the second test (two inclined planes, figure 6.1b). In figure 6.4 a sequence of snapshots of numerical simulation for different time instants, with contour plots of the velocity magnitude, are shown. A sequence of synchronized snapshots of the experimental and numerical runouts is comparatively shown in figure 6.5, a good agreement with the experiments can be observed.

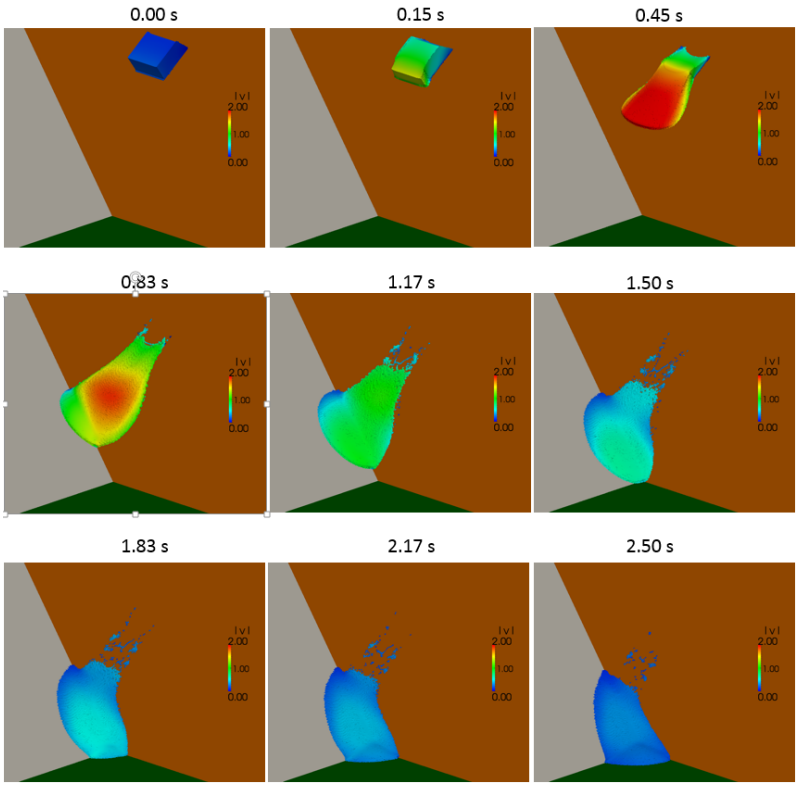

Figure 6.4: Chute of a Hostun sand along two inclined planes. Plot of the velocity field with $\mu = 1Pas$ and $h_{slip} = 0.04$ m, at different time instants.

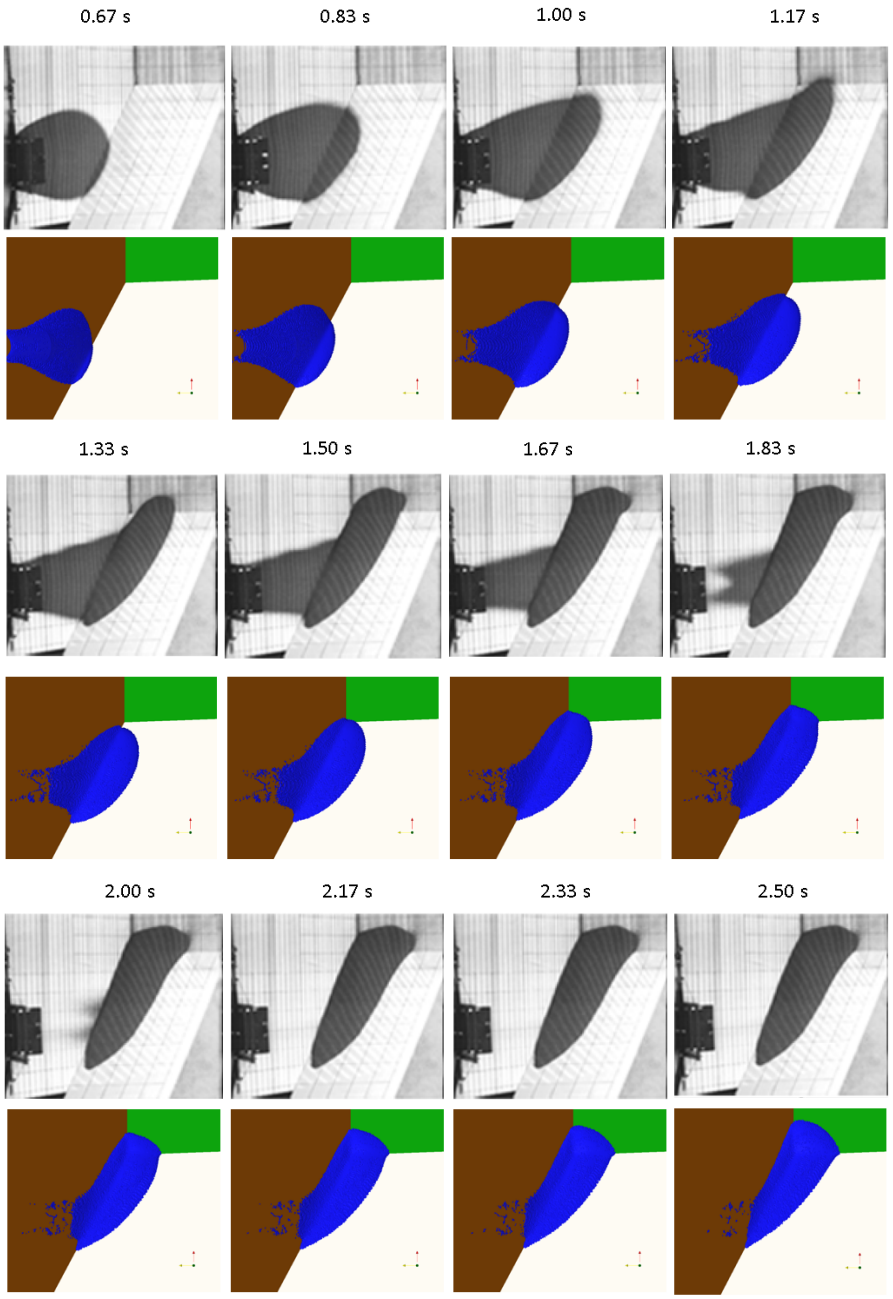

Figure 6.5: Chute of a granular mass along inclined planes. Two inclined planes. Comparison between experimental test (top) and numerical results (bottom) with $\mu = 1Pas$ and $h_{slip} = 0.04$ m, at synchronized time instants.

In the work of (Manzella, 2008) the second test (two inclined planes, figure 6.1b) has been also carried out with Hostun sand, which is a finer material than gravel. The grain size distribution (diameter) of Hostun sand is $0.32 - 0.8$ mm while the gravel one is $0.5 - 3$ mm. Material parameters provided in (Manzella, 2008) for Hostun sand are: density $\rho = 1260$ Kg/m^3, friction angle $\varphi = 34°$ and basal friction angle $\varphi_{basal} = 32°$ (table 6.1). In figure 6.6 a sequence of

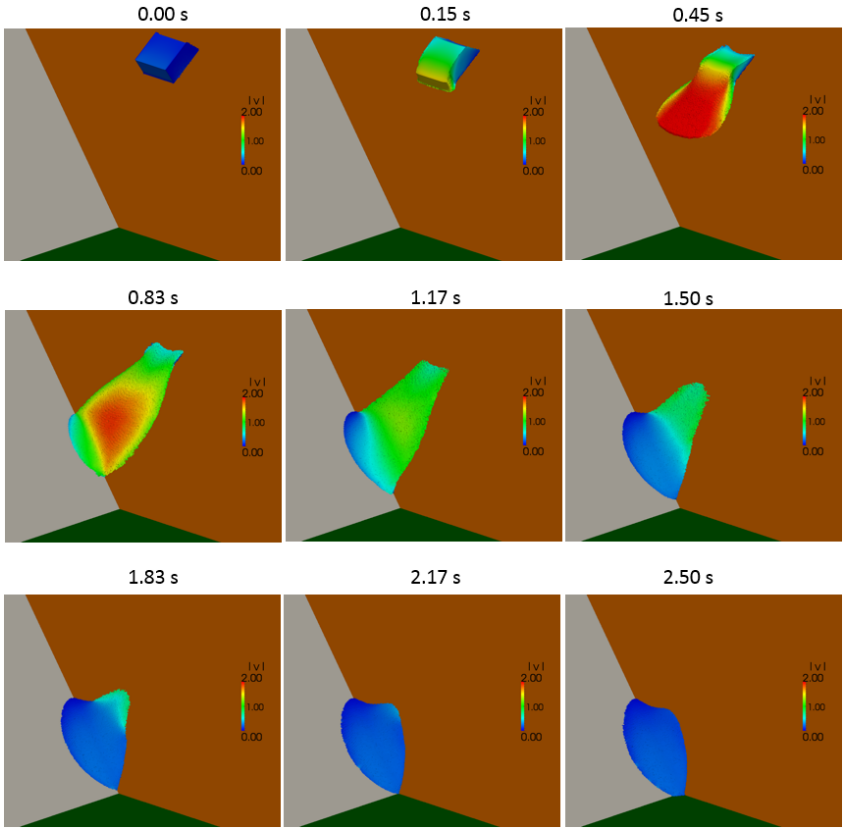

Figure 6.6: Chute of a Hostun sand along two inclined planes. Plot of the velocity field with $\mu = 1Pas$ and $h_{slip} = 0.015$ m, at different time instants.

snapshots of numerical simulation for different time instants, with contour plots of the velocity magnitude, are shown. A sequence of synchronized snapshots of

the experimental and numerical runouts is comparatively shown in figure 6.7. In this case with $h_{slip} = 0.015$ m and $h_{slip}/h_e = 1.5$. This value of h_{slip} is in accordance with (Schaefer et al., 2010) (see section 5.1) where it has been observed that the slip velocity between the flowing mass and the basal surface increases with the average grain diameter. This test has also been simulated in (Pastor et al., 2009a, 2015) using the same constitutive parameters but without slip velocity at the interface. A good agreement with the experiments can be observed.

A view of the boundary of the final deposit in the $x - y$ plane at $t = 2.5$ s for aquarium gravel with $h_{slip} = 0.04$ m and for Hostun sand with $h_{slip} = 0.015$ m is also shown in figures 6.16 and 6.8(b), respectively. Also in this case, a good agreement with the experimental final deposit can be observed for both materials. In table 6.3 information on the physical and computational time, volume and height of release are shown.

	time			
	physical	computational	volume (m^3)	ΔH (m)
test 1	2.0 s	23 hours	0.02	1
test 2	2.5 s	31 hours	0.03	1
test 3	2.5 s	31 hours	0.03	1

Table 6.3: Time and geometrical information for the presented simulations. ΔH indicates the vertical distance between the center of mass of the granular material initial position and the horizontal plane.

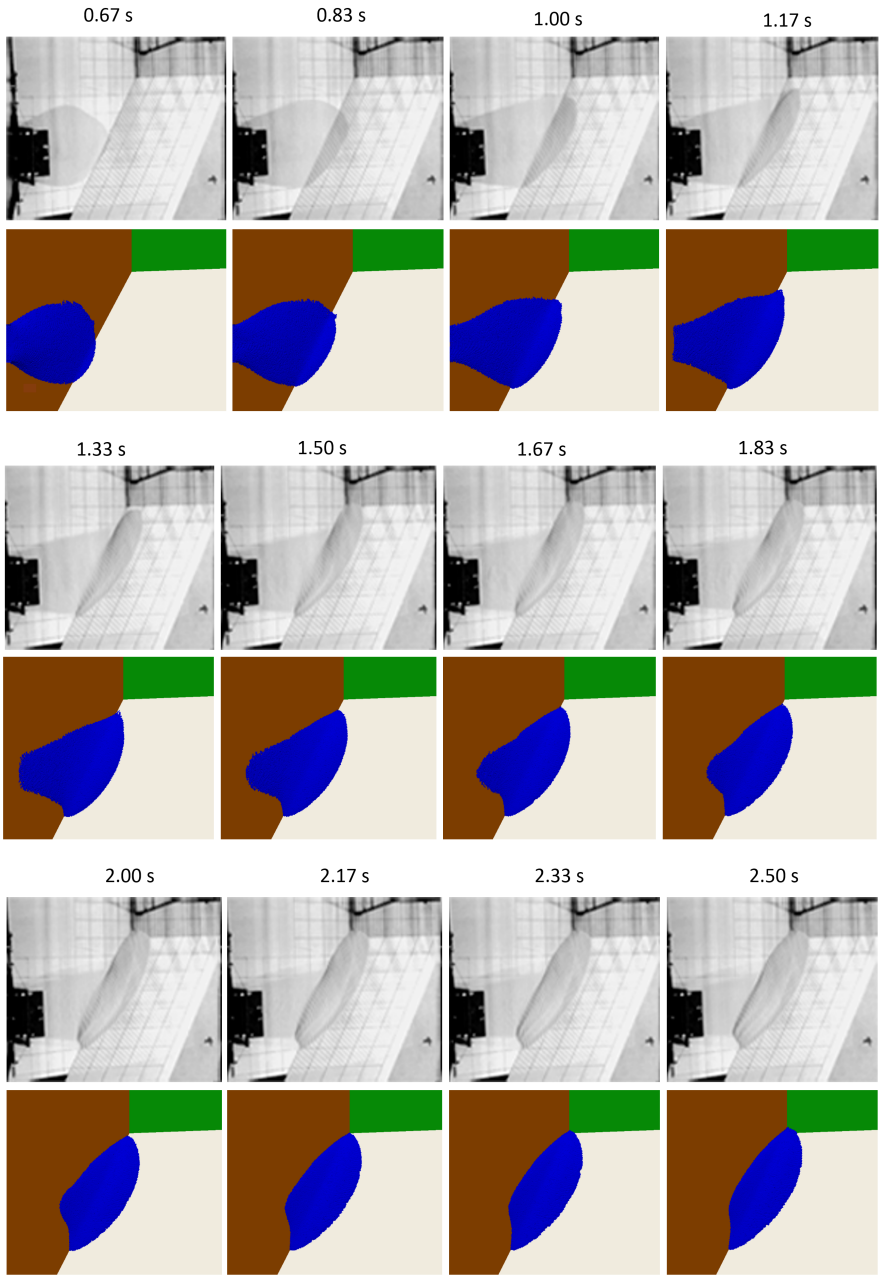

Figure 6.7: Chute of a Hostun sand along two inclined planes. Comparison between experimental test (top) and numerical results (bottom) with $\mu = 1Pas$ and $h_{slip} = 0.015$ m, at synchronized time instants.

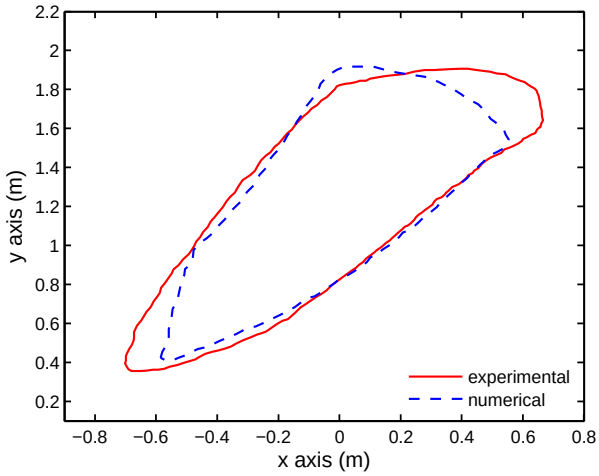

(a)

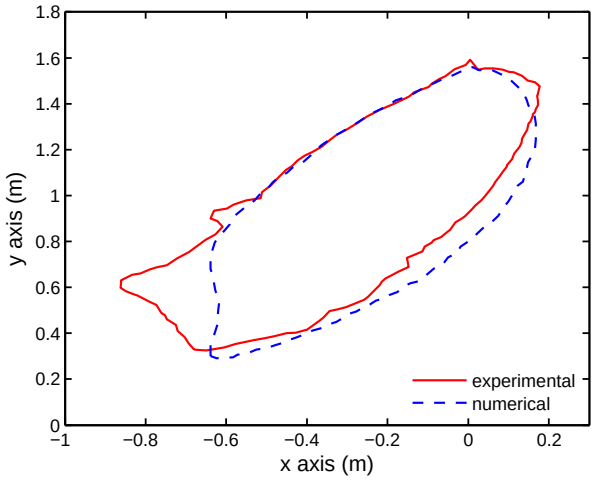

(b)

Figure 6.8: Chute of gravel (a) and Hostun sand (b) along two inclined planes. Comparison of the final deposits at $t = 2.5$ s, with $\mu = 1$ Pa s and $h_{slip} = 0.04$ m (a) and with $\mu = 1$ Pa s and $h_{slip} = 0.015$ m (b).

6.2 Chute of a granular mass on an erodible substrate

In this example, the tests performed in (Crosta et al., 2014) are simulated numerically. The chute of a mass of granular material along two planes of different inclination (40° and 60° respectively) is considered. A horizontal box is placed at the bottom of the inclined plane. Two different situations are investigated. In the first one, the material flows along the inclined plane and then it impacts against the empty box (see figure 6.9(a)). In the second case, the box is filled with a small layer (5 mm) of erodible granular material (see figure 6.9(b)).

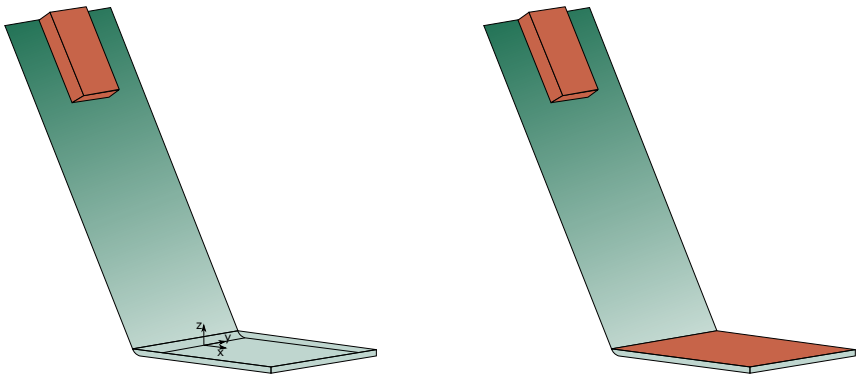

(a) (b)

Figure 6.9: Chute of a granular mass on an erodible substrate. Initial position of sand mass: (a) without erodible substrate; (b) with erodible substrate.

The material used in this examples is Hostun sand. Material parameters are provided in (Crosta et al., 2014): density $\rho = 1420$ Kg/m^3, friction angle $\varphi = 32°$ and basal friction angle $\varphi_{basal} = 25°$. In accordance with the previous example, a viscosity of $\mu = 1$ Pa s is used also for these tests. The same material is used also for the erodible substrate.

Material parameters are listed in table 6.4. For the case without an erodible substrate, the following initial meshes have been used, with an average mesh size

		material parameters		
	geometry	ϕ	ϕ_{basal}	ρ (kg/m^3)
40°	6.9(a)	32°	25°	1420
60°	6.9(a)	32°	25°	1420
40° substrate	6.9(b)	32°	25°	1420
60° substrate	6.9(b)	32°	25°	1420

Table 6.4: Summary of the material parameter of in the previous analyses

$h^e = 0.007$ m: 133318 tetrahedra with 49477 nodes for the 40° case; 133604 tetrahedra with 49529 nodes for the 60° case. For the case with an erodible substrate, the following initial meshes have been used, still with an average mesh size $h^e = 0.007$ m (the larger number of elements is due to the fact that also the erodible substrate need be discretized): 379243 tetrahedra with 94031 nodes for the 40° case; 379548 tetrahedra with 95749 nodes for the 60° case. This information are summarized in table 6.5. In table 6.6 information on the physical

	mesh		
	h^e (m)	nodes	tetrahedra
40°	0.007	49477	133318
60°	0.007	49529	133604
40° substrate	0.007	94031	379243
60° substrate	0.007	95749	379548

Table 6.5: Mesh information for the presented simulations, where h^e is the mesh size. The number of tetrahedra is refered to the first time step.

and computational time, volume and height of release is shown. In a first instance, the test with no erodible substrate has been performed with $h_{slip} = 0$ (no slip at the interface). In the case with an inclination angle of 40° after less than 0.2 s, the

	time			
	physical	computational	volume (m^3)	ΔH (m)
40°	1.2 s	12 hours	0.0034	0.3
60°	1.2 s	12 hours	0.0034	0.3
40° substrate	1.2 s	27 hours	0.0034	0.3
60° substrate	1.2s	27 hours	0.0034	0.3

Table 6.6: Time and geometrical information and of the presented simulations. ΔH indicates the vertical distance between the center of mass of the granular material initial position and the horizontal plane.

front stops advancing, before the material has completely reached the horizontal plane, while in the case with 60° the final front position differs significantly from the experimental data, as shown in figure 6.10.

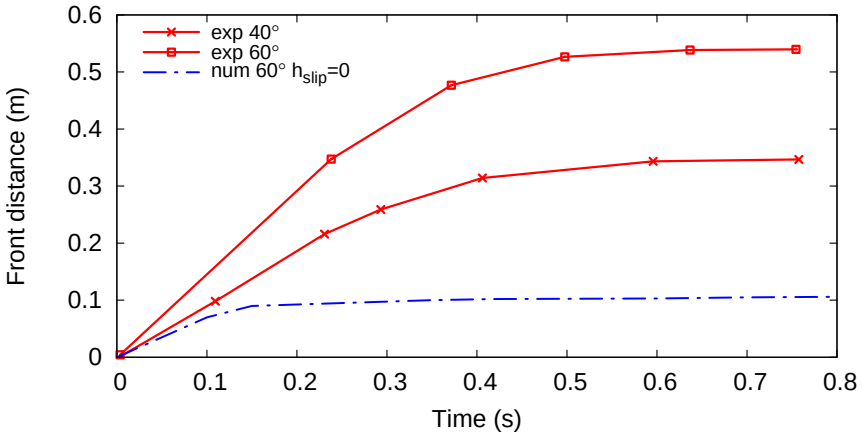

Figure 6.10: Chute of a granular mass on an erodible substrate. Front distance evolution. Results without slip at the interface.

Considering now the possibility of slip at the interface, the slip length should be identified. As in the previous example, the first test is used to calibrate the

value h_{slip}, while the second is used to validate the results. The plot of figure 6.11 shows the time evolution of the front distance for the first case (no erodible substrate), comparing numerical results and experimental data for the two plane inclinations. Two values of h_{slip} are considered, showing that better results can be obtained using $h_{slip} = 0.05m$, with a ratio $h_{slip}/h^e \cong 7$.

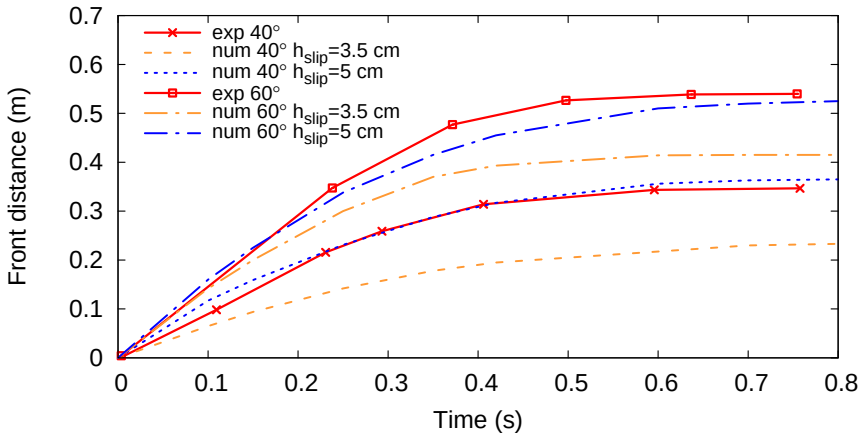

Figure 6.11: Chute of a granular mass on an erodible substrate. Front distance evolution. Test 1 (without erodible material).

The second test (with erodible substrate) is simulated using the parameters identified in the first test, and is shown in figures 6.12 and 6.13, for the cases of 40° and 60°, respectively. The snapshots are plotted on the vertical middle plane of the experimental setup.

The front distance evolution for the second test is plotted in figure 6.14. A satisfactory agreement is obtained also in this case for the 40° inclination. In the 60° case, the numerical solution seems to underestimate the run front distance. However, it should be noted that, in the case of the erodible substrate, the experimental identification of the front position is problematic due to the difficulty to distinguish between the granular material of the moving landslide and the erodible substrate.

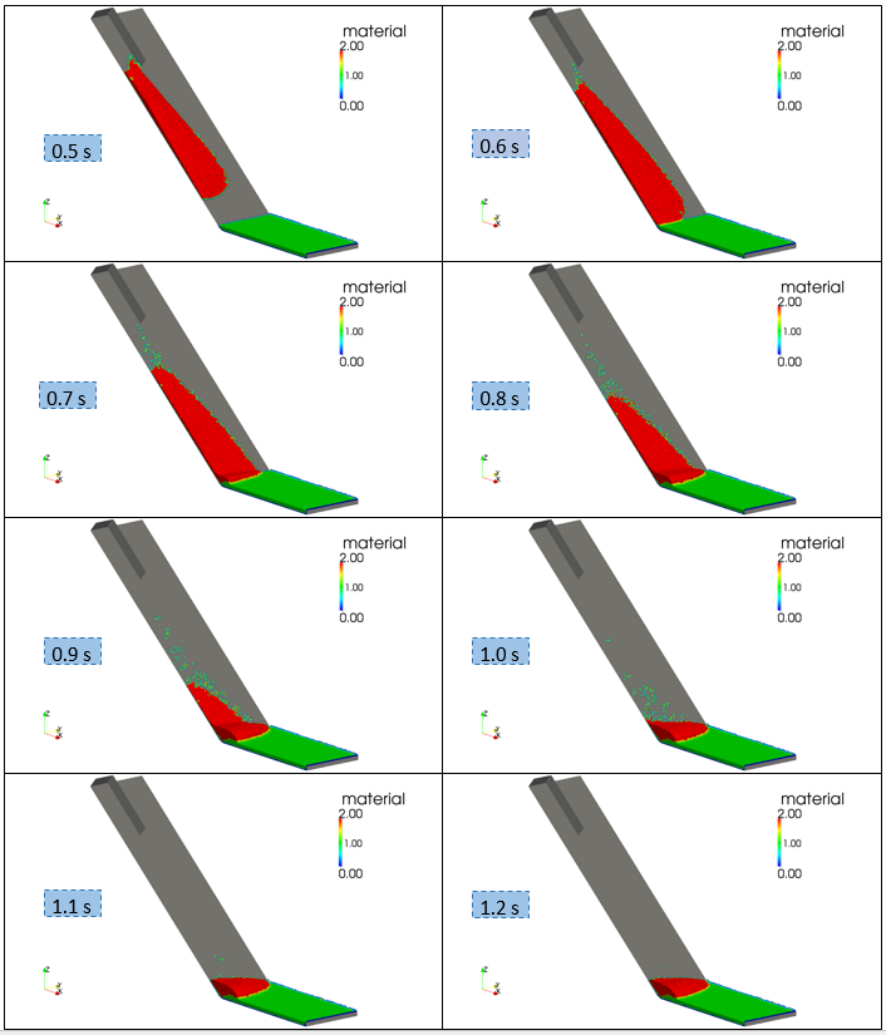

Figure 6.12: Chute of a granular mass along a plane inclined of 40° with erodible substrate, with $\mu = 1$ Pa s and $h_{slip} = 0.05$ m. Snapshots at different time instants. The green color indicates the erodible substrate while the red one indicates the material flowing from the inclined plane. The blue color indicates the basal layer.

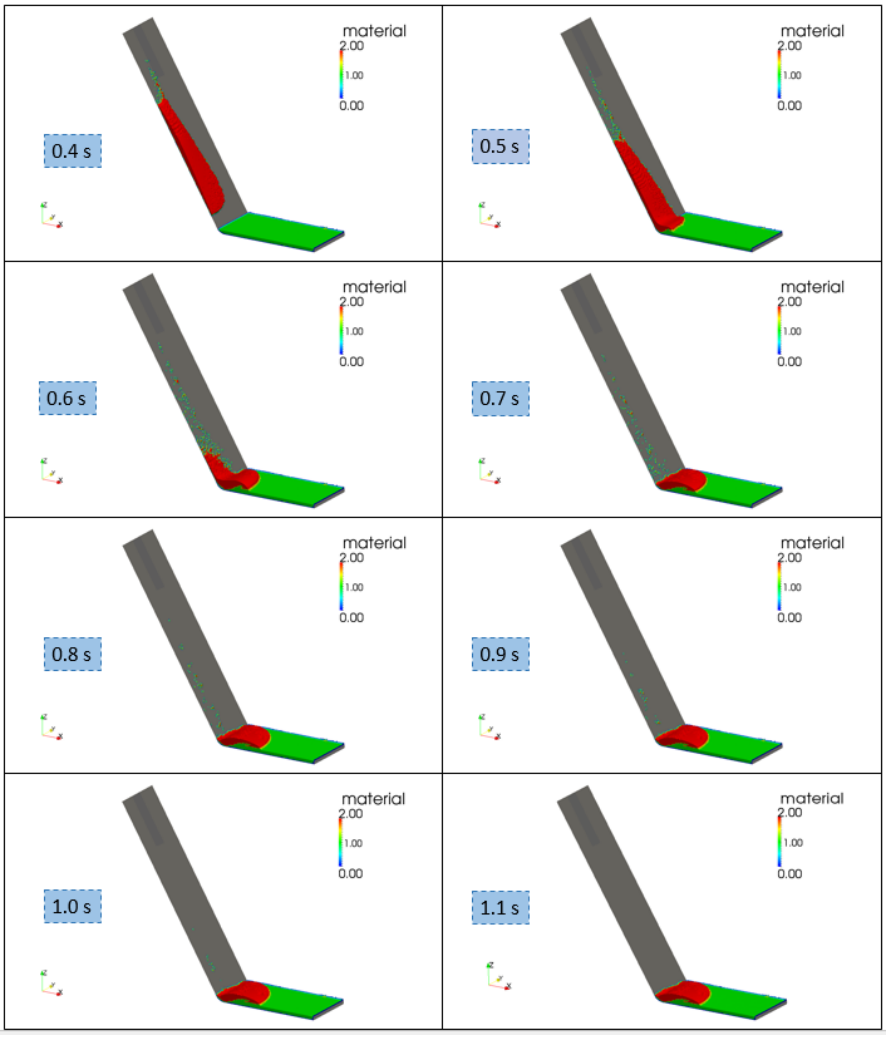

Figure 6.13: Chute of a granular mass along a plane inclined of 60° with erodible substrate, with $\mu = 1$ Pa s and $h_{slip} = 0.05$ m. Snapshots at different time instants. The green color indicates the erodible substrate while the red one indicates the material flowing from the inclined plane. The blue color indicates the basal layer.

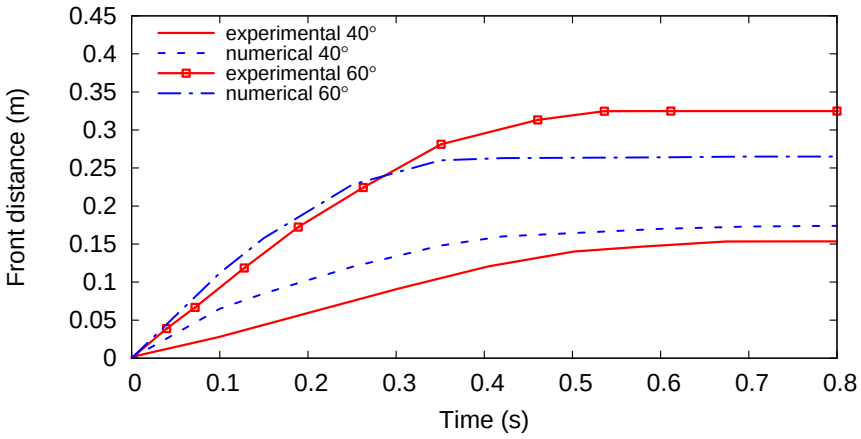

Figure 6.14: Chute of a granular mass on an erodible substrate. Front distance evolution. Test 2 (with erodible material, $h_{slip} = 0.035$ m).

Figure 6.15 shows snapshots with contour plots of the velocity magnitude at different time instants, plotted on the vertical middle plane of the experimental setup. The effect of the slipping interface can be appreciated in the enlarged inserts, showing a non-zero relative velocity between the flowing mass and the basal plane. Figure 6.16 shows the final deposit of the two tests with an enlarged view of the contour between the flowing material and the erodible substrate.

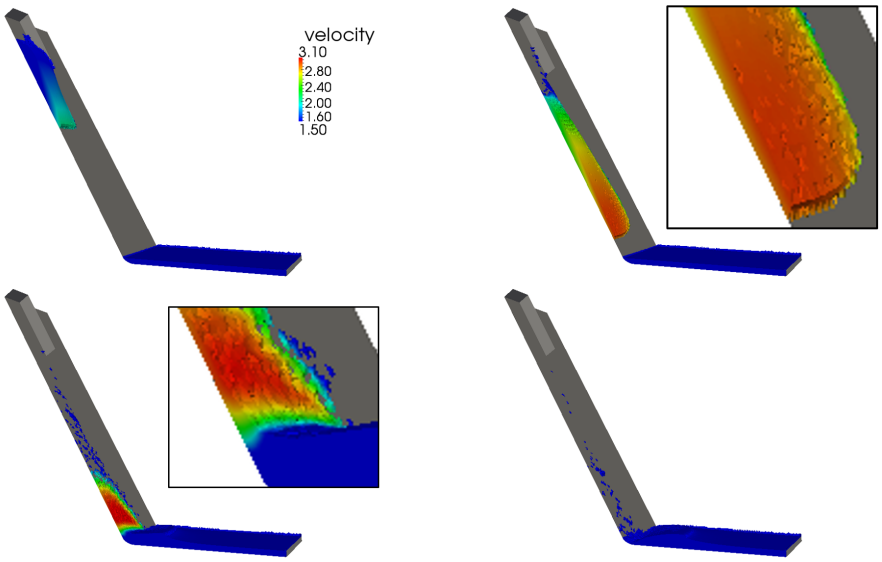

Figure 6.15: Chute of a granular mass on an erodible substrate. Test 2 (with erodible material). Snapshots at time instants $t = 0.2$ s, 0.4 s, 0.6 s and 0.8 s (from left to right, from top to bottom, respectively), with $h_{slip} = 0.035$ m.

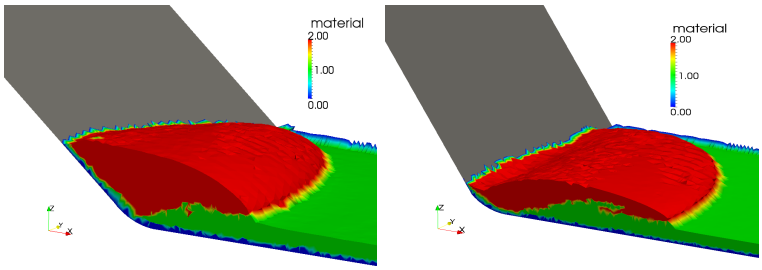

(a) (b)

Figure 6.16: Chute of Hostun sand on a plane inclined of 40° (a) and 60° (b). Comparison of the final deposits at $t = 1.2$ s, with $\mu = 1$ Pa s and $h_{slip} = 0.05$ m. The green color indicates the erodible substrate while the red one indicates the material flowing from the inclined plane. The blue color indicates the basal layer.

6.3 Mass variation

In the mechanics of incompressible fluids the mass conservation is an important issue, in the lagrangian framework especially, even though this problem exists also in the Eulerian and ALE approaches (Pelletier et al., 1989). In the lagrangian formulation, the mass loss is immediately observed (Aubry et al., 2006) since the particles are used to define the domain. In the proposed method, the issue of mass conservation is particularly critical, mainly due to the method employed for boundary identification. Various works have been presented to find a way to improve the mass conservation for incompressible fluids, in the PFEM approach. In (Ryzhakov et al., 2012), a second order fractional step scheme is used and the compressibility condition is applied on the intermediate velocity using a prediction of the end-step pressure. In (Oñate et al., 2014), a residual-based stabilized expression of the mass balance equation is obtained using the finite calculus method. An example of a critical situation for mass variation is the adding or removing of tetrahedra from a step to another. In particular, when a particle separates from the bulk of the fluid through the deletion of one or more elements, a mass equal to the total mass of the deleted elements is attached to the particle. If subsequently the same particle merges back within the bulk, the mass added to the bulk itself is not exactly the mass of the particle, but is the mass of the newly created elements which first connect the particle to the bulk according to the alpha-shape algorithm. This issue also affects the momentum balance equation, which is enforced separately for the bulk of the fluid and for the isolated particles. The momentum added to the bulk when an isolated particle is re-attached, is not exactly the momentum of the particle itself. Similar remarks also hold for the formation and annihilation of internal cavities.

In figures 6.17 the mass variation of the numerical simulation presented in section 6.1 and 6.2 is shown. For the tests of section 6.2 (figure 6.17(b)) the difference in the percentage mass variation between the cases with or without the erodible substrate, is due to the presence of the erodible substrate of Hostun

sand which is partially or totally at rest in the horizontal plane, for the entire simulation. Hence the mass variation of the sand of the erodible layer, which undergoes small displacements, is limited.

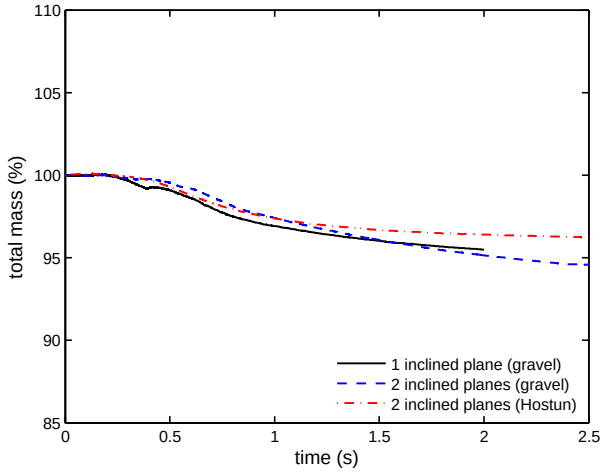

(a)

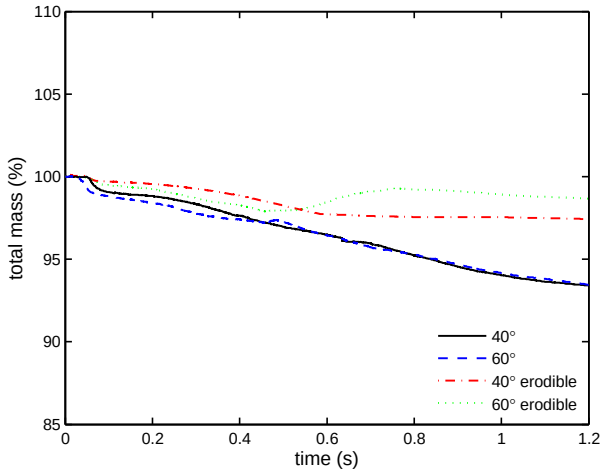

(b)

Figure 6.17: Mass percentage variation for the tests of section 6.1: chute of aquarium gravel (black and blue lines) and Hostun sand (red line) along one or two inclined planes (a). Mass percentage variation for the tests of section 6.2: chute of Hostun sand on an inclined plane without erodible substrate (black and blue lines) and with erodible substrate (red and green lines) (b).

7
Lanslides Simulations

In this chapter, the numerical simulations of three historical events are presented: the Cougar Hill dump flowslide, the Frank avalanche and the Vajont slide. A brief description of these events can be found in the introduction of this work. The constitutive model discussed in the previous chapters for a rigid-viscoplastic material (see section 3.5.2) with slip boundary conditions (see section 5.1) is here adopted. In the Vajont event, the mobilized material slips into the water reservoir, generating a huge wave. In this case both the terrain and the water have been modelled and simulated. Some remarks on large scale simulations are presented, before introducing numerical results.

7.1 Remarks on large scale simulation

Accurate digital elevation models, describing the terrain topography, are of primary importance to perform numerical simulation of real events. They can been obtained with different methods such as photogrammetry, lidar (laser imag-

ing detection and ranging) and land surveying. Digital elevation models can be involved in more general Geographical Information Systems (GIS) with the aim to analyses and evaluate the risk (see Morgenstern and Martin, 2008 for a review on application of GIS).

In this work the geometry of the problem can be defined starting from the discretization of two surfaces: the sliding surface and the free surface. The sliding surface represents the border of the simulation, it includes partially the slope topography before the event and entirely the surface of rupture (figure 7.16(a)). The free surface is the surface of the sliding material, before the event (figure 7.16(b)). The geometry of the slope is an important factor that strongly affects the propagation, the velocity and the run-out of a landslide. The code uses a set of ASCII data files which have to be prepared in order to run the problem. These files have to include a sets of points describing the discrete approximation of the boundary (sliding surface) and the free surface, as well as the volume of the moving terrain and/or water (figure 7.1(c)). All the previous points constitute nodes of the initial mesh of the problem.

A modification to the continuous re-triangulation strategy has been realized in order to reduce the computational time. In fact, considering the sliding surface of figure 7.16(a), most part of the nodes are not active during the analysis. Indeed the Delaunay triangulation can be performed only in a box containing all the active nodes. The box is a rectangular cuboid where the faces are defined starting from the maximum and minimum values of the $\mathbf{x}$ coordinates of the active nodes. In figure 7.2(a) the entire mesh is shown and the edges of the box are highlighted. The partial set of nodes used to perform the Delaunay triangulation is shown in figure 7.2(b). To allow the correct identification of the evolving boundary, the faces of the box have to be located at a distance Δh from the maximum and minimum values of the $\mathbf{x}$ coordinates of the active nodes. In the present work:

$$\Delta h = 3h \tag{7.1}$$

where h is the average smaller edge of all the elements (see section 4.6.2).

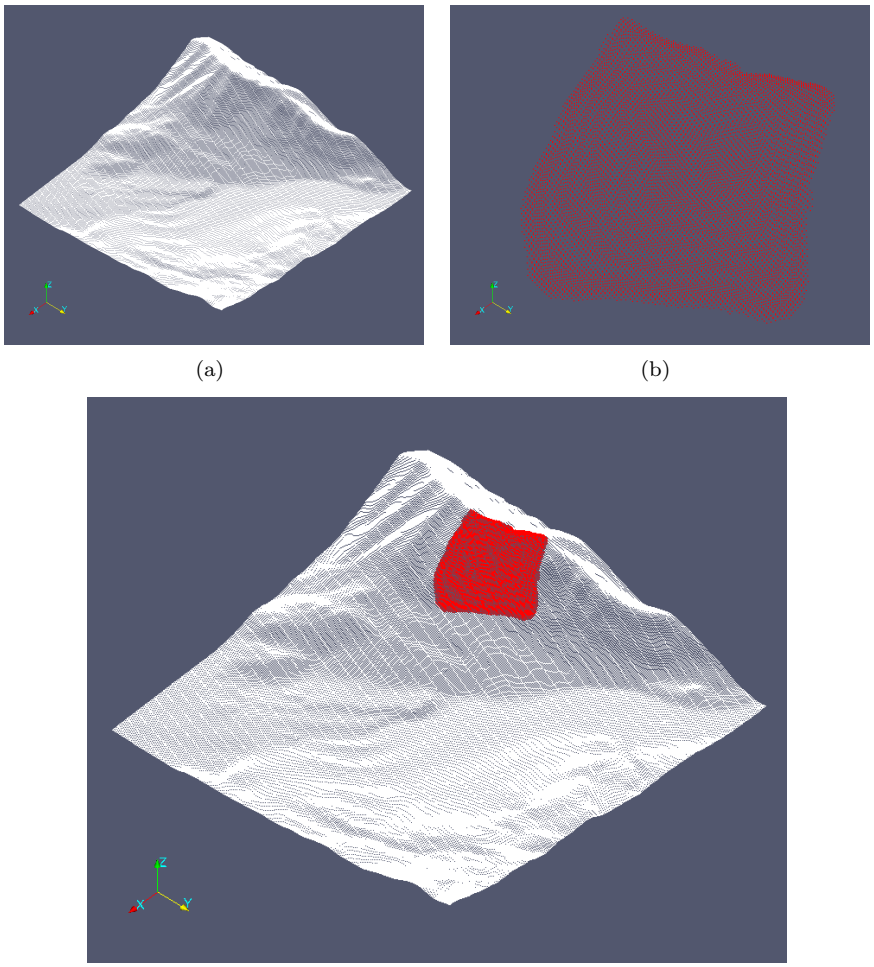

Figure 7.1: Discrete representation of the sliding surface (a), the free surface (b) and the complete mesh (c) of Frank avalanche.

Considering now the case of a tetrahedral initial mesh, at the end of step t^n, not excessively distorted to require a new triangulation, but with some nodes too close to each other. In this case the routine *add_rem* (see section 4.6.4) removes these and a new triangulation is necessary. Instead of performing a complete

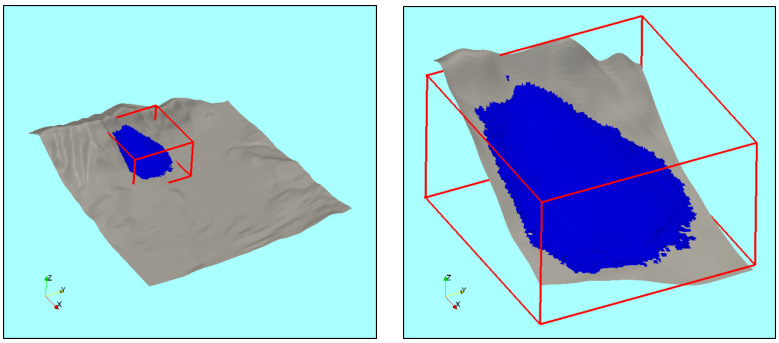

(a) (b)

Figure 7.2: Tessellation box: entire mesh and edges of the box (a), partial domain (b) where to perform the Delaunay triangulation.

triangulation, a partial one, involving only some nodes, can be performed. In the set of elements in figure 7.3(a) a node (figure 7.3(b)) does not respect the minimum distance to the closest node. In this case a constrained Delaunay triangulation is performed. The constrained Delaunay triangulation allows to triangulate a set of nodes bounded by triangular faces.

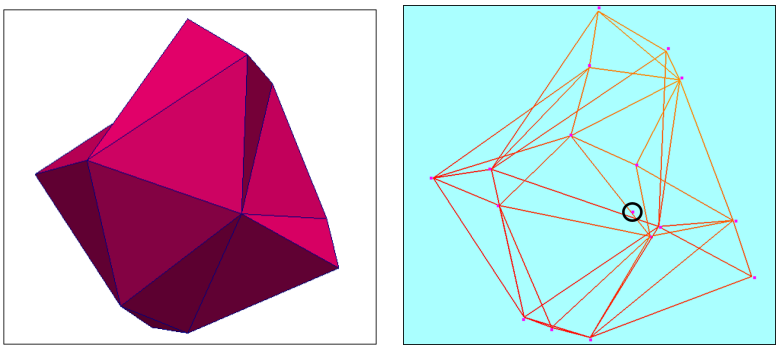

(a) (b)

Figure 7.3: Constrained Delaunay triangulation: set of tetrahedral elements (a) and set of nodes with one node that have to be removed (b).

7.2 Cougar Hill

On May 11, 1992, the Cougar 7 dump at the Greenhills Mine located near Elkford, British Columbia, failed. It is one of a large number of long runout flowslides that happened during 25 years in the Greenhills Mine (Dawson et al., 1998). Forty-eight landslides have been classified with a modal value of runout distance ranging from 500 m to 1000 m. All the events occurred rapidly even if the absence of a eyewitness did not allow for an accurate estimation of the physical propagation time. The considered event is the Greenhills Cougar 7 flowslide. Approximately 200000 m^3 of failure debris slid off the 100 m high waste dump, travelled across an access roadway, and flowed downslope for a total runout distance of 700 m. The dump slope was at an angle of repose of 37°-38°. The debris was mainly sandy gravel and the foundation was composed by sand and gravel colluvium. A few days prior the flowslide, warm weather could have caused the melting of the snow cover and just before the propagation flow some crack appeared on the waste dump. The propagation mechanism described by (Dawson et al., 1998) dwells on the presence of a fine-grained layer which underwent liquefaction and the wast debris flow above this layer. This hypothesis is deduced from the finding of the fine layer in the deposition zone. Numerical simulations of the Greenhills Cougar 7 flowslide, using different approaches, can be found in (Pastor et al., 2014; Quecedo et al., 2004) and (Herrores et al., 2002).

The original data of the sliding surface is shown in figure 7.4(a), from which the set of nodes of figure 7.4(b) has been generated.

Material parametes, as provided in (Dawson et al., 1998), are: density $\rho =$ 1900 Kg/m^3, friction angle $\varphi = 37°$ and basal friction angle $\varphi_{basal} = 32°$. Material parameters used in the numerical analysis, are shown in table 7.1.

The difference between the physical and the numerical parameters, in particular the smaller friction angle used in the simulation, can been explained considering that in the presented model, the liquefaction process can not be modelled. In the analysis, the following numerical parameters have been used: $\Delta t = 0.005$

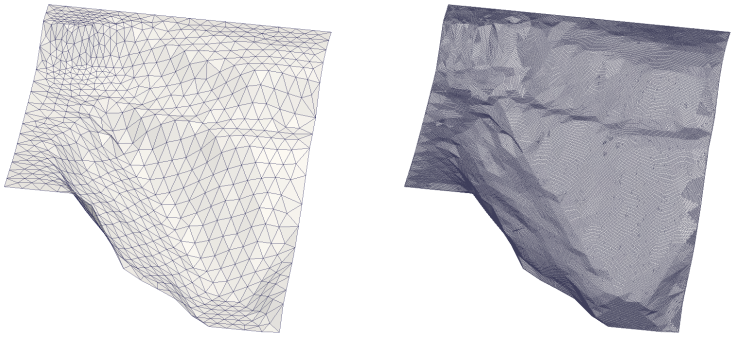

(a) (b)

Figure 7.4: Sliding surfaces of Greenhills Cougar 7 dump. Original data (a) and the set of points used for the numerical simulation (b).

		material parameters		
h_{slip} (m)	μ (Pa s)	ϕ	ϕ_{basal}	ρ (kg/m^3)
2	0.1	32°	32°	1900

Table 7.1: Cougar Hill: material parameter.

s, $N = 1000$, $\alpha = 1.8$ and $\frac{1}{\varepsilon} = 10^7$, where N is the parameter of the regularized apparent viscosity (section 3.5.2), α is the parameter used in the alpha-shape algorithm (section 4.6.2) and $\frac{1}{\varepsilon}$ is the penalization term to prevent normal velocity at the slip boundary (section 5.6). The geometry of the problem has been provided by the department of Applied Mathematics in Civil Engineering at the Polytechnical University of Madrid. Mesh and time information are shown in table 7.2 and 7.3, respectively.

The presented simulation have been used as first test on large scale simulation. Material parameters, and in particular viscosity and slip height, have been calibrated performing different attempts. Even if the comparison with the experimental observation is qualitative, figure 7.5, it can be observed that the presented model works well on irregular topography and is able to capture the

mesh		
h^e (m)	nodes	tetrahedra
5	106046	104360

Table 7.2: Cougar Hill: mesh information, h^e is the reference mesh size. The number of tetrahedra is the one at the first time step.

time		
physical	computational	volume (m^3)
110 s	14 hours	2 10^5

Table 7.3: Time information and mobilized terrain volume of the Cougar Hill landslide.

propagation mechanism.

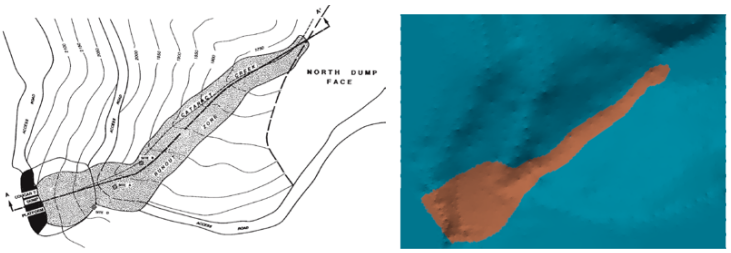

Figure 7.5: Comparison between experimental observation and simulation of the final deposit

Figure 7.6 and 7.7 show snapshots of the numerical simulation at different instants, in the second one the velocity magnitude is plotted.

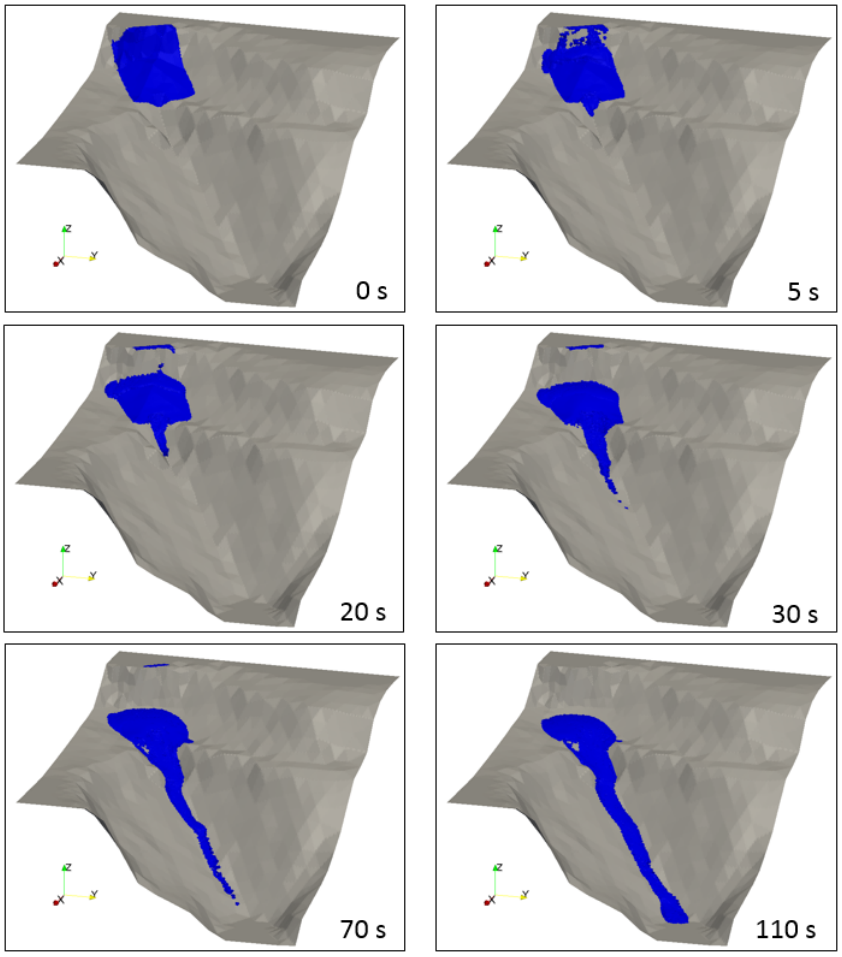

Figure 7.6: Cougar Hill: Cougar dump 7 failure. Position of nodes at different instants

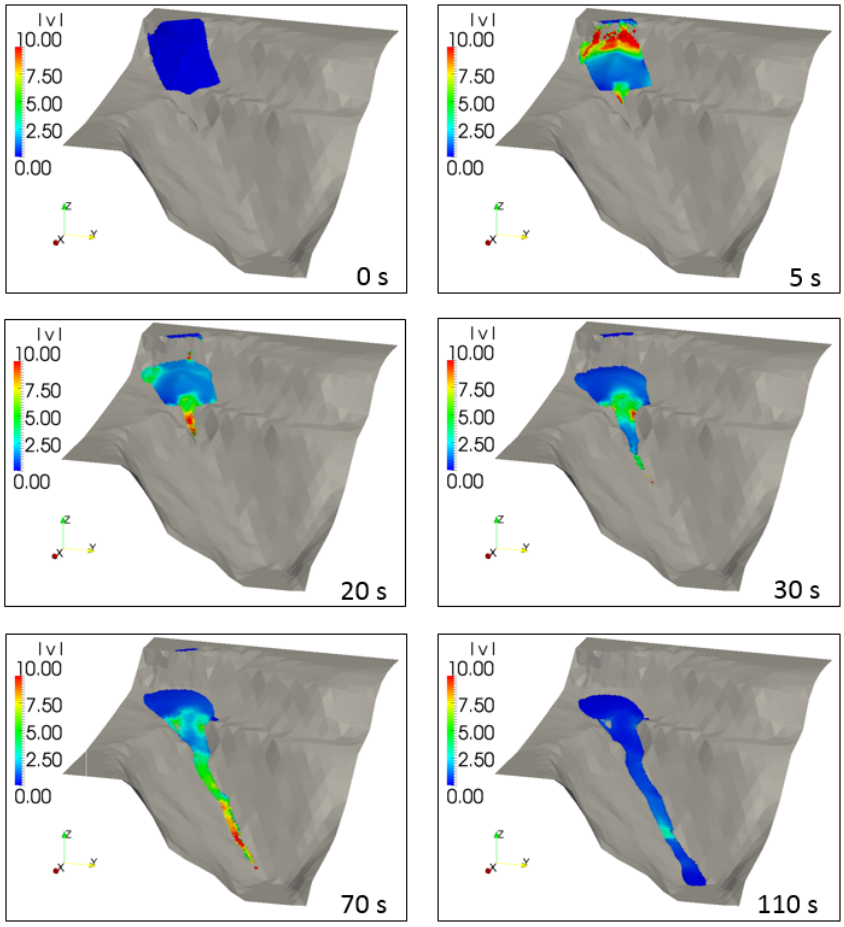

Figure 7.7: Cougar Hill: Cougar dump 7 failure. Contours of velocity magnitude at different instants.

7.3 Frank rock avalanche

Frank slide (Canada, 1903) is considered as one of the most severe tragedies in Canada with a loss of approximately 70 lives. It involved more than 30 million of cubic meters of limestone rock detached from the ridge of Turtle Mountain, in the Northwest Territories. The landslide, with a 700 m wide front, descended along a 800 m slope creating a deposit 1.7 km wide and almost 2 km long. The deposit was approximately 18 m thick and the estimated duration of the event was of less than 100 s. A detailed description of the event can be found in (Cruden and Hungr, 1986; Wang and Sassa, 2010a). A view of the final deposit is shown in Figure 7.9. The track followed by the running landslide is also clearly visible in the picture.

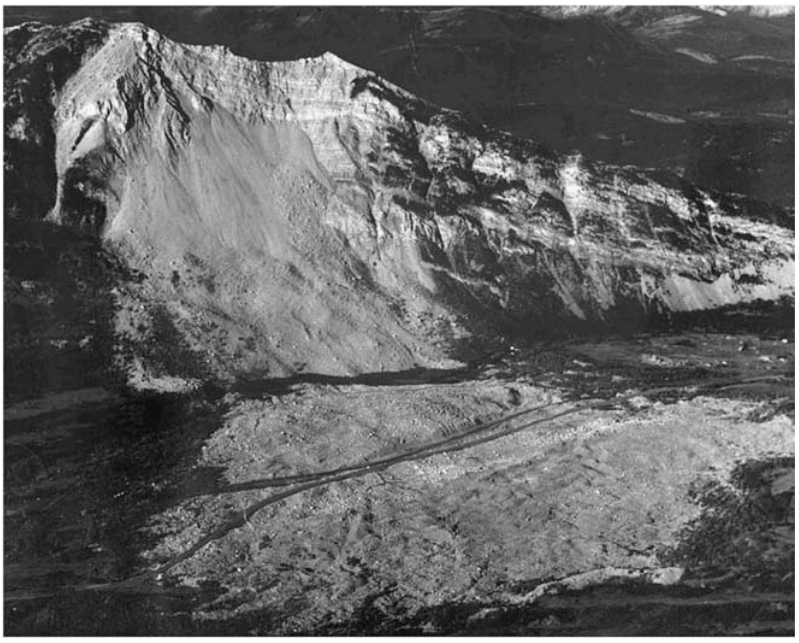

Figure 7.8: Frank rock avalanche. View of the final deposit (Wang and Sassa, 2010a).

Material properties are as in (Pastor et al., 2015): density $\rho = 1800$ Kg/m^3, internal friction angle $\varphi = 12.4°$, viscosity $\mu = 0.01$ Pa s. A basal friction angle $\varphi_{basal} = \varphi = 12.4°$ has also been assumed (table 7.4). Three different values of the slip height have been considered: $h_{slip} = 0$ m, 20 m, 50 m. The used initial mesh consists of 194795 tetrahedra, with 191028 nodes and an average mesh size $h^e = 10$ m (table 7.5).

Snapshots of the landslide runout are shown in Figure 7.10 at time instants $t = 0$ s, 14 s, 31 s, 71 s. The last snapshot shows the configuration of the final deposit and the corresponding time of 71 s compares well with the duration of less than 100 s reported by witnesses and with the propagation time of 80 s estimated in (Pastor et al., 2015). The profile of the final deposit is shown in Figure 7.11 for the different values of h_{slip}. Also in this case, the no-slip condition $h_{slip} = 0$ leads to an underestimation of the runout distance, while better accuracy is achieved with the largest value $h_{slip} = 50$ m, with a ratio $h_{slip}/h^e = 5$. This large value of h_{slip} can be explained with the very large (compared to the previous laboratory tests) average mesh size used in this case ($h^e = 10$ m). In fact, the slip condition directly affects an amount of flowing material which is of the order of magnitude of the mass in the elements in contact with the basal interface.

material parameters		
ϕ	ϕ_{basal}	ρ (kg/m^3)
12.4°	12.4°	1800

Table 7.4: Frank avalanche: material parameter.

Figure 7.9: Frank rock avalanche. View of the final deposit.

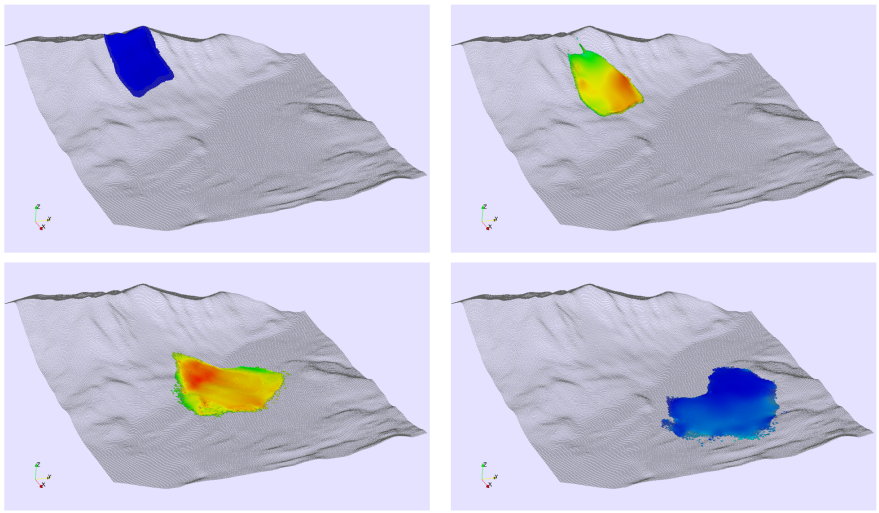

Figure 7.10: Frank rock avalanche. Snapshots at time instants $t = 0$ s, 14 s, 31 s, 71 s (from left to right, from top to bottom, respectively), with $h_{slip} = 50$ m.

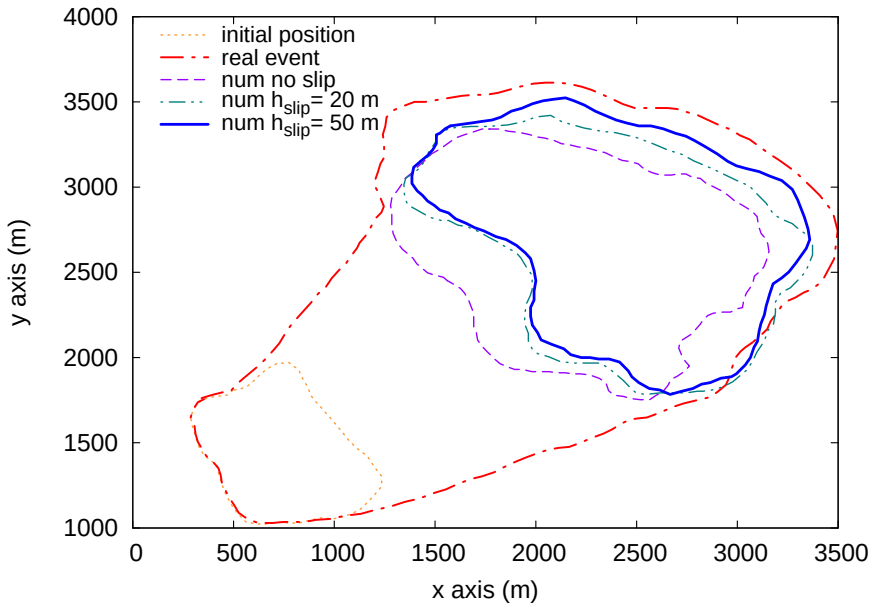

Figure 7.11: Frank rock avalanche. Landslide track and final deposit at $t = 71$ s. Comparison between experimental observation and simulation with different slip lengths: $h_{slip} = 0$ m, 5 m, 20 m, 50 m.

mesh		
h^e (m)	nodes	tetrahedra
10	194795	191028

Table 7.5: Mesh information for the presented simulations, where h^e is the mesh size. The number of tetrahedra is relative to the first time step.

time		
physical	computational	volume (m^3)
80 s	19 hours	30 10^6

Table 7.6: Time information and mobilized terrain volume of the Frank avalanche.

7.4 Vajont Slide

The Vajont valley is located in the western part of Friuli Venezia Giulia region, Italy, between the towns of Erto and Casso and it extends to the left bank of Piave valley near the city of Longarone. The topographic boundaries of the Vajont valley are the S. Osvaldo pass on the east, the Tòc mount on the south, the dam on the west and the mount Borga on the north. The valley is east-west oriented, formed as a result of the erosion of an ancient glacial, with two main waterways which are the Vajont stream, which gives the name to the valley, and its major tributary, the stream Mesazzo (figure 7.12).

Figure 7.12: Aerial view of the Vajont valley

The reservoir was finalized to electric energy production through Vajont stream water usage. The doubly arched dam was constructed between 1957 and 1959. The 276 meters high dam had a maximum level of water storage equal to 722.5 m a.s.l. and a volume of $169 \cdot 10^6\ m^3$.

The 9^{th} October 1963 approximately 270 million cubic meter of rock slid from the mount Toc, generating a huge impulsive wave which overtopped the dam destroying the town of Longarone and other towns on its path. In the years

Figure 7.13: Aerial view of the Vajont valley after the slide of 1960

Figure 7.14: Aerial view of the Vajont valley after the catastrophic slide of 1963

Figure 7.15: View of the mount Toc in the present days, with vegetation on the surface of the slide.

preceding the catastrophic event, there were two important warning signs: the landslide on the close reservoir of Pontisei in March 1959 and the landslides of November 1960 in the same Vajont reservoir from the plain della Pozza with 700.000 cubic meters of mobilized terrain (figure 7.13). These signs were underestimated and the lowering of the water level in the reservoir, up to 700 meters, was considered a sufficient measure to mitigate hazards.

The landslide of 1963 had a catastrophic and unexpected effect. The landslide mass moved laterally and upwards on the opposite valley flank and rapidly displaced the water in the reservoir which reached over the dam. The village of Casso, in the opposite bank of the lake, was not damaged and only water spray and some stones of medium dimension hit the village. Due to the irregular terrain topography the water did not reach the same level around the reservoir. In the Piave valley, the effects were much more destructive: the villages of Longarone, Pirago, Villanova, Rivalta, Faè and Codissago were destroyed. Over 2000 people were killed and it is considered the most disastrous landslide that occurred in the

XX century. An aerial view of the Vajont valley after the landslide is shown in figure 7.14 and a view of the mount Toc in present days is shown in figure 7.15.

In the analysis, the following numerical parameters have been used: $\Delta t = 0.01$ s, $N = 100$, $\alpha = 1.9$ and $\frac{1}{\varepsilon} = 10^7$, where N is the parameter of the regularized apparent viscosity (section 3.5.2), α is the parameter used in the alpha-shape algorithm (section 4.6.2) and $\frac{1}{\varepsilon}$ is the penalization term to prevent normal velocity at the slip boundary (section 5.6). Material parameters for the numerical simulation are provided in (Semenza, 2001; Genevois and Ghirotti, 2005; Crosta et al., 2007) and are summarized in table 7.7. In figure 7.16 the contours of the velocity

		material parameters		
material	geometry	ϕ	ϕ_{basal}	ρ (kg/m^3)
terrain	fig. 7.18 brown	26°	5°	2400
water	fig. 7.18 blue			1000

Table 7.7: Vajont slide: material parameter.

magnitude plotted on a vertical plane of the moving terrain are shown for two different values of h_{slip}. The very high value of the slip parameter h_{slip} is justified

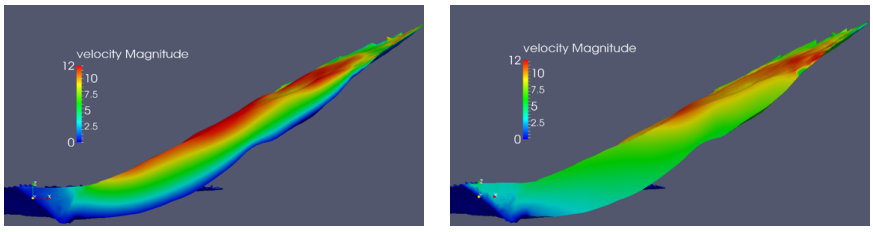

(a) (b)

Figure 7.16: Terrain velocity profile in a section: $h_{slip} = 5$ m (a) and $h_{slip} = 1000$ (b)

considering that the prevalent movement was of translational type along a well defined surface of rupture. Hence, for the terrain material a viscosity of $\mu = 0.1$

Pa s and a slip height of $h_{slip} = 1000$ m have been considered. Water viscosity has been set equal to $\mu = 0.001$ Pa s. To avoid irregularities in the pressure field between the water and the terrain (figure 7.17, on the nodes on the boundary slip conditions have been imposed even for water with a value of $h_{slip} = 1$ m. The input data that define the geometry of the problem, were provided by the

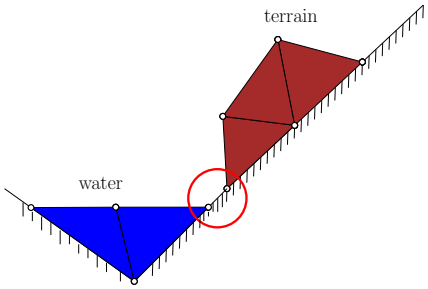

Figure 7.17: 2D representation of terrain and water elements. If water has no slip at the boundary interface (highlighted nodes) high pressure is generated.

department of Environmental Sciences at the University of Milano-Bicocca. The considered area for the simulation is about 3×4 km^2. Figure 7.18 shows the discretized geometry of the problem. An initial mesh of 273695 tetrahedra with 78137 nodes has been used with an average element size of $h^e = 20$ m (table 7.8). Snapshots of the numerical simulation at different time instants are presented in

mesh		
h^e (m)	nodes	tetrahedra
20	78137	273695

Table 7.8: Mesh information for the presented simulations, where h^e is the mesh size. The number of tetrahedra is relative to the first time step.

figure 7.19. Figure 7.20 shows the contour of the wave height on the opposite bank of the mount Toc. The comparison between the in situ observation (the wave eroded trees and soil on the northern side of the Vajont valley) and the

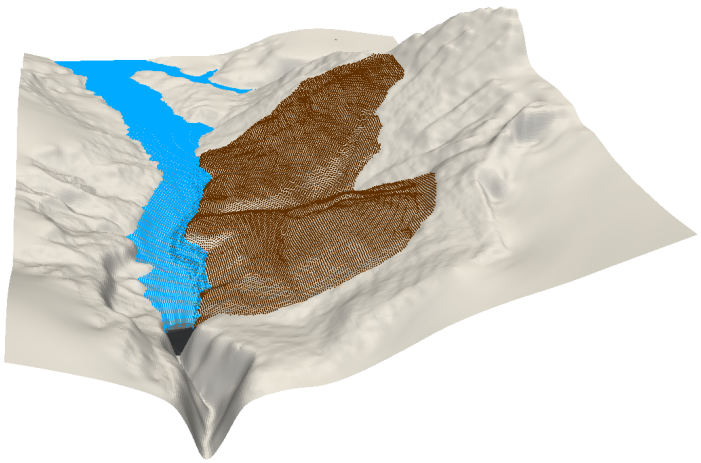

Figure 7.18: Complete geometry of the Vajont slide.

numerical results shows a good agreements. Not a successful accordance is found only in the center of the bank, where the slope is very steep and the size of the tetrahedral elements are too big to capture the correct water propagation. In table 7.9 time and volume information of the Vajont landslide simulation are shown.

time		
physical	computational	volume (m^3)
70 s	34 hours	270 10^6

Table 7.9: Time information and mobilized terrain volume of the Vajont landslide.

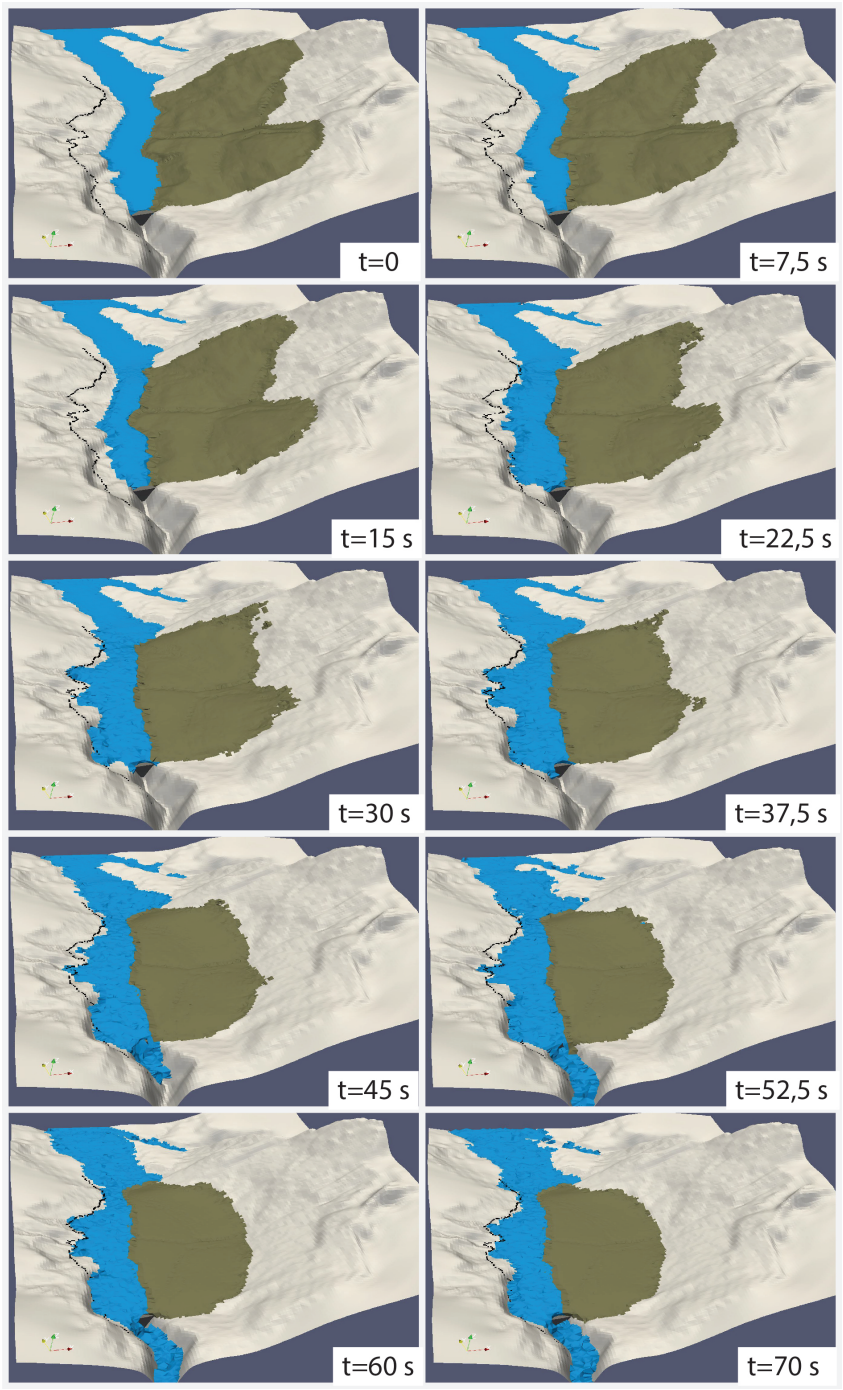

Figure 7.19: Numerical simulation of the Vajont slide. Snapshots at different instants.

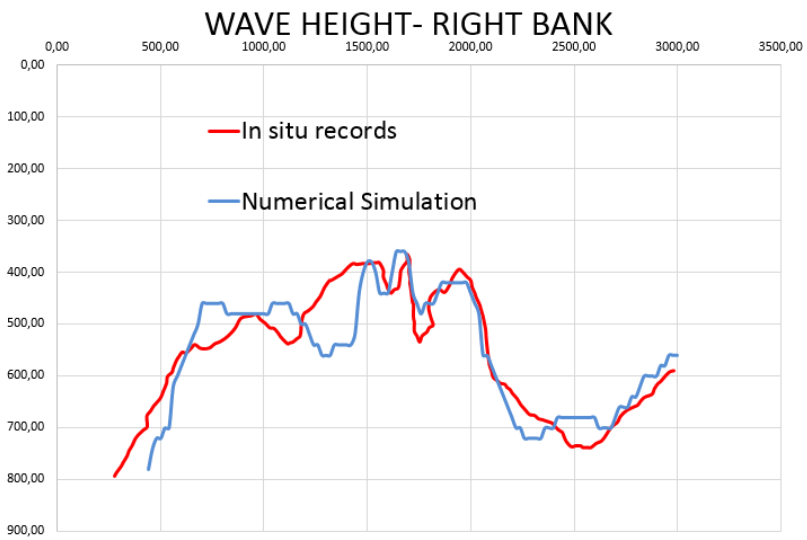

Figure 7.20: Profile of the wave height, comparison between numerical (blue) and in situ records (red)

8 Conclusions

This work has been devoted to the development of a three-dimensional numerical tool for the analysis of landslides runouts. To this purpose, a Lagrangian Finite Element Method, based on the so called Particle Finite Element Method (PFEM), first proposed by Oñate, Idelsohn and coworkes, has been developed. The main results achived can be summarized as follows.

- Landslide runouts involve extremely large deformations of the moving soil mass. For this reason, in the literature they have been modelled mainly by considering the soil as a viscous fluid. This assumption implies that the initial, statically equilibrated state cannot be included in the model and the transition from stable slope configuration to an unstable moving landslide cannot be described. In this work, the moving mass is modeled as a rigid-viscoplastic solid undergoing large deformations. This implies that also in this case only the landslide motion can be described. The assumed rigid-viscoplastic behavior is obtained by simply neglecting the elastic part of the

behavior of an elastic-viscoplastic material model. In contrast, the modeling of the soil evolution from its initially stable equilibrium configuration to the final unstable state of running landslide will require consideration of the complete elasto-viscoplastic material behavior. The kinematic and the material model have been described in chapter 3.

- For the viscous fluid, normally adopted in the simulations of fast propagating landslides, the standard boundary conditions enforce zero relative slip between the fluid and the containing wall. These conditions are physically motivated for fluids, but have been shown to loose validity when the flowing material has a granular structure, in particular for increasing grain size. In the present work, the soil material has been modeled as a rigid-viscoplastic, non-dilatant, Drucker-Prager material and specific slip conditions have been defined to model the interaction between the flowing mass and the basal surface (chapter 5). The new slip conditions are of Navier type, i.e. the resisting tangential force is proportional to the slip velocity. A pressure sensitive threshold has also been introduced, so that the slip can occur only when the tangential stress exceeds the current limit value. The proposed interface law is characterized by two parameters: the slip height h_{slip} and the basal friction angle φ_{basal}.

- The new boundary conditions require a special treatment to fit into the PFEM framework in view of the special role of the nodes on the basal surface, which are used to define the geometry of the computational domain and therefore cannot move. Finite elements having at least a node onto the basal surface are defined to have a mixed Lagrangian-Eulerian nature: nodes on the boundary are Eulerian, i.e. their velocity is set to zero and a convective term is added to the balance equation; interior nodes are Lagrangian, i.e. they move with the material velocity and the corresponding convective term is zero. Slip boundary conditions need to be supplemented with no-flux conditions, stating that the soil material cannot interpenetrate

the basal surface. These no-flux conditions are known to lead to inconsistencies when the surface is not smooth, due to ambiguity in the definition of the normal. The problem has been circumvented by relaxing the no-flux condition using a penalty approach.

- The importance of the slip conditions has been assessed by simulating laboratory tests (chapter 6). In all cases, a proper definition of the slip parameters has allowed for a significant accuracy gain in the prediction of the runout distance and of the shape of the final deposit. The proposed numerical model has finally been applied to the simulation of a real large scale landslides (chapter 7) obtaining good accuracy in the prediction of the final deposit. Some modification to the continuous re-triangulation strategy has been realized in order to reduce the computation time (chapter 7).

The numerical tool has been implemented by the author using the FORTRAN 90 programming language, with the exceptions of the PARDISO solver used for the solution of the linear system and the public domain tool TETGEN used to create the Delaunay triangulation.

Future developments

The present work could be improved under several points of view. Some possible new developments are listed below.

- In chapter 5 the present approach has been formulated using a nodal integration. 2D tests using Newtonian fluids show a good agreement in comparison with the standard elemental integration while considering the rigid viscoplastic model, spurious oscillations appear in the pressure field. It would be of interest to consider others stabilization techniques, for example the direct pressure stabilization, to improve the results. In view of a future parallel implementation of the code, it is interesting to note that in this

case, the matrices assembly can be performed with a loop on nodes instead of on elements. Furthermore, historic variables for more complex plastic laws, can be defined and stored in the integration points (nodes). This approach can be easily implemented also in the 3D case.

- Other constitutive laws can be implemented to allow the model to describe different cases from more fluid-like landslides to the slide or fall of rigid solids and more realistic constitutive law for landslide material can be investigated, allowing for initial equilibrium and instability triggering.

- Further validations on real landslides should be performed. To speed-up calculation to allow for practical engineering applications a parallelization of the code should be investigated.

Bibliography

Aleotti, P. and Chowdhury, R. (1999). Landslide hazard assessment: summary review and new perspectives. *Bulletin of Engineering Geology and the Environment*, 58(1):21–44.

Andersen, S. and Andersen, L. (2010). Modelling of landslides with the material-point method. *Computational Geosciences*, 14(1):137–147.

Anderson, R. S. and Anderson, S. P. (2010). *Geomorphology: the mechanics and chemistry of landscapes*. Cambridge University Press.

Aubry, R., Idelsohn, S. R., and Oñate, E. (2005). Particle finite element method in fluid-mechanics including thermal convection-diffusion. *Computers and Structures*, 83(17-18):1459–1475.

Aubry, R., Idelsohn, S. R., and Oñate, E. (2006). Fractional step like schemes for free surface problems with thermal coupling using the lagrangian PFEM. *Computational Mechanics*, 38(4-5):294–309.

Azanza, E., Chevoir, F., and Moucheront, P. (1999). Experimental study of collisional granular flows down an inclined plane. *Journal of Fluid Mechanics*, 400:199–227.

Balestra, M., Hughes, T. J. R., and Franca, L. P. (1986). A new finite element formulation for computational fluid dynamics: V. Circumventing the babuška-brezzi condition: a stable Petrov-Galerkin formulation of the stokes problem

accommodating equal-order interpolations. *Computer Methods in Applied Mechanics and Engineering*, 59(1):85–99.

Barbolini, M., Biancardi, A., Natale, L., and Pagliardi, M. (2005). A low cost system for the estimation of concentration and velocity profiles in rapid dry granular flows. *Cold Regions Science and Technology*, 43(1-2):49–61.

Bartelt, P., Buser, O., and Platzer, K. (2007). Starving avalanches: Frictional mechanisms at the tails of finite-sized mass movements. *Geophysical Research Letters*, 34(20):1–6.

Becker, P., Idelsohn, S. R., and Oñate, E. (2015). A unified monolithic approach for multi-fluid flows and fluid–structure interaction using the Particle Finite Element Method with fixed mesh. *Computational Mechanics*, 55(6):1091–1104.

Beguería, S., Van Asch, T. W. J., Malet, J.-P., and Gröndahl, S. (2009). A GIS-based numerical model for simulating the kinematics of mud and debris flows over complex terrain. *Natural Hazards and Earth System Science*, 9:1897–1909.

Behr, M. (2004). On the application of slip boundary condition on curved boundaries. *International Journal for Numerical Methods in Fluids*, 45(1):43–51.

Berger, M. J., George, D. L., LeVeque, R. J., and Mandli, K. T. (2011). The GeoClaw software for depth-averaged flows with adaptive refinement. *Advances in Water Resources*, 34(9):1195–1206.

Brezzi, F. and Fortin, M. (1991). *Mixed and Hibrid Finite Element Method.* Springer-Verlag.

Brooks, A. N. and Hughes, T. J. R. (1982). Streamline upwind/Petrov-Galerkin formulations for convection dominated flows with particular emphasis on the incompressible Navier-Stokes equations. *Computer methods in applied mechanics and engineering*, 32(1):199–259.

Brunetti, M. T., Guzzetti, F., Cardinali, M., Fiorucci, F., Santangelo, M., Mancinelli, P., Komatsu, G., and Borselli, L. (2014). Analysis of a new geomorphological inventory of landslides in Valles Marineris, Mars. *Earth and Planetary Science Letters*, 405:156–168.

Calvetti, F., Crosta, G., and Tatarella, M. (2000). Numerical simulation of dry granular flows: from the reproduction of small-scale experiments to the prediction of rock avalanches. *Rivista Italiana di Geotecnica*, 2:21–38.

Cascini, L., Cuomo, S., and Guida, D. (2008). Typical source areas of May 1998 flow-like mass movements in the Campania region, Southern Italy. *Engineering Geology*, 96(3-4):107–125.

Castellazzi, G., Artioli, E., and Krysl, P. (2015). Linear tetrahedral element for problems of plastic deformation. *Meccanica*, 50(12):3069–3086.

Cecinato, F., Zervos, A., and Veveakis, E. (2011). A thermo-mechanical model for the catastrophic collapse of large landslides. *International Journal for Numerical and Analytical Methods in Geomechanics*, 35(14):1507–1535.

Chen, H. and Lee, C. F. (2003). A dynamic model for rainfall-induced landslides on natural slopes. *Geomorphology*, 51(4):269–288.

Chorin, A. J. (1967). A numerical method for solving incompressible viscous flow problems. *Journal of Computational Physics*, 2(1):12–26.

Codina, R. (2001). Pressure Stability in Fractional Step Finite Element Methods for Incompressible Flows. *Journal of Computational Physics*, 170(1):112–140.

Cremonesi, M., Frangi, A., and Perego, U. (2010). A Lagrangian finite element approach for the analysis of fluid–structure interaction problems. *International Journal for Numerical Methods in Engineering*, 84:610–630.

Cremonesi, M., Frangi, a., and Perego, U. (2011). A Lagrangian finite element approach for the simulation of water-waves induced by landslides. *Computers & Structures*, 89(11-12):1086–1093.

Cremonesi, M. and Perego, U. (2013). Numerical simulation of landslide-reservoir interaction using a PFEM approach. In *Particle-Based Methods III: Fundamentals and Applications - Proceedings of the 3rd International Conference on Particle-based MethodsFundamentals and Applications, Particles 2013*, pages 408–417.

Crosta, G., Blasio, F. D., Caro, M. D., Volpi, G., Imposimato, S., and Roddeman, S. (2014). Model of collapse and propagation of a granular mass onto a erodible substrate. *submitted for the pubblication.*

Crosta, G., Frattini, P., Imposimato, S., and Roddeman, D. (2007). 2D and 3D numerical modeling of long runout landslides - the Vajont case study. In *Landslides: from mapping to loss and risk astimation*, pages 15–24. IUSS Press, Pavia.

Crosta, G., Imposimato, S., and Roddeman, D. (2009). Numerical modelling of entrainment/deposition in rock and debris-avalanches. *Engineering Geology*, 109(1-2):135–145.

Cruden, D. M. (1991). A simple definition of a landslide. *Bulletin of the International Association of Engineering Geology - Bulletin de l'Association Internationale de Géologie de l'Ingénieur*, 43(1):27–29.

Cruden, D. M. and Hungr, O. (1986). The debris of the Frank Slide and theories of rockslide-avalanche mobility. *Canadian Journal of Earth Sciences*, 23(3):425–432.

Cruden, D. M. and Varnes, D. J. (1996). Landslides: investigation and mitigation. Chapter 3-Landslide types and processes. Technical Report 247.

Dawson, R. F., Morgenstern, N. R., and Stokes, a. W. (1998). Liquefaction flowslides in Rocky Mountain coal mine waste dumps. *Canadian Geotechnical Journal*, 35(2):328–343.

De Borst, R., Crisfield, M. A., Remmers, J. J. C., and Verhoosel, C. V. (2012). *Nonlinear finite element analysis of solids and structures*. John Wiley & Sons.

de Gennes, P. (1999). Granular matter: a tentative view. *Reviews of Modern Physics*, 71(2):S374–S382.

Del Prete, M., Guadagno, F. M., and Hawkins, a. B. (1998). Preliminary report on the landslides of 5 May 1998, Campania, southern Italy. *Bulletin of Engineering Geology and the Environment*, 57(2):113.

Denn, M. M. (2001). Extrusion instabilities and wall slip. *Annual Review of Fluid Mechanics*, 33:265–287.

Dione, I., Tibirna, C., and Urquiza, J. (2013). Stokes equations with penalised slip boundary conditions. *International Journal of Computational Fluid Dynamics*, 27(6-7):283–296.

Dione, I. and Urquiza, J. M. (2015). Penalty: finite element approximation of Stokes equations with slip boundary conditions. *Numerische Mathematik*, 129(3):587–610.

Donea, J. and Huerta, A. (2003). *Finite Element Methods for Flow Problems*. John Wiley & Sons, Ltd, Chichester, UK.

Edelsbrunner, H. and Mücke, E. P. (1994). Three-dimensional alpha shapes. *ACM Transactions on Graphics (TOG)*, 13(1):43–72.

Engelman, M. S., Sani, R. L., Gresho, P. M., and Liuemore, L. (1982). The implementation of normal and/or tangential boundary conditions in finite element codes for incompressible fluid flow. *International Journal for Numerical Methods in Fluids*, 2(3):225–238.

Ferrás, L., Nóbrega, J., and Pinho, F. (2012). Analytical solutions for Newtonian and inelastic non-Newtonian flows with wall slip. *Journal of Non-Newtonian Fluid Mechanics*, 175-176:76–88.

Forterre, Y. and Pouliquen, O. (2008). Flows of Dense Granular Media. *Annual Review of Fluid Mechanics*, 40(1):1–24.

Fortin, A., Côté, D., and Tanguy, P. (1991). On the imposition of friction boundary conditions for the numerical simulation of Bingham fluid flows. *Computer Methods in Applied Mechanics and Engineering*, 88(1):97–109.

Fritz, H. M., Mohammed, F., and Yoo, J. (2009). Lituya bay landslide impact generated mega-tsunami 50th anniversary. *Pure and Applied Geophysics*, 166(1-2):153–175.

Genevois, R. and Ghirotti, M. (2005). The 1963 vaiont landslide. *Giornale di Geologia Applicata*, 1(1):41–52.

Gray, J. M. N. T., Wieland, M., and Hutter, K. (1999). Gravity-driven free surface flow of granular avalanches over complex basal topography. *Proceedings of the Royal Society A: Mathematical, Physical and Engineering Sciences*, 455(1985):1841–1874.

Guermond, J. L., Minev, P., and Shen, J. (2006). An overview of projection methods for incompressible flows. *Computer Methods in Applied Mechanics and Engineering*, 195(44-47):6011–6045.

Habib, P. (1976). Production of gaseous pore pressure during rock slides. *Rock Mechanics*, 7:193–197.

Herrores, M. I., FernÁndez Merodo, J. a., Quecedo, M., Mira, P., Pastor, M., and GonzÁlez, E. (2002). Modelling tailings dams and mine waste dumps failures. *Géotechnique*, 52(8):579–591.

Highland, L. and Bobrowsky, P. (2008). The landslide handbook—A guide to understanding landslides: Reston, Virginia. *US Geological Survey Circular*.

Hirt, C. and Nichols, B. (1981). Volume of fluid (VOF) method for the dynamics of free boundaries. *Journal of Computational Physics*, 39(1):201–225.

Hirt, C. W., Nichols, B. D., and Romero, N. C. (1975). SOLA: A numerical solution algorithm for transient fluid flows. *NASA STI/Recon Technical Report N*, 75:32418.

Holzapfel, G. A. (2000). *Nonlinear solid mechanics*, volume 24. Wiley Chichester.

Hungr, O., Evans, S. G., Bovis, M. J., and Hutchinson, J. N. (2001). A Review of the Classification of Landslides of the Flow Type. *Environmental & Engineering Geoscience*, VII:221–238.

Hutter, K. and Koch, T. (1991). Motion of a granular avalanche in an exponentially curved chute: Experiments and theoretical predictions. *Philosophical Transactions of the Royal Society of London*, 334(1633):93–138.

Hutter, K., Koch, T., Plüss, C., and Savage, S. B. (1995). The Dynamics of Avalanches of Granular-Materials from Initiation to Runout .2. Experiments. *Acta Mechanica*, 109:127–165.

Idelsohn, S., Oñate, E., and Del Pin, F. (2003). A Lagrangian meshless finite element method applied to fluid–structure interaction problems. *Computers & Structures*, 81(8-11):655–671.

Idelsohn, S., Oñate, E., and Pin, F. D. (2004). The particle finite element method: a powerful tool to solve incompressible flows with free-surfaces and breaking waves. *International Journal for Numerical Methods in Engineering*, 61(7):964–989.

Idelsohn, S. R., Marti, J., Limache, A., and Oñate, E. (2008). Unified Lagrangian formulation for elastic solids and incompressible fluids: Application to fluid-

structure interaction problems via the PFEM. *Computer Methods in Applied Mechanics and Engineering*, 197:1762–1776.

Idelsohn, S. R. and Oñate, E. (2006). To mesh or not to mesh. That is the question... *Computer Methods in Applied Mechanics and Engineering*, 195(37-40):4681–4696.

Idelsohn, S. R., Oñate, E., Pin, F. D., and Calvo, N. (2006). Fluid–structure interaction using the particle finite element method. *Computer Methods in Applied Mechanics and Engineering*, 195(17-18):2100–2123.

Iverson, R. M., Logan, M., and Denlinger, R. P. (2004). Granular avalanches across irregular three-dimensional terrain: 2. Experimental tests. *J. Geophys Res.*, 109(FI).

Kilburn, C. R. J. and Petley, D. N. (2003). Forecasting giant, catastrophic slope collapse: Lessons from Vajont, Northern Italy. *Geomorphology*, 54(1-2):21–32.

Knill, S. J. (2006). Report on the Fei Tsui Road landslide of 13 August 1995. Technical report.

Krysl, P. and Zhu, B. (2008). Locking-free continuum displacement finite elements with nodal integration. *International Journal for Numerical Methods in Engineering*, 76(7):1020–1043.

Kuzmin, A., Luisier, M., and Schenk, O. (2013). Fast methods for computing selected elements of the Green's function in massively parallel nanoelectronic device simulations. *Lecture Notes in Computer Science (including subseries Lecture Notes in Artificial Intelligence and Lecture Notes in Bioinformatics)*, 8097 LNCS:533–544.

Lagrée, P.-Y., Staron, L., and Popinet, S. (2011). The granular column collapse as a continuum: validity of a two-dimensional Navier–Stokes model with a μ(I)-rheology. *Journal of Fluid Mechanics*, 686:378–408.

Larese, A. (2012). *A coupled Eulerian-PFEM model for the simulation of overtopping in rockfill dams*. Universitat Politècnica de Catalunya (UPC Barcelona Tech).

Larese, a., Rossi, R., Oñate, E., and Idelsohn, S. (2008). Validation of the particle finite element method (PFEM) for simulation of free surface flows. *Engineering Computations*, 25(4):385–425.

Larese, A., Rossi, R., Oñate, E., and Idelsohn, S. R. (2012). A coupled PFEM-Eulerian approach for the solution of porous FSI problems. *Computational Mechanics*, 50(6):805–819.

Larese, A., Rossi, R., Oñate, E., Toledo, M. Á., Morán, R., and Campos, H. (2013). Numerical and Experimental Study of Overtopping and Failure of Rock fill Dams. *International Journal of Geomechanics*, 15(8):1–23.

Lu, C.-Y., Tang, C.-L., Chan, Y.-C., Hu, J.-C., and Chi, C.-C. (2014). Forecasting landslide hazard by the 3D discrete element method: A case study of the unstable slope in the Lushan hot spring district, central Taiwan. *Engineering Geology*, 183:14–30.

Lubarda, V. A. (2004). Constitutive theories based on the multiplicative decomposition of deformation gradient: Thermoelasticity, elastoplasticity, and biomechanics. *Applied Mechanics Reviews*, 57(2):95.

Lucas, A., Mangeney, A., and Ampuero, J. P. (2014). Frictional velocity-weakening in landslides on Earth and on other planetary bodies. *Nature communications*, 5:3417.

Lun, C. K. K., Savage, S. B., Jeffrey, D. J., and Chepurniy, N. (1984). Kinetic theories for granular flow: inelastic particles in Couette flow and slightly inelastic particles in a general flowfield. *Journal of Fluid Mechanics*, 140(-1):223.

Malin, M. C. (1992). Mass movements on Venus - Preliminary results from Magellan cycle 1 observations. pages 1–15.

Manzella, I. (2008). *Dry rock avalanche propagation: Unconstrained flow experiments with granular materials and blocks at small scale*. PhD thesis.

Manzella, I. and Labiouse, V. (2009). Flow experiments with gravel and blocks at small scale to investigate parameters and mechanisms involved in rock avalanches. *Engineering Geology*, 109(1-2):146–158.

Manzella, I. and Labiouse, V. (2013). Empirical and analytical analyses of laboratory granular flows to investigate rock avalanche propagation. *Landslides*, 10(1):23–36.

Marsden, J. E. and Hughes, T. J. R. (1994). *Mathematical foundations of elasticity*. Courier Corporation.

Martelloni, G., Bagnoli, F., and Massaro, E. (2013). A computational toy model for shallow landslides: Molecular dynamics approach. *Communications in Nonlinear Science and Numerical Simulation*, 18(9):2479–2492.

McConnell, R. G. and Brock, R. W. (1904). Report on the Great Landslide at Frank, Alta. 1903.

McDougall, S. and Hungr, O. (2004). A model for the analysis of rapid landslide motion across three-dimensional terrain. *Canadian Geotechnical Journal*, 41(6):1084–1097.

Miller, D. (1960). Giant waves in Lituya Bay, Alaska. Technical report, U.S. Government Printing Office, Washington D.C.

Morgenstern, N. R. and Martin, C. D. (2008). Landslides : Seeing the ground. *Landslides and Engineered Slopes*, pages 3–23.

Moriguchi, S., Borja, R. I., Yashima, A., and Sawada, K. (2009). Estimating the impact force generated by granular flow on a rigid obstruction. *Acta Geotechnica*, 4(1):57–71.

Ogden, R. W. (1997). *Non-linear elastic deformations*. Dover Publications 1997 and Ellis Horwood 1984.

Oñate, E., Celigueta, M. a., and Idelsohn, S. R. (2006). Modeling bed erosion in free surface flows by the particle finite element method. *Acta Geotechnica*, 1:237–252.

Oñate, E., Celigueta, M. A., Idelsohn, S. R., Salazar, F., and Suárez, B. (2011). Possibilities of the particle finite element method for fluid-soil-structure interaction problems. *Computational Mechanics*, 48(3):307–318.

Onate, E., Edelshon, S. R., Del Pin, F., and Aubry, R. (2004). The particle finite element method. An overview. *International Journal of Computational Methods*, 01(02):267–307.

Oñate, E., Franci, A., Carbonell, J. M., Tezduyar, T. E., Sathe, S., Schwaab, M., and Conklin, B. S. (2014). Lagrangian formulation for finite element analysis of quasi-incompressible fluids with reduced mass losses. *International Journal for Numerical Methods in Fluids*, 74(10):699–731.

Osher, S. and Sethian, J. a. (1988). Fronts propagating with curvature-dependent speed: Algorithms based on Hamilton-Jacobi formulations. *Journal of Computational Physics*, 79(1):12–49.

Papanastasiou, T. C. (1987). Flows of Materials with Yield. *Journal of Rheology*, 31(5):385.

Pastor, M., Blanc, T., Haddad, B., Drempetic, V., Morles, M. S., Dutto, P., Stickle, M. M., Mira, P., and Merodo, J. a. F. (2015). Depth Averaged Models for Fast Landslide Propagation: Mathematical, Rheological and Numerical Aspects. *Archives of Computational Methods in Engineering*, 22(1):67–104.

Pastor, M., Blanc, T., Haddad, B., Petrone, S., Sanchez Morles, M., Drempetic, V., Issler, D., Crosta, G. B., Cascini, L., Sorbino, G., and Cuomo, S. (2014).

Application of a SPH depth-integrated model to landslide run-out analysis. *Landslides*, (August 2013):793–812.

Pastor, M., Blanc, T., and Pastor, M. (2009a). A depth-integrated viscoplastic model for dilatant saturated cohesive-frictional fluidized mixtures: Application to fast catastrophic landslides. *Journal of Non-Newtonian Fluid Mechanics*, 158(1-3):142–153.

Pastor, M., Haddad, B., Sorbino, G., Cuomo, S., and Drempetic, V. (2009b). A depth-integrated , coupled SPH model for flow-like landslides and related phenomena. *International Journal for Numerical Methods in Biomedical Engineering*, 33:143–172.

Pelletier, D., Fortin, A., and Camarero, R. (1989). Are FEM solutions of incompressible flows really incompressible?(or how simple flows can cause headaches!). *International Journal for Numerical in Fluids*, 9(February 1988):99–112.

Perot, J. (1993). An analysis of the fractional step method. *Journal of Computational Physics*, 108:51–58.

Pitman, E. B. and Le, L. (2005). A two-fluid model for avalanche and debris flows. *Philosophical Transactions of the Royal Society A: Mathematical, Physical and Engineering Sciences*, 363(1832):1573–1601.

Pitman, E. B., Nichita, C. C., Patra, A., Bauer, A., Sheridan, M., and Bursik, M. (2003). Computing granular avalanches and landslides. *Physics of Fluids*, 15(12):3638.

Pudasaini, S. P. (2012). A general two-phase debris flow model. *Journal of Geophysical Research*, 117(F3):F03010.

Quarteroni, A., Saleri, F., and Veneziani, A. (2000). Factorization methods for the numerical approximation of Navier–Stokes equations. *Computer Methods in Applied Mechanics and Engineering*, 188(1-3):505–526.

Quecedo, M., Pastor, M., Herreros, M. I., and Fernández Merodo, J. a. (2004). Numerical modelling of the propagation of fast landslides using the finite element method. *International Journal for Numerical Methods in Engineering*, 59(6):755–794.

Radovitzky, R. and Ortiz, M. (1998). Lagrangian Finite Element Analysis of Newtonian Fluid Flow. *International Journal for Numerical Methods in Engineering*, 619(February):607–619.

Richardson, S. (1973). On the no-slip boundary condition. *Journal of Fluid Mechanics*, 59(04):707.

Rossi, R., Larese, A., Dadvand, P., and Oñate, E. (2013). An efficient edge-based level set finite element method for free surface flow problems. *International Journal for Numerical Methods in Fluids*, 71(6):687–716.

Ryzhakov, P. B., Oñate, E., Rossi, R., and Idelsohn, S. R. (2012). Improving mass conservation in simulation of incompressible flows. *International Journal for Numerical Methods in Engineering*, 90:1435–1451.

Salazar, F., Irazábal, J., Larese, A., and Oñate, E. (2015). Numerical modelling of landslide-generated waves with the particle finite element method (PFEM) and a non-Newtonian flow model. *International Journal for Numerical and Analytical Methods in Geomechanics*.

Salazar, F., Oñate, E., and Morán, R. (2012). Modelación numérica de deslizamientos de ladera en embalses mediante el Método de Partículas y Elementos Finitos (PFEM). *Revista Internacional de Métodos Numéricos para Cálculo y Diseño en Ingeniería*, 28(2):112–123.

Savage, S. B. and Hutter, K. (1989). The motion of a finite mass of granular material down a rough incline. *Journal of fluid mechanics*, 199:177–215.

Schaefer, M., Bugnion, L., Kern, M., and Bartelt, P. (2010). Position dependent velocity profiles in granular avalanches. *Granular Matter*, 12(3):327–336.

Schenk, O., Bollhoefer, M., and Roemer, R. A. (2005). On Large Scale Diagonalization Techniques for the Anderson Model of Localization. *ReVision*.

Schenk, O., Wächter, A., and Hagemann, M. (2007). Matching-based preprocessing algorithms to the solution of saddle-point problems in large-scale nonconvex interior-point optimization. *Computational Optimization and Applications*, 36(2-3):321–341.

Schenk, P. M. (1998). Origin of Mountains on Io by Thrust Faulting and Large-Scale Mass Movements. Technical Report 5356.

Schowalter, W. R. (1988). Extrusion instabilities and wall slip. *Journal of Non-Newtonian Fluid Mechanics*, 29:25–36.

Schuster, R. L. and Highland, L. M. (2007). The Third Hans Cloos Lecture. Urban landslides: socioeconomic impacts and overview of mitigative strategies. *Bulletin of Engineering Geology and the Environment*, 66(1):1–27.

Semenza, E. (2001). La storia del Vajont. *Tecomproject, Ferrara (in Italian)*.

Si, H. (2006). A quality tetrahedral mesh generator and three-dimensional delaunay triangulator. *Weierstrass Institute for Applied Analysis and Stochastics (WIAS)*.

Simo, J. C. and Hughes, T. J. R. (2006). *Computational inelasticity*, volume 7. Springer Science & Business Media.

Taboada, A. and Estrada, N. (2009). Rock-and-soil avalanches: Theory and simulation. *Journal of Geophysical Research*, 114(F3):F03004.

Temam, R. (1968). Une methode d'approximation de la solution des equations de Navier-Stokes. *Bull. Soc. Math. France*, 96:115–152.

Tezduyar, T. E., Mittal, S., Ray, S. E., and Shih, R. (1992). Incompressible flow computations with stabilized bilinear and linear equal-order-interpolation

velocity-pressure elements. *Computer Methods in Applied Mechanics and Engineering*, 95(2):221–242.

Thompson, P. A. and Robbins, M. O. (1990). Shear flow near solids: Epitaxial order and flow boundary conditions. *Physical review A*, 41(12):6830.

Thompson, P. a. and Troian, S. M. (1997). A general boundary condition for liquid flow at solid surfaces. *Nature*, 389(September):360–362.

Thouret, J. C., Abdurachman, K. E., Bourdier, J. L., and Bronto, S. (1998). Origin, characteristics, and behaviour of lahars following the 1990 eruption of Kelud volcano, eastern Java (Indonesia). *Bulletin of Volcanology*, 59(7):460–480.

Tormen, D. (2015). Al Veneto il record delle frane: sono 10 mila, primato in Alpago.

van Westen, C. J. and Lulie Getahun, F. (2003). Analyzing the evolution of the Tessina landslide using aerial photographs and digital elevation models. *Geomorphology*, 54(1-2):77–89.

Vardoulakis, I. (2002). Dynamic thermo-poro-mechanical analysis of catastrophic landslides. Geotechnique. *Geotechnique*, 52(3):157–171.

Varnes, D. J. (1978). Slope movement types and processes. *Transportation Research Board*, (176):11–33.

Verfürth, R. (1987). Finite Element Approximation of Incompressible Navier-Stokes Equations with Slip Boundary Condition. *Numerische Mathematik*, 721:697–721.

Vigevano, L. (2003). Lezioni di Fluidodinamica I. *Dipartimento di Ingegneria Aerospaziale*.

Voight, B. and Faust, C. (1982). Frictional heat and strength loss in some rapid landslides. *Géotechnique*, 32(1):43–54.

Wang, F. and Sassa, K. (2010a). Landslide simulation by a geotechnical model combined with a model for apparent friction change. *Physics and Chemistry of the Earth, Parts A/B/C*, 35(3):149–161.

Wang, F. and Sassa, K. (2010b). Landslide simulation by a geotechnical model combined with a model for apparent friction change. *Physics and Chemistry of the Earth, Parts A/B/C*, 35(3-5):149–161.

Ward, S. N. and Day, S. (2011). The 1963 landslide and flood at vaiont reservoir Italy. A tsunami ball simulation. *Italian Journal of Geosciences*, 130(1):16–26.

Xiao, Z. and Komatsu, G. (2014). Reprint of: Impact craters with ejecta flows and central pits on Mercury. *Planetary and Space Science*, 95:103–119.

Xiao, Z., Zeng, Z., Ding, N., and Molaro, J. (2013). Mass wasting features on the Moon - how active is the lunar surface? *Earth and Planetary Science Letters*, 376:1–11.

Yoon, D. K., Jenkins, J. T., and JTJenkins (2005). Kinetic theory for identical, frictional, nearly elastic disks. *Physics of Fluids*, 17(8):1–10.

Zhang, X., Krabbenhoft, K., Sheng, D., and Li, W. (2015). Numerical simulation of a flow-like landslide using the particle finite element method. *Computational Mechanics*, 55(1):167–177.

Zienkiewicz, O. C. and Codina, R. (1995). A general algorithm for compressible and incopressible flow-Part I. The split, characteristic-based scheme. *Int. J. Numer. Meth. Fluids*, 20(8-9):869–885.

Zienkiewicz, O. C., Codina, R., and Vàzquez, M. (1998). A general algorithm for compressible and incompressible flow-Part III. The semi-implicit form. *Int. J. Numer. Meth. Fluids*, 27(1):13–32.